This is to certify that the

dissertation entitled

EFFECT OF FORCING ON THE VORTICITY
FIELD IN A CONFINED WAKE

presented by

RICHARD K. COHN

has been accepted towards fulfillment
of the requirements for

PhD degree in Mechanical Engineering

M. M. Koochesfahani
Major professor

Date March 15, 1999

EFFECT OF FORCING ON THE VORTICITY FIELD IN A CONFINED WAKE

By

Richard K. Cohn

A DISSERTATION

Submitted to
Michigan State University
in partial fulfillment of the requirements
for the degree of

DOCTOR OF PHILOSOPHY

Department of Mechanical Engineering

1999

ABSTRACT

EFFECT OF FORCING ON THE VORTICITY FIELD IN A CONFINED WAKE

By

Richard K. Cohn

Several recent studies have found that when a low Reynolds number, plane wake is forced with sufficient amplitude, the normalized mixing product, measured as the amount of mixed fluid per unit width of the wake, can be increased to levels larger than those seen in high Reynolds number mixing layers. However, no studies examining the velocity and vorticity fields of this flow have been conducted. The present study examines the velocity and vorticity field of a low Reynolds number plane wake within a confining channel in order to better understand the vortex-vortex and vortex-wall interactions in order to shed light on the mechanisms which lead to increases in the amount of mixed fluid within the wake.

Molecular Tagging Velocimetry (MTV) is used to measure the velocity field in both the streamwise (u, v velocities in x, y plane) and cross-stream (v, w velocities in y, z plane) measurement planes. The spanwise and streamwise vorticity components are then computed from their respective velocity fields. The experimental results represent the first time MTV has been used to make whole-field velocity measurements in a plane where the mean flow is moving directly out of the measurement plane. Increases were also made in the number of measurement points per image plane which has been increased by more than the 50% over previous MTV studies. Advances were also made in several post-processing aspects of MTV including the determination of the best method to remap the velocity data onto a regular grid

and methods to compute vorticity from this data.

Measurements in the streamwise plane have found that a distinct spatial periodicity exists in the u_{rms} field that is not found in either the unforced case or in unconfined forced flows such as the wake of an oscillating airfoil. A model was developed which relates this spatial periodicity to the phase difference between the forcing input and the rolling up of the vorticity shed from the splitter plate. From these data, it was also determined that the phase at which vorticity is shed is dependent upon the forcing amplitude.

The forced wake flow is dominated by the shedding of concentrated, spanwise vortex core rollers. As these cores develop downstream, the levels of peak vorticity within the core decrease. This decrease has been shown to be dominated by negative vortex stretching, rather than diffusion. A very small amount of $-\partial w/\partial z$ is sufficient to generate a very large decrease in peak vorticity levels. This same quantity has also been found to be a good predictor of the spatial location where mixing enhancement will occur in the forced wake.

Mixing enhancement is accomplished by the generation of regions of streamwise vorticity from the reorientation of the primary spanwise vortex cores. In flows where mixing enhancement occurs, multiple regions of streamwise vorticity quickly convect towards the center of the test section. A model was developed which describes how these cores develop. The multiple regions of streamwise vorticity are the result of the passage and reorientation of multiple spanwise rollers. As each roller is reoriented into the streamwise direction, it experiences a large amount of stretching which increases the peak vorticity levels. These reoriented “legs” of streamwise vorticity interact with the regions of streamwise vorticity resulting from the passage of previous spanwise vortex rollers to generate the additional surface area necessary for mixing enhancement.

ACKNOWLEDGMENTS

It would not have been possible to complete this work without the help of many people. I would like to thank all of my lab-mates over these past years, for the many hours of conversation and assistance needed to complete this projects. I would like to specifically thank, Chuck Gendrich, Colin MacKinnon, Doug Bohl, Hooman Rezaei, Greg Katch, and Suman Chakrabarti for their assistance in completing this work. I would also like to thank my advisor, Dr. M.M. Koochesfahani, for his years of assistance. This work would also not have been possible without the financial support of the AFOSR, the Center for Sensor Materials at Michigan State University, a National Science Foundation Graduate Research Fellowship, and the Air Force Research Laboratory Palace Knight program.

Finally, I would like to thank my wife Misty, who stuck through all of these years of late nights and odd hours necessary for the completion of my degree. Your support was essential to the completion of my program.

TABLE OF CONTENTS

Table 2.1. F
the p
strea
low.
Kov

Table 2.2:
mea

Table 2.3:
mea

LIST OF TABLES

LIST OF FIGURES

LIST OF SYMBOLS AND ABBREVIATIONS

Abbreviations and Notations

AD	Analog to Digital Converter
MTV	Molecular Tagging Velocimetry
RMS	Root Mean Square
< x >	Phase average of quantity x
$\overline{x}$	Mean of quantity x
x_{bias}	Bias error in measurement of quantity x
x_{max}	Maximum value of quantity x
x_{peak}	Value of x at peak vorticity
x_{rms}	Root mean square of quantity x

Symbols

A	Forcing amplitude measured as u_{rms}/u_0 in percent
F	Forcing frequency in cycles per second
f	Generic value for frequency in cycles per second
h	Spacing between points on the regular grid
L	Characteristic flow length scale – equal to the vortex core radius
M	Molarity
n	Maximum percentage of noise added
n_{random}	Actual percentage of noise added to a velocity component
R	Maximum radius used in the least squares fit

r	Radial location
r_{core}	Vortex core radius
r_{min}	Minimum distance from regular grid location to velocity measurement location
T^*	Total record length
t	Time
$U_{A,0}$	Velocity magnitude at point A at phase 0
U_{fs}	Instantaneous velocity magnitude in free stream region
u	Streamwise velocity
$u_{i,j}$	Velocity in x component direction at node i, j
u_0	time-averaged free stream velocity
u_θ	Azimuthal velocity about center of concentrated vortex core
v	Transverse velocity
$v_{i,j}$	Velocity in y component direction at node i, j
w	Spanwise velocity
x	Streamwise coordinate direction
y	Transverse (y) coordinate direction
z	Spanwise coordinate direction
z_{cam}	Distance from measurement plane to camera
Δt	Time delay between undelayed and delayed images
δ	Mean spacing between velocity measurements
δ_p	Wake product thickness
δ_1	Wake visual 1% thickness

η	An integer number
ϕ	Phase of measurement data – $0 < \phi < 1$
ϕmax	Required spatial distribution of velocity measurements used in least squares fit
ϕmin	Required spatial distribution of velocity measurements within rmin region
Γ	Circulation
λ	Wavelength between vortex cores
λ_{laser}	Wavelength of laser light used in experiments
τ	Phosphorescence lifetime
θ	Wake momentum thickness
ω_{max}	Maximum vorticity
ω_x	Streamwise vorticity
ω_z	Spanwise vorticity
ζ	Peak level of forcing amplitude

Chapter 1

Introduction

1.1 Motivation

Several recent studies have examined the mixing properties of forced, low Reynolds number, confined plane wakes. These studies have shown that when forced with sufficient amplitude, both the total amount of molecularly mixed fluid in the wake region as well as normalized mixing product, the amount of mixed fluid per unit width of the wake, can be increased to values larger than those seen in unforced, high Reynolds number mixing layers. Figure 1.1 shows of two views this flow. Two streams of fluid which are initially separated by a thin splitter plate are allowed to interact once the plate ends. Unlike in a shear layer, the speeds of the two streams are equal which presents several important differences in the structure of the flow. The flow to be examined also has characteristics of both an external

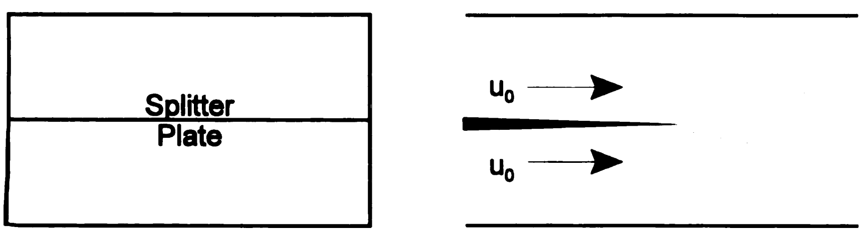

Figure 1.1: Schematic of the wake flow. Note that the wake is confined both on the top and bottom walls as well as by the sidewalls of the facility.

and an inte

region can

is the wak

walls, play

characteris

confined".

A re

mixed fluid

even in high

turbulent sha

have been co

velocities ome

properties of

this flow a

that is use

Figur

the wake f

streamwise fl

these length

the forcing

ed by me

the influence

become app

and an internal flow. In the initial stages of the development of the flow field, the center region can be considered to be a free region and it behaves as if it is not confined. However, as the wake continues to develop, the confining walls of the facility, particularly the side walls, play an important role in the flow structure and development Since this flow has characteristics of both confined and unconfined flows, it will be referred to as "semi-confined".

A recent study by Koochesfahani and Nelson (1997) has shown that the normalized mixed fluid fraction in this low Reynolds number forced wake is three times larger than that seen in high Reynolds number liquid mixing layers and 60% larger than that in gas-phase turbulent shear layers. However, no studies of this velocity and vorticity fields of this flow have been conducted. The research presented in this work examines the three-dimensional vortex-vortex and vortex-wall interactions of a confined plane wake as well as many other properties of this flow field in order to examine the behavior of the underlying vorticity field in this flow and to try to connect the mixing increase to its behavior. In this study, the term vortex is used to denote a concentrated region of vorticity with the same rotational sense.

Figure 1.2 shows sample streamwise flow visualizations of an unforced and forced plane wake from MacKinnon and Koochesfahani (1997). The measurement range for the streamwise flow visualization results are $1\ cm < x < 12\ cm$, which corresponds to the first *8* wavelengths of the vorticity field. This study was conducted in the same facility with the same forcing conditions as will be examined in this research. The forcing in this flow is applied by means of oscillating the speed of one of the free streams. In the streamwise view of the unforced wake, the flow is starting to become unstable and undulations are beginning to become apparent in the interface separating the two streams as they move downstream.

Unforced Forced

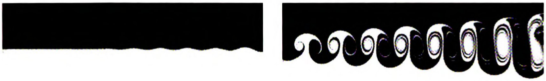

(a) Streamwise View

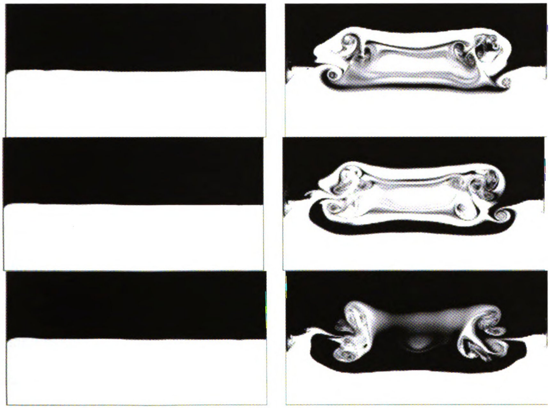

(b) Spanwise View

Figure 1.2: Laser induced fluorescence visualization of the unforced (left) and forced (right) wake from MacKinnon and Koochesfahani (1997). (a) Streamwise view for *1 cm* $< x <$ *12 cm* downstream of the splitter plate tip. The flow direction is from left to right. (b) Spanwise views of the test section cross-section at x = *8 cm* at three representative times in the forcing cycle.

However

refer to

W

Previou

Seve

However, there is little evidence of vortical structures. In contrast, the forced case is dominated by a concentrated Karman vortex street of spanwise vortices. Several studies also refer to these regions of spanwise vorticity as the spanwise "rollers". Although not shown here, further flow visualization results presented in MacKinnon and Koochesfahani (1997) show that the strength and spacing of these vortices vary depending upon the amplitude of the imposed forcing in the flow. When examined in the cross-stream (y-z) plane, it is apparent from these visualizations that the flow near the sidewalls of the test section is not two-dimensional and the existence of streamwise vorticity is apparent. As in the streamwise view, very little motion is seen in the unforced case. Further flow visualization images of the forced case, also not shown here, suggest that the region of three-dimensional motion moves closer to the center of the test section as the downstream distance increases.

Wake flows such as the one being studied are qualitatively different from the often studied shear layer flows. Most notably, the forced wake contains vorticity of both signs whereas shear layers contain only one sign of time-averaged vorticity. Breidenthal (1980) examined a wake and a shear layer forced by various configurations of wedges placed on the trailing edge of the splitter plate. With this method of forcing, it was shown that shear layers rapidly relax to the characteristic two-dimensional large vortex structures, whereas the forced wake remains three-dimensional. Furthermore, the forced wakes exhibited large spanwise variations in mixing products far downstream which was not seen in the forced shear layers.

1.2 Previous work

Several research groups have measured the mixing field characteristics of a confined, forced wake. These studies have shown that forcing can result in a significant increase in the

amount of mixed fluid. Breidenthal (1980), whose results are mentioned above, used the reaction of phenolphtalein and a base to measure the visible mixing product in a wake forced with a three-dimensional perturbation. Roberts (1985) applied two-dimensional forcing, similar to that applied in the present study, to a wake flow by varying the pressure drop in one of the streams. This study made use of both an absorption based technique similar to Breidenthal as well as passive scalar measurements to examine the effect of varying the forcing frequency on the amount of molecular mixing. This study observed a significant increase in mixing when the flow was forced at twice the natural shedding frequency. Examination of the cross-stream *(y-z)* plane at different x locations showed that in the upstream region, regions of concentrated streamwise vorticity exist near the sidewalls. At locations father downstream, these regions of ω_x move rapidly inwards towards the center of the facility.

Robert's study also proposed the following model to partially explain the increase in mixing. Close to the sidewalls of the facility, the boundary layer will cause the predominately spanwise vortex tubes to be reoriented into the streamwise direction. If the streamwise vortices, which were generated by reorientation, are modeled as two point vortices close to a wall, the induction of the vortices and their images in the side walls of the facility will cause these original vortices to propagate away from the sidewall towards the center of the test section. It was noted that forcing was found to cause the vertical separation between the vortices in the wake to change and when the wake was forced at twice the natural frequency, vertical distance between the positive and negative signs of vorticity reached a minimum. In the proposed model, as the vertical distance between the counter-rotating vortices decreases, the propagation speed of the pair away from the wall will increase. This increased motion of the streamwise vortices in the cross-stream plane created the additional surface area necessary for the two reactants to combine.

MacKinnon and Koochesfahani (1997) studied the effect of varying the forcing amplitude on the mixing field of this flow. The forcing frequency was fixed near the natural shedding frequency of the wake. Using a passive scalar technique, this study found that high amplitude forcing caused a significant increase in the amount of mixing product generated over the unforced case. Flow visualization results showing the evolution of the cross-stream plane of this flow suggest the existence of additional streamwise vortices and more complex interactions than can be described by Robert's model of the reorientation of the spanwise vorticity and its propagation towards the center of the test section.

Nelson (1996) and Koochesfahani and Nelson (1997) used a chemical reaction technique to directly measure the amount of chemical product under the same conditions as MacKinnon and Koochesfahani (1997). Data from Koochesfahani and Nelson (1997) presented in Figure 1.3a, show the extent of the increase in the chemical product as the forcing amplitude is increased. When compared to the unforced layer, forcing at low (2%) and moderate (5%) amplitudes results in a small increase in the amount of mixed fluid. The high (9%) amplitude forcing case, however, results in a much more significant increase in the amount of mixed fluid. The measured product thickness of the highly forced wake is 40 times larger than that in the unforced layer. The leveling out of this profile at approximately 20 cm is likely due to the vortical structures impinging upon top and bottom walls of the test section. If the test section had a greater height, the amount of mixed fluid would likely continue to increase. Figure 1.3b shows the amount of mixed fluid normalized by the local wake width. This normalized mixing product represents the percentage of the wake width

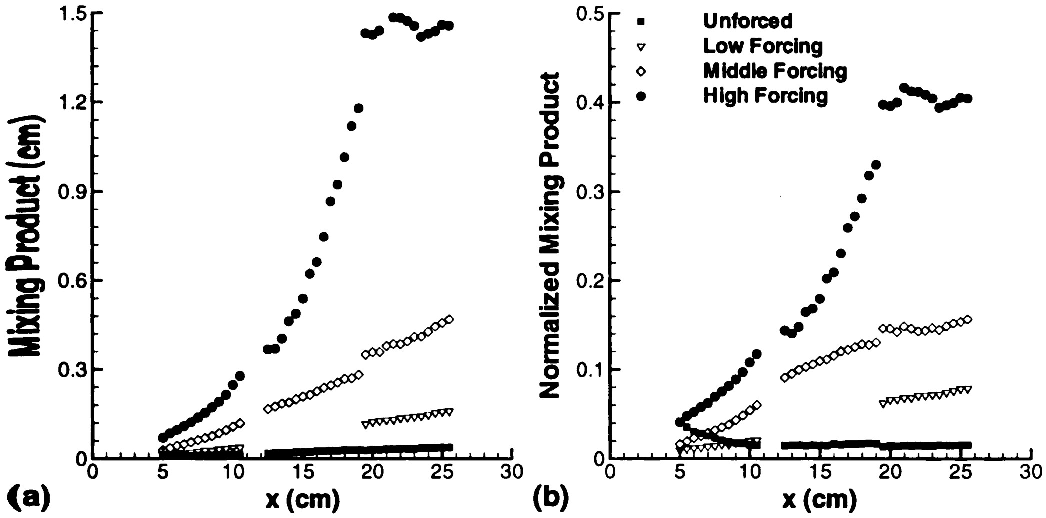

Figure 1.3: Streamwise variation of total mixing product (a) and normalized product thickness (b) at the mid-span location for different forcing amplitudes. Data is from the mixing studies of Koochesfahani and Nelson (1997).

occupied by mixed fluid. Although the amount of the increase is less than that seen in the total product, the normalized mixing product shows a significant increase in the high amplitude forcing case over the other forcing cases. Thus, the increase is not solely in the width of the mixing layer. Rather, the amount of mixed fluid within the mixing layer has increased as well.

The studies of this flow field have so far been limited to flow visualization and scalar concentration levels. No studies of the fluid dynamical properties that generate this enhanced mixing field are known. However, based on the flow visualization information, the streamwise vorticity field is believed to play a major role in the mixing enhancement. The current study, using the same facility as the works of Koochesfahani, Nelson, and MacKinnon will quantitatively examine the fluid dynamical properties of this flow field in order to better understand its mixing properties.

Although there have been no quantitative studies of a forced, semi-confined two-stream wake such as those in which the mixing studies have been conducted, several detailed quantitative studies of the free plane wake of a flat plate have been conducted. Sato and Kuriki (1961) made hot-wire velocity measurements in the wake behind a thin flat plate in order to examine the laminar-turbulent transition. Both the natural wake and wakes perturbed with low-level acoustical forcing were studied. Three distinct regions were found in the wake. A "linear" region in which sinusoidal velocity fluctuations were exponentially amplified, a "non-linear" region where harmonics of the input fluctuations were amplified, and finally, a "three-dimensional" region where the velocity fluctuations were believed to be perpendicular to the measurement plane. Sato (1970) expanded this study to include forcing with multiple frequencies.

Mattingly and Criminale (1972) examined the near wake region both experimentally and using a theoretical analysis based on inviscid stability theory. This study suggested that the development of forced wakes, even those forced with very small amounts of excitation, could be different from the development of natural wakes. Forcing near the natural frequency eliminates the approximately 10% drift observed in the natural frequency of the shedding which is perhaps an inherent part of the flow. Further, forcing generates an oscillation in the free-stream region which will interact in an undetermined way with the shed vorticity. Wygnanski *et al.* (1986) studied a variety of different wake flows, including cylinders, flat plates, airfoils, and screens, in order to determine the universality of their self-preserving states. Although the wake of each vortex generator was self-preserving, the characteristic velocity and length scales, when suitably scaled by the momentum thickness and free-stream velocity, as well as the turbulence intensity distribution, when suitably normalized, were found to depend upon the geometry of the wake generator, which indicates a sensitivi

universal.

M

of a flat p

another t

streamwis

studies sug

activity.

the spanw

causes the

developme

that by di

W

curved wal

from inpu

between th

the distu

and conc

initial str

LeB

flow an

adequate co

and was se

a sensitivity to the initial conditions of the wake. The mean velocity profiles, however, were universal.

Meiburg and Lasheras (1988) and Lasheras and Meiburg (1990) examined the wake of a flat plate with periodic spanwise and streamwise perturbations. Depending upon whether the initial perturbations were in the spanwise or streamwise direction, the streamwise vorticity developed either a "symmetric" or a "non-symmetric" pattern. These studies suggested a mechanism for the self-amplifying increase in the amount of streamwise vorticity. Once the primary spanwise vorticity develops a kink, the induced velocity due to the spanwise vorticity causes the kink to lift up. Then, the induced velocity of this portion causes the development of additional kinks and additional streamwise vorticity. Thus, the development of the wake is dominated by the reorientation and stretching of vorticity rather than by diffusion.

Weygandt and Mehta (1995) studied the three-dimensional evolution of plane and curved wakes. In comparison with shear layers, it was found that the wake is slow to recover from input perturbations. Shear layers are constantly energized by the velocity difference between the two layers. The resulting turbulent mixing can, in some cases, "wash-out" the input disturbance. The streamwise vorticity was also found to be extremely sensitive to the initial conditions. When the initial boundary layer was tripped, no stationary streamwise vortical structures were observed.

LeBoeuf and Mehta (1996) conducted detailed measurements of a wake forced with very low amplitude acoustic waves. The purpose of the forcing in this study was to ensure adequate coherence to allow the velocity measurements to be phase averaged, so the forcing level was set to the smallest value allowed by their amplifier. Velocity measurements were made with a cross-wire hot-wire anemometer probe that was traversed through the measurement volume. The probe was rotated in order to measure all three components of velocity. As the flow is phase-averaged, the entire velocity field at a given phase can be recovered and the vorticity components calculated. It was found that the phase-averaged streamwise vorticity levels were 40% of the spanwise vorticity levels. The peak streamwise vorticity values were also found to coincide with the location of the tubes of spanwise vorticity. The streamwise circulation was found to be 20% of the levels found in the spanwise vortical tubes. It is interesting to note that the average circulation of the streamwise vortices remained constant as they travel downstream. This study, along with the studies by Lasheras and Meiburg, concentrated on the central regions of test sections where the effect of walls and other boundary conditions are minimal. In these cases, it is believed that the streamwise vorticity is generated by a local distortion in the spanwise vorticity field which is then reoriented into the streamwise direction by the induced flow generated by the vorticity in the legs of the distortion as suggested by Lasheras and Meiburg. The origin of the initial kinks in the roller span is believed to be a small disturbance in the flow field.

1.3 Potential mechanisms for increased mixing

Several possible mechanisms for the increase in mixing will be explored in this work. Robert's model that the initial spanwise vorticity is reoriented in the streamwise direction will result in the development of more surface area for constituent chemicals to mix. However, MacKinnon and Koochesfahani (1997), have shown that streamwise vorticity field is more complicated and cannot be described solely by the reorientation of a single spanwise vortex roller. The recent study of the transition of a plane wall jet by Visbal *et al.* (1998)

may have particular relevance to the current in work. This study has shown that in a forced wall jet, vortex tubes can split into discrete concentrations of vorticity. The splitting process was found to begin near the wall and to propagate towards the center of symmetry. The spiral branches formed are wrapped around the original vortex core twisting in the opposite direction of the vortex swirl.

As suggested by Lasheras and Mehta, once a spanwise distortion of the spanwise vortex roller develops, it will generate more distortions resulting in more streamwise vorticity. Near a wall, as in the present study, a distortion develops as the boundary layer causes the spanwise vorticity to be reoriented. Additionally, vortex stretching will have a significant impact on the streamwise vorticity for the portion of the vorticity near the sidewall of the facility slows due to the boundary layer. The resulting stretching will result in the increase in the magnitude of the streamwise vorticity.

A second possible mechanism for the increased mixing can be the existence of an axial flow within the spanwise vortex cores. In studies of concentrated vortex cores in the wake of oscillating airfoils, it has been shown that an axial flow is generated along the vortex core whenever a vortex encounters a solid boundary (Cohn and Koochesfahani, 1992, Koochesfahani, 1989). Axial flow along the vortex core can develop if the core passes over a region where the no-slip condition is applied over a length of the order of the vortex core diameter. Cohn and Koochesfahani (1992) have further shown that the no-slip condition is not necessary for the generation of axial flow. This type of cross-stream fluid transport has also been found within vortices in a forced shear layer and in the wake of a cylinder (Kurosaka *et al.*, 1988) and within hairpin vortices in boundary layers (Hagen and Kurosaka, 1993). In the forced wake flow currently being studied, the concentrated spanwise vortices pass ove

ures.

A

cross-stre

making

could be

mechanis

the stream

continua

In

are mapp

location

captured

process

pass over a solid wall, so it seems likely that an axial flow might exist within the vortex cores.

Although it is not known whether core-wise axial flow exists in this flow, strong cross-stream transport could act as a pump, bringing unmixed fluid into areas where mixing is taking place, and moving mixed fluid into regions normally occupied by pure fluid. It should be noted that this mechanism may be acting in concert with the previously mentioned mechanisms. The study by Visbal *et al.* (1998) found that in terms of the induced velocity, the streamwise vorticity arrangement generated by the splitting process found the plane jet is consistent with axial flow towards the plane of symmetry.

In the research presented, the velocity and vorticity fields in a forced confined wake are mapped in order to gain a better understanding of the vortex-vortex and vortex-wall interactions that generate the three-dimensional motions. These interactions are then examined in order to shed light on the mechanisms which could result in the significant increases in the amount of mixed fluid found in the forced wake.

Chapter 2

Experimental Procedure

2.1 Mixing layer facility

The experiments were conducted in the gravity driven, liquid mixing layer facility located in the Turbulent Mixing and Unsteady Aerodynamics Laboratory at Michigan State University. This is the same facility used in the mixing studies conducted by MacKinnon and Koochesfahani (1991 and 1997), Nelson (1996), and Koochesfahani and Nelson (1997). In this facility, shown schematically in Figure 2.1, fluid (water mixed with the chemicals necessary for the molecular tagging diagnostic technique utilized in these experiments) from two reservoir tanks is pumped into two constant head reservoirs approximately *3.5* meters above the test section. From the constant head section, the two separate streams of fluid pass through their own set of control valves and flow meters.

The flow meters and valves allow the mass flow rate through each side of the facility to be controlled to within ±1.5% during the course of the experiments. That is, the mass flow rate of each of the streams of fluid may vary by a maximum of ±1.5% during the course of all of the experimental runs presented. During a typical experimental set, the mass flow rate varied by less than ±0.75%. For the experiments conducted for this work, the mass flow rate was set such that the free stream velocities in the two sides were $U_1 = U_2 = 9.4\ cm/s$. This allows the measurements made in this study to be directly compared with the mixing results previously mentioned.

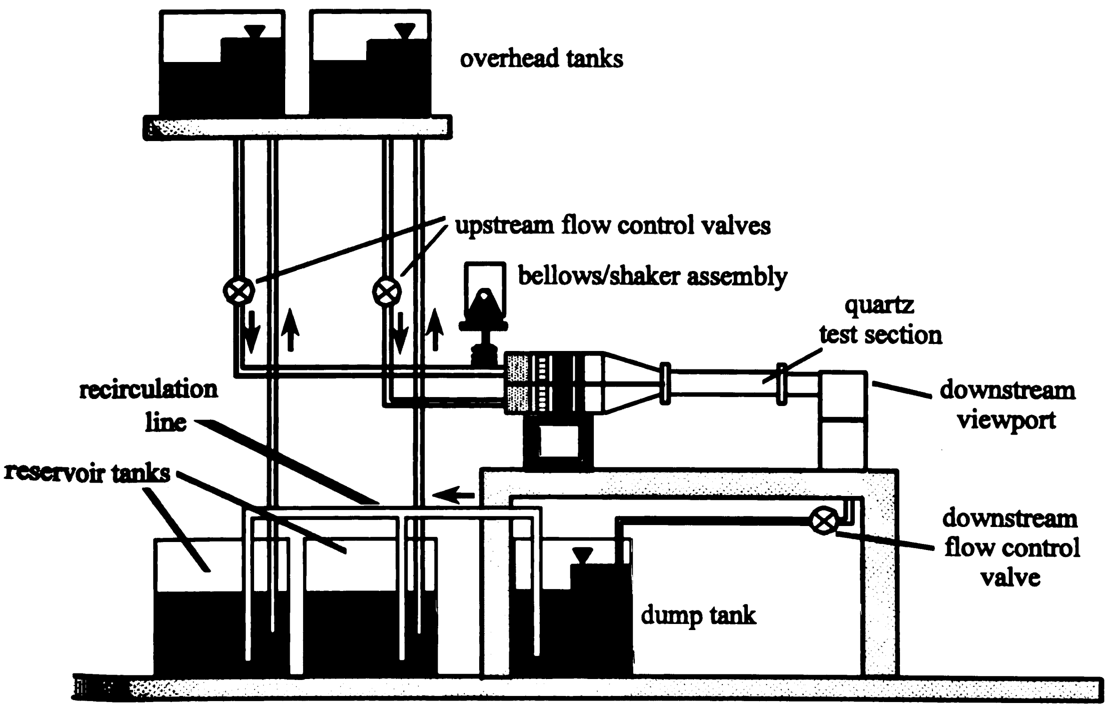

Figure 2.1: Schematic of the mixing layer facility.

manage

order to

separate

the two

of the sp

T

the cross

section a

flow to e

nt cont

T

section th

Tally is

ulized

Reyglas

these expe

order fo

section

and th

used up

Th

the studie

After passing through the valves and flow meters, the fluid travels through a flow management unit consisting of foam, honeycomb, and several layers of perforated plates in order to eliminate large scale motions. Within the flow management unit, a flat splitter plate separates the two streams. This splitter plate ends *1.5 cm* upstream of the test section and the two streams are allowed to interact. The origin of the streamwise coordinate, x, is the end of the splitter plate.

The return section of this facility is unique in that it contains a viewport that allows the cross-stream flow to be examined. This is accomplished by the presence of a straight section and turning vanes in the downstream return section of the facility which direct the flow to either side of the test section before it travels into the dump tank. The downstream unit contains a Plexiglas window which allows direct viewing of the flow in this plane.

The test section of this facility is *30 cm* in the streamwise dimension and has a cross-section that has a span of *8 cm* and transverse dimension of *4 cm.* The test section of this facility is normally constructed of Plexiglas. However, the molecular tagging diagnostics utilized in these studies require that ultraviolet light be passed into the test section and Plexiglas absorbs these wavelengths. A new test section made of quartz was designed for these experiments. It was necessary to glue Aluminum bracing on the edge of the test section in order for the section to be able to withstand the pressure of the water. A schematic of the test section is shown in Figure 2.2. This test section is connected to the flow management unit and the return sections by means of plexiglass flanges. Due to these modifications, the farthest upstream location where measurements can be made is approximately $x = 3\ cm$.

This flow facility is designed to run as a blow-down facility when scalar mixing is being studied with the fluid being dumped after passing through the test section. However,

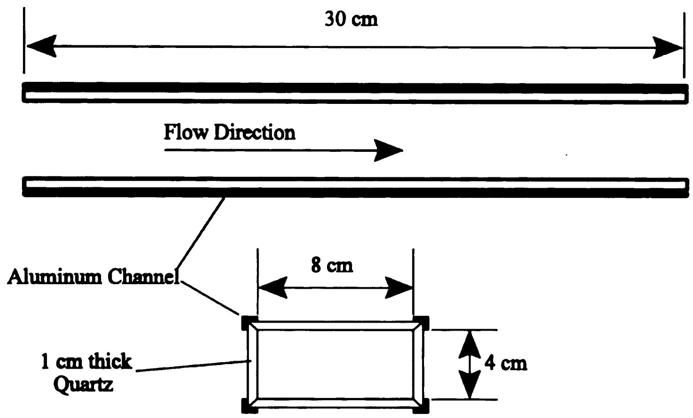

Figure 2.2: Schematic of test section.

for this purely velocimetry study, the facility is operated in a closed loop mode with the fluid being recirculated from the dump tank back into the reservoir tanks. This allows the facility to be continuously operated during the course of the experiments.

Previous visualization studies conducted in this facility determined that the natural frequency of the shed vortices is approximately *6 Hz* when the free-stream velocities are set to *9.4 cm/s*. In the present study, this was measured to be *6.5 Hz*. However, measurements will still be made at $F = 6\ Hz$ in order to compare with the previous mixing studies. Velocity measurements made at the splitter plate tip have also found the momentum thickness across the unforced wake, $\theta = 0.1\ cm$. This value is consistent with the values of θ measured at a variety of downstream locations in the current study. Thus, Re_θ for this flow is about *100*.

2.2 Forcing mechanism and conditions

Two-dimensional perturbations are introduced into the upper free-stream of this flow by means of an oscillating bellows mechanism in the upper supply line. The diameter of the

Table 2.1: Forcing conditions for forced wake experiments. The forcing amplitudes indicate the percentage of the free stream velocity of the root mean square fluctuations of the streamwise velocity. Superscripts 1, 2, and 3 are the cases which correspond to the low, middle, and high amplitude forcing cases (respectively) of Nelson (1996), Koochesfahani and Nelson (1997) and MacKinnon and Koochesfahani (1997).

Frequency	**4 Hz**	**6 Hz**	**8 Hz**
	2.7	2.1^1	2.4
		2.8	
Forcing		4.3	
Amplitudes		5.3	
(% RMS)	7.7	7.3^2	9.8
		8.5	
	11.4	10.2	13.8
		11.6^3	
		13.3	

bellows is 5 cm. This mechanism is driven by an electromagnetic shaker whose command signal originates from a Hewlett-Packard 3314a function generator. With this setup, it is possible to input an arbitrary forcing perturbation into the flow. However, only the effect of purely sinusoidal perturbations will be examined in this study. A velocity and a position transducer are attached to the bellows mechanism to track the actual motion of the bellows. These signals, along with the command signal, are digitized by a 12 bit Analog to Digital (AD) Converter simultaneous with the velocity measurements in order to facilitate phase averaging of the measured data.

Table 2.1 shows a list of the forcing conditions used in the study. The majority of the studies are conducted at the 6 Hz sinusoidal forcing perturbations, which is very close to the natural Karman shedding frequency of this flow. A larger frequency (8 Hz) and a smaller frequency (4 Hz) are also examined, although not in as great detail as the 6 Hz case.

In order to ascertain the effect of increasing the forcing amplitude, a range of perturbation levels will be examined. The forcing amplitude is defined by dividing the measured free stream RMS fluctuations measured in the flow by the mean free stream velocity. For the 6 Hz case, nine different perturbation amplitudes are studied ranging from the unforced case, up to the maximum fluctuation level being in excess of 10% of the free stream speed. It should be noted that due to the size of the test section, no "free stream" region exists in the 4 Hz case. Therefore, the RMS magnitudes listed for that case are only used in order to provide a label for these cases. This will be described in more detail in Chapter 5.

In order to directly compare the results of the present velocimetry study with the mixing results, conducted in the same facility, of Nelson (1996), Koochesfahani and Nelson (1997) and MacKinnon and Koochesfahani (1997), several of the forcing conditions were selected to match those used in these previous mixing studies. This was accomplished by matching both the input perturbation waveform, as well as the peak-peak amplitude and the RMS of the measured bellows position. The cases in the present study which match those in the mixing studies are denoted by superscripts 1, 2, and 3 in Table 2.1. These will be referred to as the low, middle, and high amplitude forcing cases.

A numerical difference is seen between the quoted values of the perturbation levels in the mixing and velocimetry studies. A portion of this difference is due to the random error inherent to the measurement technique which will tend to increase the measured fluctuation levels in the present study. Visualization results indicated that the structure of the low, middle and high amplitude mixing results is very similar to the 2.1%, 7.3%, and 11.6% forcing levels in the present study.

2.3 Velocity measurement method (Molecular Tagging Velocimetry)

Measurements are made using Molecular Tagging Velocimetry (MTV). MTV is a full-field optical diagnostic which allows for the non-intrusive measurement of the velocity field in a flowing medium. This technique has previously been used by several authors such as Gendrich *et al.* (1994), Stier (1994), Cohn *et al.* (1995), Hill and Klewicki (1996), Koochesfahani *et al.* (1996), Cohn and Koochesfahani (1997), and Gendrich, Bohl, and Koochesfahani (1997), Gendrich, Koochesfahani, and Nocera (1997) to make measurements in a wide variety of flows.

The molecular tagging technique takes advantage of molecules having a long-lived excited states which can be viewed after tagging by a photon source. The displacement of the luminescence of these molecules is tracked over the luminescence lifetime in order to determine an estimate of the velocity field. The tracer used in the present study is a recently engineered molecular assembly containing 1-Bromonapthalene, Gβ-Cyclodextrin and Cyclohexanol dissolved in water. This combination has a phosphorescent lifetime, $\tau \cong 5$ ms when excited by an ultraviolet laser light source. It should be noted that lifetime is measured as the time when the intensity drops to e^{-1} of the original intensity. Measurements can be made using time delays much longer than τ with the use of proper detectors. Details about the use of this molecular assembly in MTV can be found in Gendrich, Koochesfahani, and Nocera, 1997. Additional details about the chemical properties of this molecular assembly can be found in Ponce *et al.*, 1993 and Hartmann *et al.*, 1996.

The concentration of the Gβ-Cyclodextrin in the flowing solution is driven by two competing factors. The larger the concentration, the higher the intensity of the phosphorescence. However, the penetration of the laser beam decreases because of increased absorption by the phosphorescent complex. Since the working distance in the mixing layer facility is relatively small, concentrations of Gβ-Cyclodextrin between $2 \times 10^{-4}\,M$ and $3 \times 10^{-4}\,M$ were used. The concentration of the alcohol was kept at *0.06 M*. The study of Gendrich, Koochesfahani, and Nocera (1997) shows that there is no increase in intensity for alcohol concentrations larger that *0.055 M*. The additional alcohol used in the present study was to make certain the intensity was as large as possible. Only a limited amount of Bromonaphthalene will dissolve in a water solution. Enough Bromonaphthalene was placed in the solution so that it was saturated and a small amount of undissolved Bromonaphthalene could be seen. The presence of these compounds in solution has the effect of decreasing the kinematic viscosity of water by approximately *5%*.

This technique can be thought of as the molecular equivalent of Particle Image Velocimetry (PIV). Rather than tracking particles placed in the flowing medium, the luminescence lifetime of the tracer molecules is tracked. An abbreviated description of the molecular tagging technique will be given here. A more complete description the implementation of the molecular tagging technique and the parameters necessary for an optimal experiment can be found in Gendrich and Koochesfahani (1996) and Gendrich (1998).

Two velocity components can be measured in a flow when there is a spatial gradient in the luminescence intensity field of the tagged region in two (preferably) orthogonal directions. An intensity field of this type can be generated by crossing a pair of laser beams in the flowing medium containing luminescent markers. The displacement of the tagged region can then be measured by means of a spatial cross-correlation between two images

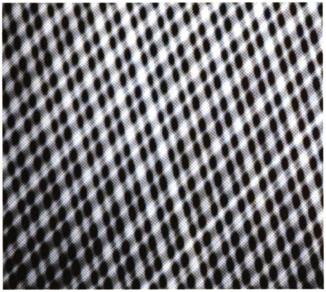

Figure 2.3: Sample MTV measurement grid.

acquired at different times within the luminescence lifetime of the marker. In order to gain sub-pixel accuracy, the cross-correlation field is then fit to a high order polynomial. Gendrich and Koochesfahani (1996) shows the accuracy of the MTV technique is dependent upon a number of conditions including the signal to noise ratio in the images, contrast, the laser line widths and line profile. Based on the quality of the images and conditions in the current experiments, it is believed that the 95% confidence interval of the results presented here is less than *0.1* pixel. This means that 95% of the measurements are more accurate than *0.1* pixel. Thus, a displacement of *10* pixels will yield a dynamic range of *100*. In the current measurements, *0.1* pixels corresponds to *0.15 cm/s* and *0.2 cm/s* for the for the streamwise and cross-stream measurement planes respectively.

In order to measure the velocity field throughout a region, many laser beam crossings must be generated. This can be accomplished by generating a grid of intersecting laser lines shown in Figure 2.3. Each intersection is a "location" where a velocity measurements is made. In the experiments reported here, these grids are created by passing a laser sheet

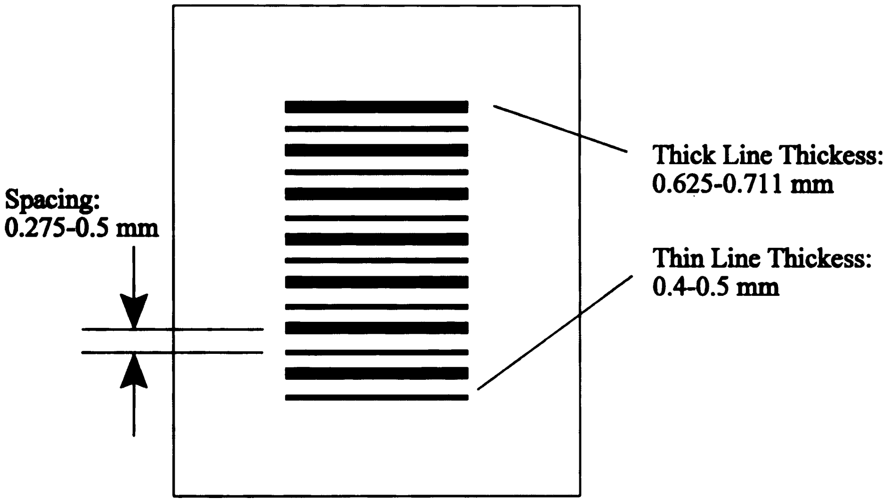

Figure 2.4: Sample beam block used in MTV experiments.

through a brass beam block as shown in Figure 2.4. The beam blocks used have both thin and thick slots. The range of dimensions of these slots is shown in the figure. The use of thin and thick lines allows the maximum displacement (and thus the dynamic range) of the experiment to be increased. The reason is that the correlation technique cannot distinguish between intersections of lines with the same thickness, it is necessary to limit the maximum allowable displacement to one half of the spacing between like intersections. The use of two line thicknesses allows the maximum displacement to be doubled since an intersection between two thin lines will not correlate well with an intersection between two thick lines.

Using beam blocks does result in the loss of a large percentage of the laser beam energy. This does not pose a problem in the current work as the intensity levels are sufficient for the detectors used in the present study. Several previous works such as Hilbert and Falco, 1991 and Stier, 1994, have used an arrangement of offset mirrors in order to generate the grid of intersecting laser lines. This arrangement will cause the loss of a much smaller amount of the laser beam energy. Beam blocks, however, have the advantage of being very easy to manufacture so many different combinations of line spacing may be tried easily. This allows for the line thickness and spacing to be optimized for the particular experimental setup and field of view being examined. This optimization allowed between 600 and 800 velocity vectors to be measured over each individual measurement plane in the current work. This measurement density is more than 50% larger than previous MTV work that has been conducted in the Turbulent Mixing and Unsteady Aerodynamics Laboratory. Even with the loss of energy due to the use of the beam blocks, the energy provided by the laser was more than sufficient for the experiments.

2.4 Implementation of MTV in the mixing layer facility

MTV velocity measurements of the wake flow will be made in two planes as shown in Figure 2.5. The streamwise (x, y) plane allows the measurement of the (u, v) components of velocity along with the spanwise component of vorticity, ω_z, at a particular spanwise (z) location. The cross-stream (y, z) plane allows the measurement of the (v, w) velocity components along with the streamwise vorticity, ω_x at a particular streamwise (x) location. In the cross-stream plane, the mean flow is moving directly towards the camera. This work is the first time this type of measurement has been conducted using MTV. Figure 2.5 also shows the coordinate system used in this work. The origin of the coordinate system is at the center of the test section at the splitter plate tip.

Table 2.2 lists the locations of the streamwise wake measurements. Measurements are made in the center span ($z = 0$ cm) for streamwise locations 3 $cm < x < 20$ cm downstream of the splitter plate tip for all of the cases listed in Table 1. This is listed as "full" in the listing of forcing cases in Table 2.2. In order to study the effect of three-

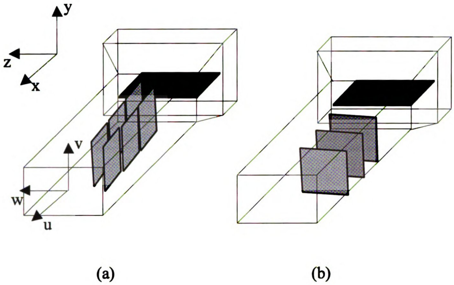

Figure 2.5: Sample measurement planes. (a) Streamwise planes. (b) Spanwise (end view) planes. Note that the origin of the coordinate system is at the center of the test section at the tip of the splitter plate.

Table 2.2: Streamwise measurement planes. Full and Reduced refer to the number of measurement cases.

Z (cm)	Streamwise Measurement Range(cm)	Forcing Cases
0	3 < x < 20	Full
-1.5	3 < x < 20	Reduced
-2	3 < x < 7	Reduced
-2.5	3 < x < 20	Reduced
-3	3 < x < 7	Reduced
-3.5	3 < x < 7	Reduced
-3.7	3 < x < 7	Reduced

Table 2.3: Spanwise measurement planes. Full and Reduced refer to the number of measurement cases.

X (cm)	Forcing Cases	X (cm)	Forcing Cases
3	Reduced	11	Full
3.25	Full	12	Reduced
4.25	Reduced	14	Reduced
5.25	Reduced	15.75	Full
6.5	Full	16.25	Reduced
7	Reduced	18.5	Reduced
8.5	Reduced	20.25	Full
10	Reduced	23.75	Reduced

dimensionality on ω_x, two additional streamwise planes, $z = -1.5\ cm$, $-2.5\ cm$ are measured with a reduced number of forcing conditions. This reduced set consisted only of the 6 Hz, 2.1%. 7.3%, 11.6%, and 13.3% forcing cases. Additionally, in order to gain more detailed information on the spanwise development of the interactions between the vortex tubes, the particular range of range $3\ cm < x < 7\ cm$, a total of *7* spanwise locations were measured with the reduced number of forcing cases.

In the cross-stream (y, z) plane, data will be collected in one half of the test section ($-4\ cm < z < 0\ cm$). Symmetry in the locations of both the instantaneous and mean streamwise structures result in the other half of the test section being identical to the portion measured. In order to determine the downstream evolution of the streamwise vorticity, measurements are made at several downstream locations as shown in Table 2.3. Five of those planes will be measured with the full set of forcing conditions and the remaining planes will be measured using the reduced set described above. In addition, several measurements will a

assum

Optic

and sp

that u

ultravi

are us

Optica

length

reflec

increas

series

the Fo

have a

Previo

sed to

complete

although

be reco

will also be made in the range $-3\ cm < z < 1\ cm$ in order to spot check the symmetry assumption.

Optical Experimental configuration

The optical setup used to generate the phosphorescent laser grid for the streamwise and spanwise measurement planes are shown in Figure 2.6. This arrangement is similar to that used in Gendrich, Koochesfahani, and Nocera, 1997. The beam from a pulsed ultraviolet laser (Lambda-Physik LPX 220i) passes through a pair of cylindrical lenses which are used to thin the rectangular shaped beam generated by the laser into a thin sheet. Optically, the pair of lenses is equivalent to one cylindrical lens with a much longer focal length. This sheet is then split into two portions with a nominally 50% transmittance, 50% reflectance beam splitter. These beams and are then reflected through focusing lenses to increase the breadth of the beam, and finally through the brass beam dividers to create a series of laser lines. The laser lines pass through the walls of the quartz test section and into the flow. The beams are carefully aligned so the lines from the two sides are in the same plane and form the necessary intersecting grid pattern. A sample grid experimental grid has previously been shown in Figure 2.4.

A two-camera measurement system which will be discussed later in this section is used to track the luminescence of the tagged line crossings. Two Pulnix 9701 charge coupled device (CCD) cameras are synchronized using a common synchronization generator. Although these cameras output their images in RS-170, interlaced format which simplifies the recording on image processing systems, the two fields are acquired simultaneously.

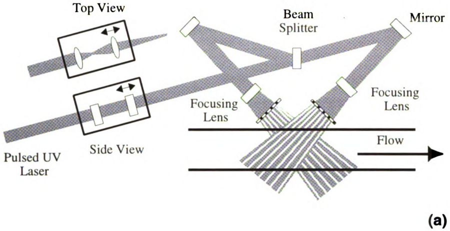

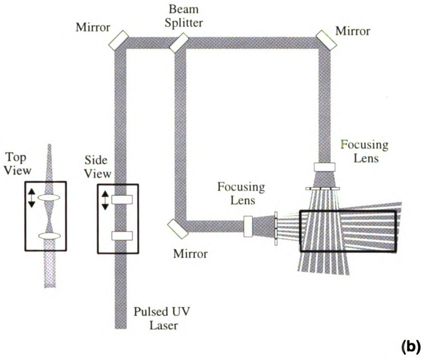

Figure 2.6: Optical arrangement for MTV measurements. (a) Streamwise plane. (b) Spanwise plane.

The

they

diffe

digit

by th

50 m

came

the ca

produ

corre

meas

13.5 c

facility

the di

a large

length

lens, a

200 m

butter

These cameras have a resolution of 768 horizontal pixels by 484 vertical pixels. However, they were digitized to a resolution of 512 pixels horizontally and 512 pixels vertically. The difference between the 484 vertical pixels on the camera and the 512 pixels recorded by the digitizer are filled in with zeros. The remainder of the 768 horizontal pixels are not digitized by the image processing system.

For the streamwise plane measurements, the cameras view the flow through a Nikkor 50 mm f/1.2 lens. With the working distances between the measurement plane and the camera a field of view of approximately *4 cm x 4 cm* to be examined. Using this lens and the cameras with a *0.5* ms shutter time, it was found that a delay time of $\Delta t = 5.4653\ ms$ produced delayed images with a sufficiently high signal to noise ratio to produce high quality correlation results. The maximum displacements found in the streamwise plane measurements was approximately *9* pixels. This corresponds to a velocity of approximately *13.5 cm/s*.

The spanwise plane images were recorded from the downstream viewport of the flow facility. As the distance from the downstream viewport to the image plane was larger than the distance from the camera to the image plane in the streamwise measurements, a lens with a larger focal length and consequently smaller aperture was needed. A Nikkor 105 mm focal length, f/1.8 lens was used. With the working distance in the experimental setup and this lens, a *4 cm x 4 cm* field of view was examined. In order to maintain high signal to noise ratio images, the delay time between the cameras was limited to $\Delta t = 4.00365\ ms$. The shutter time remained at *0.5 ms*. The maximum displacement measured in this plane is approximately *3* pixels, which corresponds to a velocity of about *5.5 cm/s*.

Sync

trac

the v

imag

field

which

the p

the s

exper

positi

of the

move

camer

along

The v

Rege

Riley

should

recess

53.55

Synchronization of experimental apparatus

In the two-camera MTV setup, the timing between the components is absolutely crucial. An error in the delay time between the two cameras will cause a bias error in all of the velocity measurements. It is also possible that improper timing could result in the digital image processor recording camera fields in the wrong order which could result in correlation fields being computed using intersections containing information occurring at different times which would have a significant impact on the measurement accuracy. It is also necessary for the pulsed laser to fire at the proper time in order for the molecules to be luminescent while the shutter of the cameras is open. Further, the phase averaging procedure used in these experiments, which will be described later in this section, require that the bellows control, position, and velocity signals are recorded at the proper time. Figure 2.7 shows a schematic of the setup used to synchronize the cameras, the pulsed ultraviolet laser, and the A/D converter.

A single synchronization generator is used to create the timing signals for both of the cameras. This ensures that the two cameras are recording images that are delayed an exact amount in relation to each other. The horizontal drive signal for the two cameras is common. The vertical drive signal is used to delay the cameras relative to each other. A Stanford Research Systems DDG535 digital delay generator is used to create the two vertical drives pulses with a fixed delay between them. These signals are then input into the cameras. It should be noted that when recording images in RS-170 (standard video) format, it is necessary to delay the vertical drive signal in units of the horizontal drive timing signal (63.55 μs). If the delay is not in units of this timing signal, it is possible to cause the digitizer

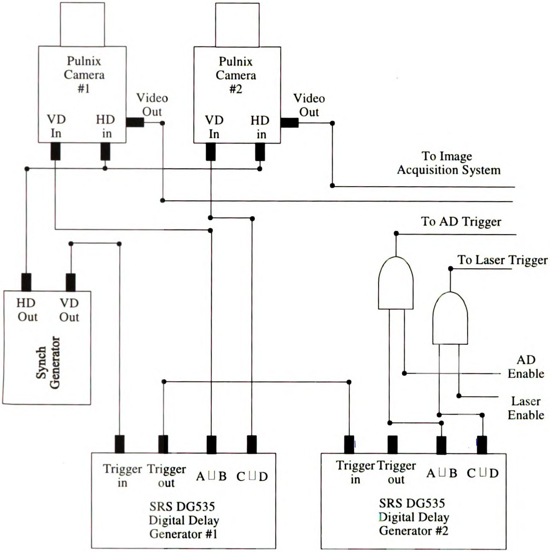

Delay Generator #1 Settings

Trigger:	External
Trigger Threshold:	-1.5 V
Trigger Slope:	-
Trigger Termination:	high Z
All output loads:	high Z
All output voltages:	TTL/Normal
Delay A:	T0
Delay B:	T0 + 0.57 ms
Delay C:	A+n*63.55 μs
Delay D:	C + 0.57 ms

Used for camera vertical drives.

Delay Generator #2 Settings

Trigger:	External
Trigger Threshold:	1.5 V
Trigger Slope:	+
Trigger Termination:	high Z
All output loads:	high Z
All output voltages:	TTL/Normal
Delay A:	T0+16.721 ms
Delay B:	A + 2 ms
Delay C:	T0 + 16.721 ms
Delay D:	C + 2 ms

Used to trigger laser at 30 Hz.

Figure 2.7: Timing Schematic for MTV experiments.

to reverse the order of the fields in one of the cameras. Delaying in units of the horizontal drive signal does not have a significant impact on the current experiments as the period of this signal is small relative to the typical delay times desired in these experiments (*3-5 ms*).

The second DDG535 delay generator displayed in Figure 2.7 is also triggered by the vertical drive control signal of the synchronization generator. This unit is set to provide a 30 Hz control signal to fire either a *90 mJ* pulse (streamwise plane measurements) or a *110 mJ* pulse (cross-stream plane measurements) from the Lamda-Physik LPX 220 laser and the trigger the analog to digital converter. The timing of the second delay generator is set such that the laser fires and the AD converter triggers just prior to the beginning of the image from the undelayed camera. Thus, the undelayed camera records a phosphorescent image.

Two camera measurement system

The experiments reported in this work will use the camera measurement system that has been used in Cohn *et al.*, 1995, Gendrich, Bohl, and Koochesfahani, 1997, and Gendrich, Koochesfahani, and Nocera, 1997. In this system, the two cameras are placed at a 90 degree angle from each other. Both are looking directly into a cube beam splitter. In this manner, both of the cameras receive half of the intensity of the grid crossings. Using the two camera system, it is extremely important for the relative alignment between the two cameras to be known in order for it to be eliminated from the flow measurements. In the current experiments, the relative displacement between the two cameras is known and steps were taken in order to minimize this alignment displacement field.

In order to align the two cameras relative to each other, the undelayed cameras is mounted onto a three-axis rotational stage system and the delayed camera is mounted to a three-axis translational stage system. The initial displacement field between the two cameras is measured by acquiring images of the laser grid with zero delay between the two cameras. Since both images are recorded shortly after the laser fires, the signal to noise ratio of the images is very high and the displacement field between the two images can be measured with accuracy that exceeds *0.1* pixel subpixel accuracy previously quoted for the present experiments. For the results presented here, *40* images of the undelayed field are measured and the resulting displacement field is averaged. Since averaging reduces the uncertainty in a measurement by a factor of (number of points)$^{-1/2}$, the initial camera displacement field should be accurate to better than *0.016* pixels.

Before each experimental run is started, the initial displacement field is measured and adjusted such that the maximum displacement between the grid intersections of the two cameras is less than *1* pixel. Typically, all of the measurement locations have a displacement less than *0.9* pixel and over half have a displacement of less than *0.5* pixel. This measurement is repeated at the end of each experimental run to confirm that the cameras have not shifted during the course of the measurements.

Image acquisition and processing

One thousand realizations of the velocity field are measured for each measurement condition. As each realization is separated by *1/30*th of a second, this corresponds to *200* forcing cycles of the 6 Hz case. Between *600* and *800* velocity vector measurement are made in each realization over the *4 cm x 4 cm* field of view. This corresponds to a mean spacin

spatia

Multi

locati

field c

be lin

record

system

proces

proces

RS-17

video

camer

imag

horiz

vide

at E

imag

from

spacing of *1.5 mm* between standard resolution velocity measurements. A set of higher spatial resolution measurements was also made and will be discussed in section 2.6. Multiple experiments were conducted at the same forcing conditions at different downstream locations because the total streamwise measurement range is significantly larger than the field of view that can be measured in a single experimental realization,. These data sets can be linked together because the phase time reference is known from the forcing signals recorded by the A/D converter.

The images from the two cameras were recorded by a dual Trapix-Plus acquisition system manufactured by Recognition Concepts Inc. This system contains two image processing systems which are controlled by a single imbedded controller. Each image processing system contains its own disk array that is capable of recording over 9 minutes of RS-170 video data in digital format. This system is capable of recording up to 10 bits of video data, however, only 8 bits of resolution were recorded as that is the limit of the cameras being used in these experiments. The use of the beam splitter to record the two images causes one of the images, the undelayed one in these experiments, to be flipped horizontally during image acquisition. Thus, it was necessary to horizontally flip the undelayed images within the image processing system in order to orient both images properly.

After recording, the images are stored in "tar" format on 8 mm backup tapes using an Exabyte 8505 tape drive. These tapes can store up to *16* GB of data. The unprocessed images from each forcing condition at each downstream location occupy *0.5* GB of space, so many forcing conditions were placed on each tape. The data were processed directly from these tapes. Processing of the experimental data is performed using an in-house code developed over the past several years. A four-processor Silicon Graphics Origin 200 is used as the primary data processing device. Each processor of this machine is capable of processing *40* MTV velocity vectors/second. Thus, each data set takes approximately *5* hours to process.

2.5 Post-processing of MTV data

A block diagram of the procedure used to process the measured velocity data can be found in Figure 2.8. Once the velocity components are measured using the correlation procedure and the zero delay reference grids are subtracted as described above, it is necessary to rescale the data from the original pixel units of the acquired images into physical units. This was done using the top and bottom edges of the test section as reference points in order to determine the distance scale factors. The distance between these two edges is *4 cm* and they were visible in all of the recorded images.

After the images are re-scaled into physical units, it is necessary to place the measured points onto a regular grid. This is necessary so that flow variables such as vorticity and strain rate can be computed via a finite difference technique. Unlike data acquired using PIV, the original measurement field is not regularly spaced. Furthermore, the best estimate for the velocity field acquired by any tracking-based measurement technique is actually at a location midway between the initial and final location of the feature being tracked. Thus, data from many whole-field techniques (including PIV) must be re-mapped onto a regular grid. (Spedding and Rignot, 1993).

Several authors including Agui and Jimenez (1987), Spedding and Rignot (1993), Abrahamson and Lonnes (1995), Fouras and Soria (1998), and Luff, *et al.* (1999) have

Figure 2

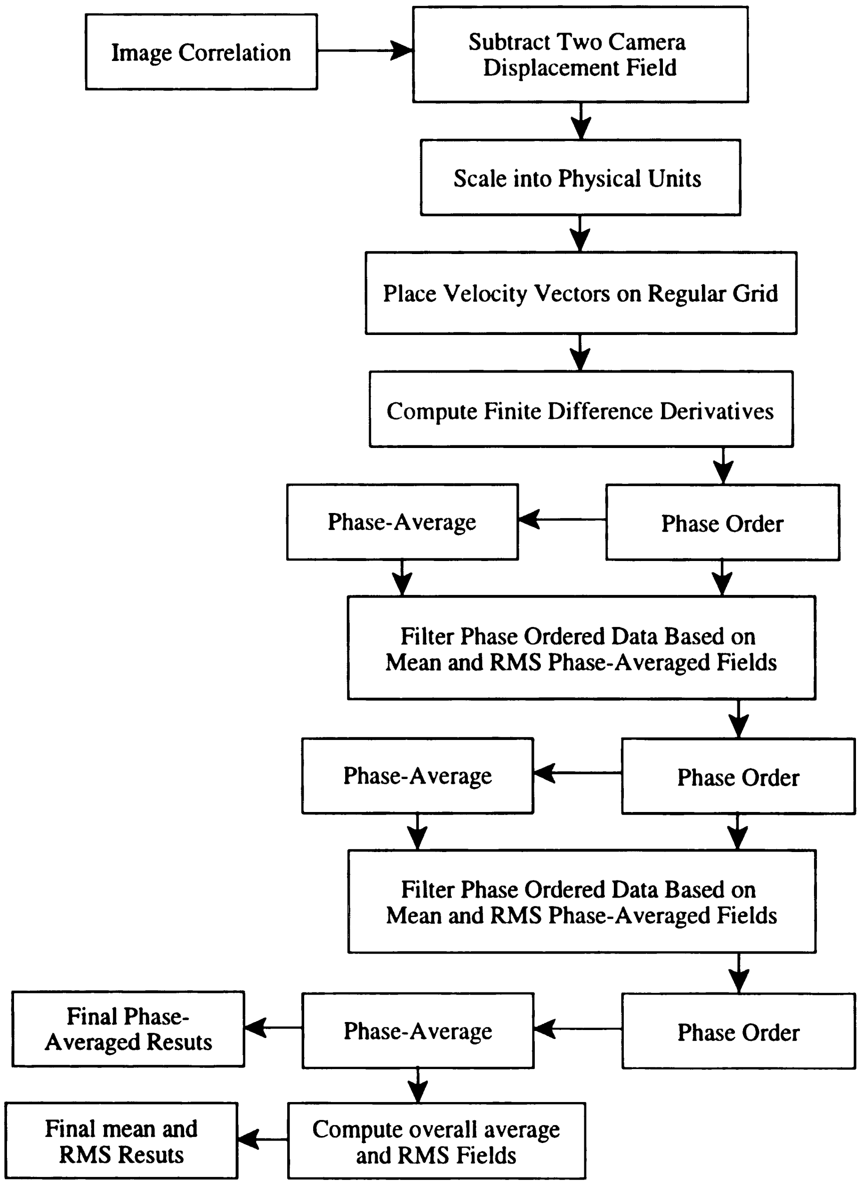

Figure 2.8: Block diagram of the MTV processing procedure.

examined different methods for the interpolation of velocity measurements and the computation of vorticity. In the current work, the remapping onto a regular grid of measurements is made by performing a local least squares fit of the irregularly spaced velocity measurements to a 2nd order polynomial. A minimum of *9* points are used in the least square fit. For a 2nd order polynomial, *6* is the minimum number of points needed to perform the analysis. When the measurements are interpolated onto a regular grid, the spacing between points on the regular grid, h, is kept at approximately the mean spacing between points in the irregular grid, δ. Thus, no information on the spatial structure of the flow is lost, and no new information is unintentionally generated by the interpolation procedure. The spatial derivatives are then computed using a 2nd order central finite difference method (4th order accurate).

Appendix A contains more complete information on the use of a polynomial least-squares fit to remap data onto a regular grid and on several methods which can be used to calculate vorticity. These results show that a mean bias error, caused by spatial filtering of the data, exists in the vorticity measurements, which will cause the peak vorticity values to be underestimated. The bias error is extremely sensitive to the normalized measurement density, the ratio of a length scale of the flow, L to δ. Studies have shown that if L/δ is not sufficient, the peak values of vorticity can be underestimated by over 40%. In the present study, these effects were examined by making an additional set of measurements at twice the standard resolution which will be discussed in section 2.6. It should be noted that simulations show that a small amount of overshoot of vorticity is also found in the range from between one and two core radii from the center of the vortex.

Extrapolation into regions where there are no measurement points can greatly

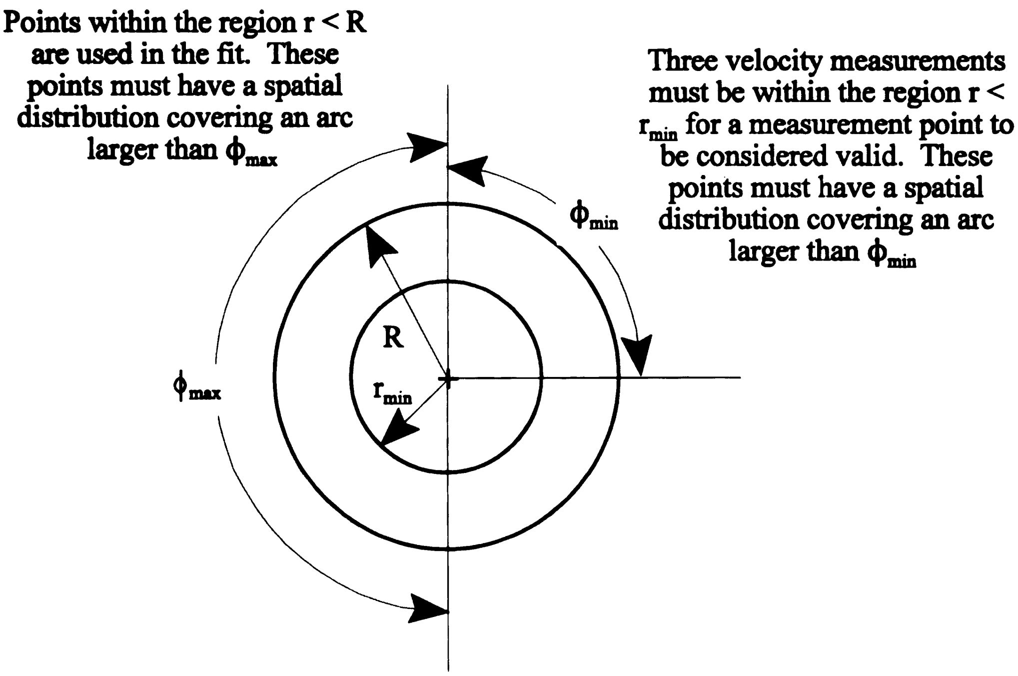

Figure 2.9: Conditions for selecting a regular grid point.

increase the error in the process of placing points onto a regular grid. In order to prevent this, additional criteria were placed on each regular grid point before a valid velocity vector was placed at that point. Figure 2.9 shows these conditions graphically. First, all points on the regular grid are required to have at least *3* actual measurement points within a radius of r_{min}. In order to optimize the number of valid points, $1.67\delta < r_{min} < 2\delta$. A factor greater than unity is necessary to account for variations in the local spacing of points. Furthermore, it was required that these points were spatially distributed such that at least these three points were distributed over an arc of at least *90* degrees. In addition, it was required that the points used in the fit are distributed in an arc of at least *180* degrees around the regular grid point.

The results presented in Appendix A also show that the bias error is also affected by the size of the region, *R*, from which velocity measurements are used in the local fit. If the

region is too small, there will not be sufficient numbers of measurement points to perform the least squares fit. If the region is too large, the bias error is increased. In order to optimize the results, the size of this region varied in the range, $2.33\delta < R < 2.8\delta$.

The data rate of MTV velocity measurements is limited by the framing rate of the cameras. For the cameras used in these experiments, this spacing is approximately *33.3 ms.* The period of the forcing signal is *167 ms.* This corresponds to only *5* measurements per period. This flow, however, is extremely periodic in nature and lends itself very well to phase averaging. The repeatability of the flow will be shown in Chapters 3 and 4. The phase averaging is accomplished using the command input signal to the electromagnetic shaker recorded by the AD converter. This signal is first phase ordered by minimizing the RMS between measurements that are close in phase after the appropriate reference frequency is applied to the signal. Zero phase is arbitrarily selected as the positive zero crossing of the forcing signal. Since each AD measurement of the command signal corresponds to a velocity field measurement, the MTV velocity information can be phase ordered based on the same reference frequency. After phase ordering the velocity field information, the data set is divided into *64* bins with a width of *1.6%* of the period. All data that fall within a bin are averaged to form the velocity field at that phase, ϕ. The value of ϕ will be normalized such that $0 < \phi < 1$. If the phase-averaged velocity field is representative of the instantaneous field at a particular point in time, this procedure yields a set of data in which consecutive phases can be thought to be separated by *2.6 ms.* In Chapters 3 and 4, it will be shown that the phase-averaged field is representative of the instantaneous results for a large portion of the collected data.

In addition to increasing the data rate of the measurements, phase averaging also

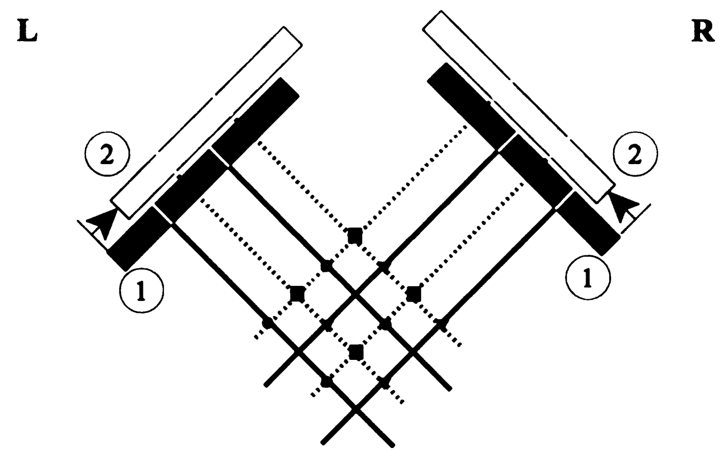

Line intersections	created when beam blocks are in there initial location.
▼	created when beam block L is moved from position 1 to 2.
■	created when beam block R is moved from position 1 to 2.
●	created when beam block L is moved from position 2 to 1.

Figure 2.10: Movement of beam blocks to increase grid measurement density.

reduces the measurement uncertainty. Since there are, on average, nominally *16* instantaneous realizations in each phase bin, the measurement error will be reduced by a factor of *4*. This corresponds to 95% confidence interval of ±*0.038 cm/s* for the streamwise plane (u, v velocities in the x, y plane) and ±*0.05 cm/s* for the cross-stream plane (v, w velocities in the y, z plane). A standard uncertainty analysis for a 2nd order finite difference technique reveals that the uncertainty in the derivative quantities, such as vorticity, is equal to $\frac{1.34}{h}\delta u$, where h is the grid spacing used for the differentiation and δu is uncertainty in the velocity measurement. Thus, the 95% confidence interval for the phase-averaged spatial derivatives can be found to be ±$0.4\ s^{-1}$ for the streamwise plane and ±$0.45\ s^{-1}$ for the cross-stream plane. If the error distribution is Gaussian, it can be shown that the width of the 95% confidence interval is twice that of the standard deviation. Thus, the standard deviation of these errors is ±*0.019* cm/s for the streamwise plane velocities, ±*0.025 cm/s* for the cross-stream plane velocities. For the spatial derivative quantities, the standard deviations for the streamwise and cross-stream plane are $\pm 0.2\ s^{-1}$ and $\pm 0.23\ s^{-1}$ respectively.

The phase averaging process is also used as a means of filtering the velocity data of spurious bad vectors. As the phase average for each velocity point is calculated, the root mean square of the velocity values in that bin is also computed. All velocity values that are more than *3* times the RMS value away from the mean are replaced by the mean value for that location. Then, the averaging process is repeated. For all of the measurements conducted, no more than 1% of the vectors at any measurement time were replaced. After the substitution, the phase averaging process is repeated.

2.6 Post-processing of higher density data

Higher spatial density measurements for the 6 Hz, 11.6% forcing case were made for several measurement locations in order to determine the effect of the spatial filtering inherent in the measurements. These experiments were conducted by making four separate measurements of this forcing condition and adjusting the location of the beam blocks as shown in Figure 2.10. This causes individual velocity measurements to be made at slightly different locations. The displacement of the beam block is approximately ½ of the spacing between the initial measurement locations. During the course of these measurements, the bellows forcing is not stopped. This technique effectively halves in each direction the mean spacing between velocity measurements.

To take advantage of the increased measurement density, the procedure used in the standard density measurements cannot be used. If this procedure were used, the increased spatial data density information would not be used in the regularization procedure. In order to guarantee that this information is used, the data from all four sets are first phase ordered. Then, the measurement planes from all four data sets that are within each phase bin are combined so that they are considered one super-measurement plane. This plane consists of the approximately *16* realizations from each of the four data sets that occur within the phase bin being examined.

After all of the irregularly spaced velocity measurements at a particular phase are placed in their appropriate phase bin, the data is then placed on a regular grid using the 2nd order polynomial described previously. However, a minimum of *120* points are used in the fit, rather than 9 used in the standard measurements. With the large increase in the number of measurement points inherent in this technique, the maximum radius from which velocity measurements are used for the fit, R, is decreased to 2.33δ which should further increase the measurement accuracy. It will be shown in the following chapters that the high density measurements result in a significantly larger value of the peak vorticity. These increases are consistent with the increases in peak vorticity levels due to an increase in L/δ as shown in Appendix A.

Chapter 3

Streamwise Measurements of a Wake Forced Near its Natural Frequency

As stated in the introduction, few studies of the effect of forcing amplitude on the vorticity distribution and other flow characteristics have been conducted in a confined wake flow. In this chapter, the streamwise flow characteristics of the wake forced at 6 Hz will be examined and discussed. First, the phase-averaging procedure will be examined and results will be presented showing the rationale for considering the phase-averaged data to be equivalent to the "instantaneous" data. The second section will then describe the mean flow properties at center span and the third section will examine the instantaneous (phase-averaged) results at this spanwise location. The fourth section will examine the flow properties of several different spanwise locations, and the final section will compare data acquired at the standard density measurement results with measurements made at a higher spatial density in order to determine the effect of spatial filtering on the results.

3.1 Phase-averaging of streamwise measurement plane data

As has been described in Chapter 2, the measured data have been phase-averaged in order to both increase the effective temporal sampling rate and reduce the measurement error. Figure 3.1 shows the phase ordered (u, v) velocities in the free-stream region of the flow at two representative downstream locations in the flow for the 11.6% forcing case. Each plot

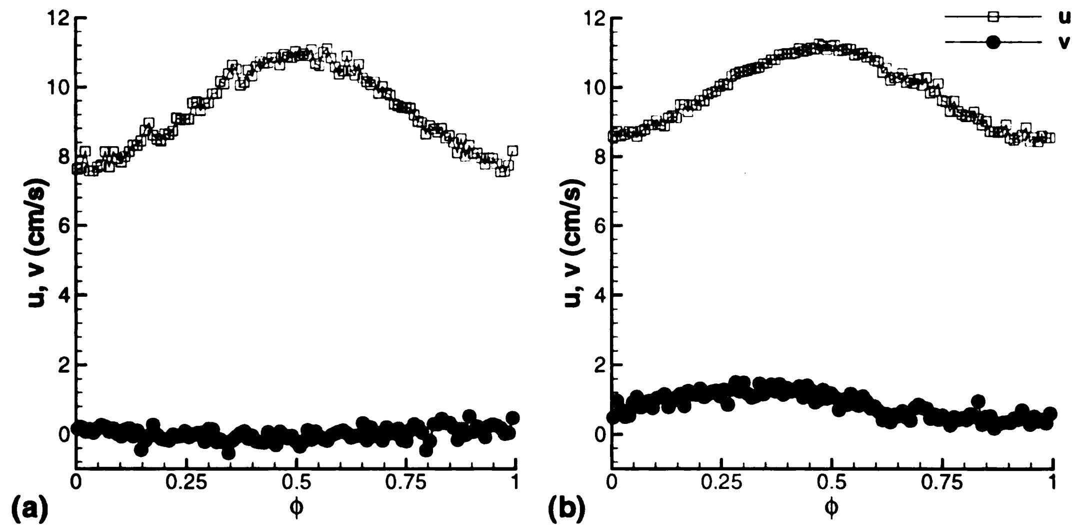

Figure 3.1: Phase ordered free-stream velocity fields for two downstream locations in the forced wake. (a) x = 5 cm. (b) x = 18 cm. The small undulation in the *v*-component of velocity at x = 18 cm is the signature of the vortex cores passing this downstream location at the *y* location of the measurement.

is composed of approximately 1000 measurement points. However, in order to make the plots more readable, only every 10th point is shown. Figure 3.1a shows a measurement station *5 cm* downstream of the splitter plate tip while Figure 3.1b shows a measurement station *18 cm* downstream of the splitter plate. The *u*-component of velocity in the upstream example (Figure 3.1a) has a sinusoidal appearance, which is as expected for the free-stream region of this flow forced with a sinusoidal waveform. The *v*-component shows very small velocities. The collapse of both velocity fields to the expected instantaneous values at these locations is excellent. The downstream example shows similar features as the upstream example. In fact, the collapse of the *u*-component of velocity to the expected velocity at this location appears to be even better than that of the upstream example. The small undulation in the *v*-component of velocity is the signature of the vortex cores passing this downstream location at the *y* location of the measurement.

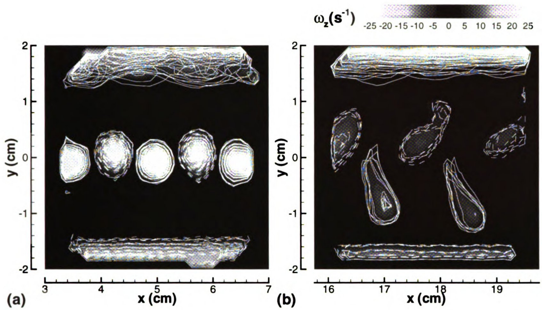

Figure 3.2: Phase-averaged vorticity field (flooded contour) along with vorticity contour lines of 6 instantaneous realizations overlaid on top. Dashed contour lines indicate negative values of vorticity and contour levels are $\pm 4\ s^{-1}$, $\pm 8\ s^{-1}$, ..., $\pm 24\ s^{-1}$. (a) $3 < x < 7\ cm$. (b) $15.75 < x < 19.75\ cm$.

The collapse of the instantaneous realizations applies as well to the vorticity field. Figure 3.2 shows flooded contour plots of the phase-averaged vorticity field at one representative phase for the region $3 < x < 7\ cm$ and $15.75 < x < 19.75\ cm$. Overlaid on top of the flooded contours are vorticity contour lines of several of the instantaneous realizations used in computing the phase-averaged vorticity. In Figure 3.2a, containing the upstream results, the spatial overlap between the instantaneous and phase-averaged is nearly perfect in the central region of the test section. On the bottom and top of the section, there are some variations due to the top and bottom wall boundary layers. Figure 3.2b shows the instantaneous vorticity contour lines overlaid on top of the phase-averaged field for the farthest downstream regions examined in this study. It can be seen that the instantaneous vorticity field does not line up with the phase-averaged field as well as the upstream example. This is caused by a small amount spatial wandering of the vortex core from realization to realization. It is also noted that the spatial distribution of the vorticity field (i.e., the elongated shape) is very similar in all of the realizations.

Two quantities will be used to quantify the numerical differences between the vorticity values among the various realizations within each phase bin; namely $(<\omega_z>_{rms})_{peak}$ and $(<\omega_z>_{rms})_{max}$ will be used for this purpose. The former is defined as the RMS among the vorticity values in the instantaneous realizations at the location of peak vorticity, which is typically the center of the vortex core in this study. The latter is defined as the peak value of the RMS among the vorticity values in the instantaneous realizations at any point in the measurement field. These same two quantities will be used in Chapter 4 to examine the numerical difference between the realizations for the streamwise vorticity measurements.

For the 11.6% forcing case that is shown, the maximum value of the spanwise vorticity is $40\ s^{-1}$. Within the phase bin shown, $(<\omega_z>_{rms})_{peak} < 1\ s^{-1}$. This value is approximately equal to the uncertainty in the vorticity measurement caused by the random error inherent to the measurement technique. Examining all of the phase bins, $(<\omega_z>_{rms})_{max}$ = 2.5 s^{-1}. This is likely due to the small amount of spatial drift in the location of the vortex cores which was previously mentioned. This can result in large deviations in regions of high gradient. Thus, it is felt that the phase-averaged field is an accurate representation of the instantaneous result.

In this downstream region, the peak vorticity levels have decreased to approximately 10 s^{-1}. However, the values of both $(<\omega_z>_{rms})_{peak}$ and $(<\omega_z>_{rms})_{max}$ remain nearly identical to the upstream case with values equal to 1 $s^{-1}$and 2.5 s^{-1} respectively. Again, the spatial location where $(<\omega_z>_{rms})_{max}$ is near the edges of the vortical structures. The variation from realization to realization, however, is more noticeable since the peak vorticity values have decreased by a factor of four. Even with the increased spatial wandering, it is believed that the phase-averaged results provide a good estimate of both the spatial location and numerical value of the instantaneous field measurements. This allows the phase-averaged results to be used as if they are the instantaneous results.

3.2 Mean and RMS flow properties at center span

Mean free stream velocity

Flow characterization experiments were conducted in the center span of the test section in order to determine the basic streamwise structure of the flow. First, the mean quantities of this flow will be examined. Figure 3.3 shows a plot of the mean streamwise velocity of this flow versus y location for the unforced case as well as for several of the 6 Hz forcing cases at $x = 4, 11,$ *and* $17\ cm$. The free-stream velocity for all cases is approximately *9.4 cm/s*. In general, at upstream locations, the effect of forcing is to reduce the wake deficit, as measured by the difference between the free stream velocity and the smallest velocity in the wake. At $x = 4\ cm$, the wake velocity deficit for the unforced case is more than twice the deficit of the forced cases. However, at locations farther downstream, this is not necessarily the case. At $x = 11\ cm$, the magnitude of the deficit for the unforced case is approximately the same as the forced cases, and at $x = 17\ cm$, the forced deficit is larger than the unforced deficit. The 13.3% amplitude forcing case is interesting because for all downstream locations, the deficit appears to remain nearly constant. The value of the deficit is also much smaller than the deficit of any of the other forcing cases.

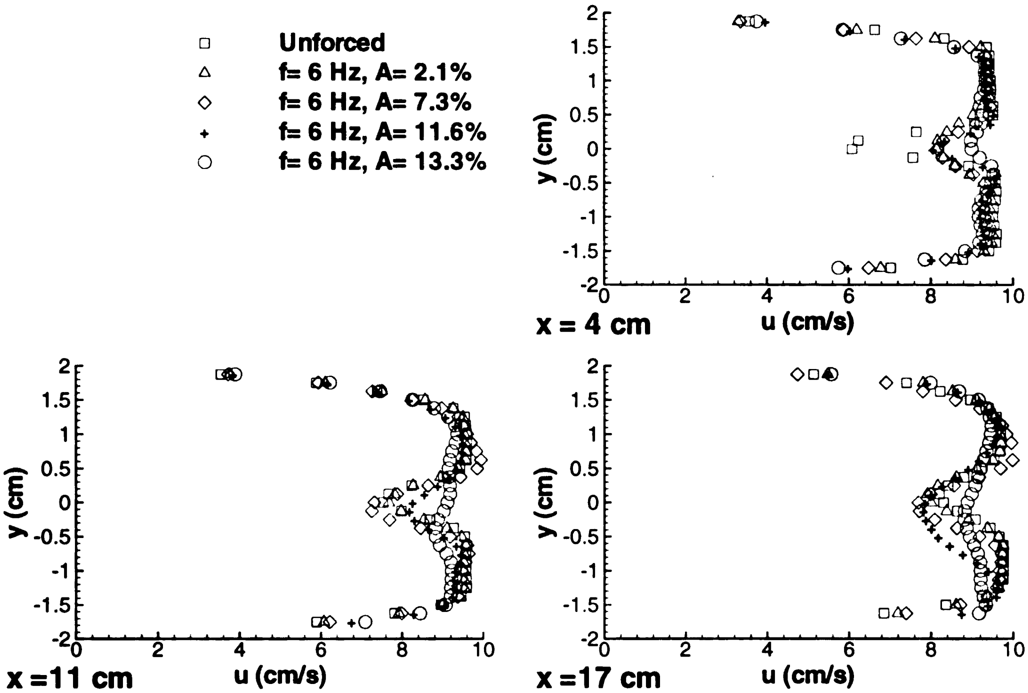

Figure 3.3: Streamwise velocity profiles at $z = 0$ *cm* for several forcing amplitudes at *3* streamwise locations.

Momentum Thickness

The momentum thickness across the layer is also used to quantify the total momentum deficit in the flow. The momentum thickness is computed according to:

$$\theta(x) = \int_{wake} \frac{\overline{u}(x,y)}{u_0(x)}\left(1 - \frac{\overline{u}(x,y)}{u_0(x)}\right) dy.$$

The value of u_0 is chosen to be the average of the free stream velocities in the upper and lower stream at the x location where θ is computed. The value of the free stream velocity of the two streams typically differ by less than *2%*. As defined, θ will almost always be positive for wake type flows, however negative values of θ have been noted in the wake of an oscillating airfoil by Koochesfahani (1989). The momentum thickness can be thought of as

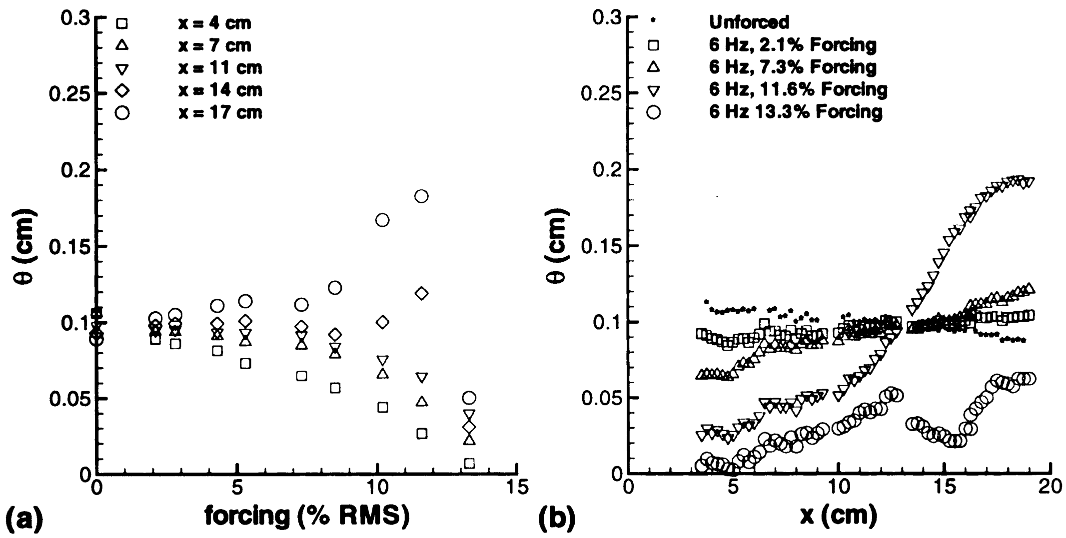

Figure 3.4: Momentum thickness as a function of (a) forcing amplitude and (b) downstream location.

one component of the drag on a hypothetical flat plate upstream of the region being measured. A second important term will be related to the non-uniform pressure distribution generated by the lower pressure present in the cores of the streamwise vortices. Since the drag on this hypothetical plate must be constant, an increase in the momentum thickness at one spanwise location must be accompanied either by a decrease at others or by changes in the pressure conditions. Note that negative values of θ have been previously seen in studies of the wake of oscillating airfoils (Koochesfahani, 1989) where they were inferred to be related to a thrusting condition on the airfoil.

Figure 3.4a shows a plot of the effect of forcing amplitude on the momentum thickness at several different downstream locations. For the farthest upstream location ($x = 4\ cm$), the momentum thickness generally increases as forcing amplitude is increased. The 13.3% forcing amplitude is an exception. As noted in the mean profiles, the wake deficit for the 13.3% amplitude is very small at all downstream locations, which results in a small value for θ. For locations farther downstream, such as $x > 14\ cm$, this trend reverses and increases in the forcing amplitude result in a decrease in θ.

Figure 3.4b shows the behavior of the momentum thickness for the unforced and three forcing cases with respect to downstream location in more detail. For the unforced case and the 2.1% and 7.3% forcing amplitudes, θ remains relatively constant with downstream location and has a value that is approximately *0.1 cm*. The small decrease in the unforced case is likely the result of the slight increase in free stream velocity caused by the growth of the sidewall boundary layers. For the 11.6% forcing case, the momentum thickness increases dramatically with downstream distance. Initially, its value is *0.03 cm.* By *17 cm* downstream, θ has increased to nearly *0.2* cm. Since the momentum thickness is proportional to the drag of the plate, which for each forcing case is constant in the mean, the value of θ must either decrease at other spanwise locations or the pressure conditions must change in order for the drag to remain constant. In section 3.4, it will be shown that the former condition is at least partially satisfied. It is also likely that the latter condition will hold as well since the size of the vortex cores is expanding, which will decrease the absolute value of the pressure within the core.

The 13.3% forcing case maintains a value that is always less than the momentum thickness for all other cases. In the upstream region, this value is almost zero. It increases slightly as the downstream distance increases, however, by *17 cm* downstream, it is still less than the *0.1* value found in the unforced flow.

Velocity RMS fields

Figure 3.5 shows a contour plot of the root mean square of u_{rms} and v_{rms} for the unforced and the 11.6% forcing amplitude cases. It is interesting to note that in the forced case shown in Figure 3.5b, the u_{rms} field is neither uniform nor monotonically decreasing in the streamwise direction. Rather, there is a distinct periodicity between regions of large and small RMS in both the streamwise (x) and the cross-stream (y) direction. This periodicity is seen in the u_{rms} for all of the forced cases, however, decreased perturbation amplitude decreases the magnitude of the effect. This periodicity is not seen in the u_{rms} field of the unforced case in Figure 3.5a. At the same transverse (y) location, the streamwise spacing between locations of maximum (or minimum) values of u_{rms} is the wavelength of the forcing perturbation. Locations of local minima in the RMS field on the one side of the layer are vertically aligned with regions of local maxima of the RMS field on the opposite side. This pattern is very different from what is seen in unconfined forced wake flows, such as in the wake of an oscillating airfoil studied by Koochesfahani (1989).

The v_{rms} field for the unforced and 11.6% forcing cases is shown in Figure 3.5c and 3.5d. In the unforced case, no v_{rms} is seen in the region $x < 8\ cm$. At locations farther downstream, a weak region of v_{rms} is found in the center of the test section. For the forced case, the strongest v_{rms} is seen in the center part of the test section in the region $x < 10\ cm$. Examining locations closer the top and bottom walls of the test section causes a decrease in v_{rms}. Farther downstream, v_{rms} weakens and begins to spread towards the sidewalls. This pattern is created by an increase in the vertical spacing between the regions of $<\omega_z>$ which will be shown in section 3.3.

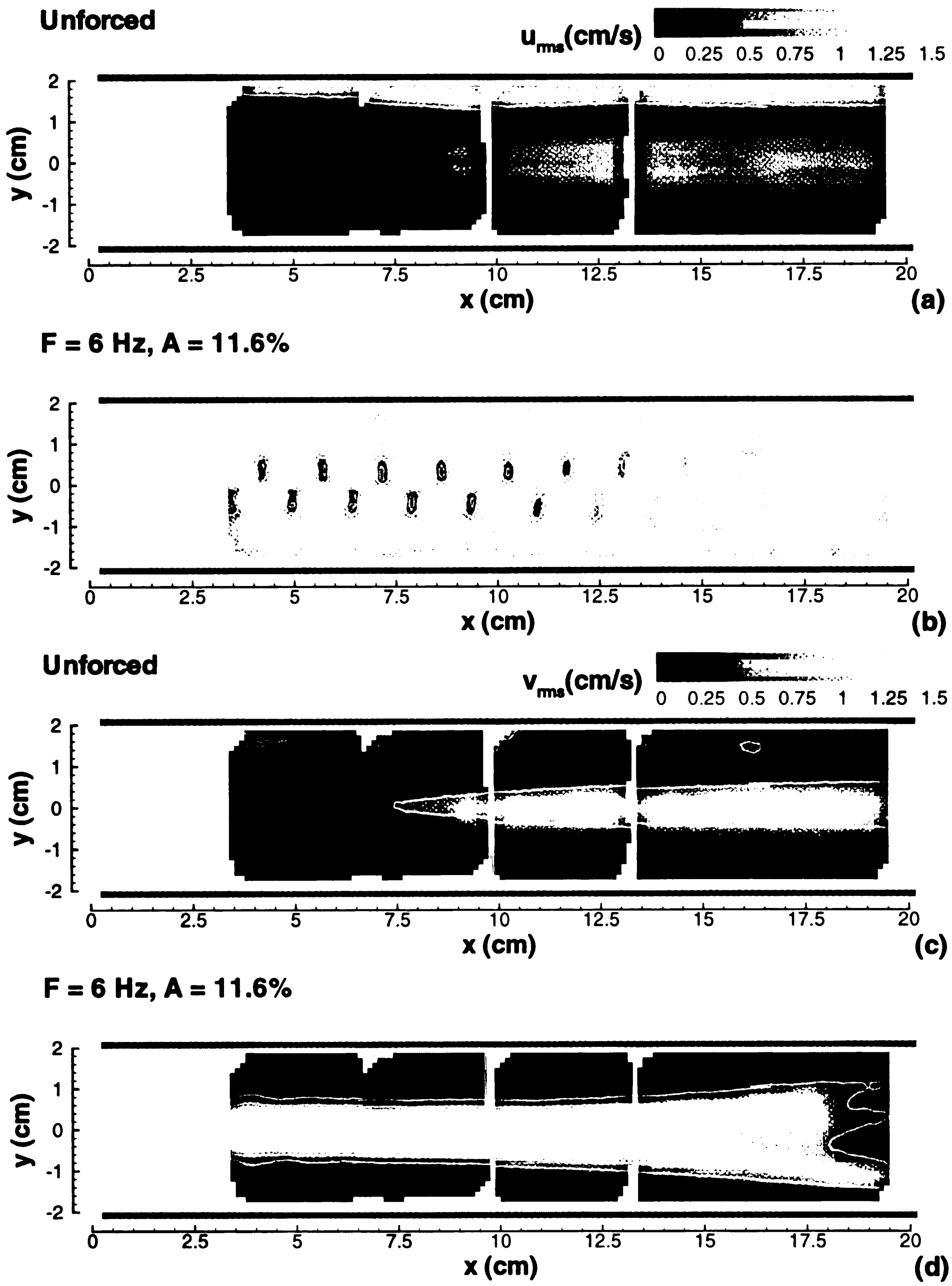

Figure 3.5: RMS of streamwise (u) and spanwise (v) velocity for the unforced and 11.6% forcing amplitude cases. (a) u_{rms} for unforced cases. (b) u_{rms} for 11.6% forcing case. (c) v_{rms} for unforced case. (d) v_{rms} for 11.6% forcing case. Contour levels are *0.3 cm/s, 0.6 cm/s, ..., 1.5 cm/s.*

This pattern in the u_{rms} field can be explained by the phase difference between the forcing and the resulting vortex shedding response. In the model, shown pictorially in Figure 3.6, the vortices are assumed to be inviscid point vortices and it is assumed that the free stream velocity can be described by $U_{fs} = u_0 + \zeta u_0 cos(2\pi ft)$ where u_0 is the mean velocity, f is the frequency of the perturbation, ζ is the forcing level and U_{fs} is the instantaneous free stream velocity. It is further assumed that vortices are shed at a distinct phase, $0 < \phi < 1$, within the forcing cycle and convect downstream at nearly a constant velocity. It should be noted that it is not necessary for the convection speed to be constant for this model. For the following argument, a negatively signed vortex is shed at a phase of $ft = \phi$ and a positively signed vortex is shed ½ cycle later at a phase of $ft = \phi + 0.5$. Only the effect of the induced velocity due to the closest vortical structure will be considered and the effect of the image vortices in the top and bottom walls are ignored in this model. In the explanation of the model, it is assumed that the vortex convection speed is constant. This requirement is not necessary and is only used to simplify the explanation.

A negatively signed vortex will pass the streamwise location of $x = n\lambda - \phi\lambda$, where λ is the forcing wavelength and η is any integer, at a phase time of $ft = \eta$. At this phase, the flow free stream velocity is a maximum, $U_{fs} = u_0 + \zeta u_0$. Similarly, when the positively signed vortex passes this point, the phase time is $ft = (\eta + ½)$ and the free stream velocity is at its minimum value, $U_{fs} = u_0 - \zeta u_0$. Examining point **A** from Figure 3.6, which is located above the vortex street, it can be found that when the negatively signed vortex passes this point, the velocity at this point is $u_{A,0} = U_{fs} + U_{induced} = u_0 + \zeta u_0 + \Gamma/2\pi r$, where $U_{induced} = \Gamma/2\pi r$, is the induced velocity due to the vortex, Γ is the circulation of the vortex, and r is

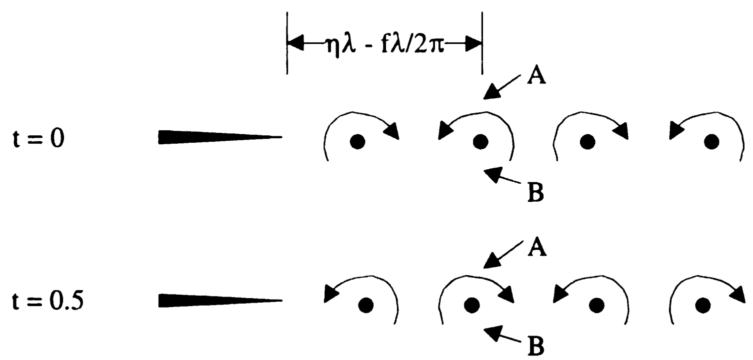

Point A:

At $t = 0$; $u_{A,0} = U_{fs} + U_{induced} = u_0 + \zeta u_0 + \Gamma/2\pi r$

At $t = 0.5$; $u_{A,0.5} = U_{fs} + U_{induced} = u_0 - \zeta u_0 - \Gamma/2\pi r$

Peak-Peak Variation:

$2(\zeta u_0 + \Gamma/2\pi r)$

Point B:

At $t = 0$; $u_{B,0} = U_{fs} + U_{induced} = u_0 + \zeta u_0 - \Gamma/2\pi r$

At $t = 0.5$; $u_{B,0.5} = U_{fs} + U_{induced} = u_0 - \zeta u_0 + \Gamma/2\pi r$

Peak-Peak Variation:

$2(\zeta u_0 - \Gamma/2\pi r)$

Figure 3.6: Effect of the phase relationship between flow forcing and vortex shedding on the streamwise velocity fluctuations in the forced wake.

the distance between the vortex and the point **A**. Similarly, when the positively signed vortex passes ½ a cycle later, the velocity at this point is $u_{A,0.5} = U_{fs} + U_{induced} = u_0 - \zeta u_0 - \Gamma/2\pi r$. Thus, at point **A**, the velocity will vary in the peak to peak range of $2(\zeta u_0 + \Gamma/2\pi r)$.

Examining point **B** located below the vortex street, when the negatively signed vortex passes, the velocity is $u_{B,0} = U_{fs} + U_{induced} = u_0 + \zeta u_0 - \Gamma/2\pi r$, whereas when the positively signed vortex passes, the velocity is $u_{B,0.5} = U_{fs} + U_{induced} = u_0 - \zeta u_0 + \Gamma/2\pi r$. Thus, the peak to peak velocity variation at point **B** is $2(\zeta u_0 - \Gamma/2\pi r)$, which is less than the peak to peak variation at point **A**. Consequently, the RMS value at point **B** will be less than that at point **A**. Similarly, at a point $\lambda/2$ either upstream or downstream, the situation will be reversed and the "large" deviation will be below the vortex array while the "small" deviation will be above the array.

Examining the u_{rms} data from the various forcing amplitudes, it is apparent that the locations of the minima occur at different spatial locations for the different forcing amplitudes. This location is an indication of an amplitude dependance in the phase when the spanwise vortex cores shed from the splitter plate tip. From this spatial information, the difference in the phases at which shedding occurs can be determined. This is shown in Figure 3.7. Increases in the forcing amplitude cause the shedding to be delayed to a later phase. Between the highest and lowest forcing amplitude, the phase difference is approximately ½ of the forcing cycle. This dependence of amplitude on the phase at which vorticity is shed highlights the non-linear nature of the process by which the vorticity align into a vortex street.

For the 6 Hz forcing frequency, the spatial periodicity does not effect the measurement of the free stream RMS values. As seen in Figure 3.6, on the top and bottom

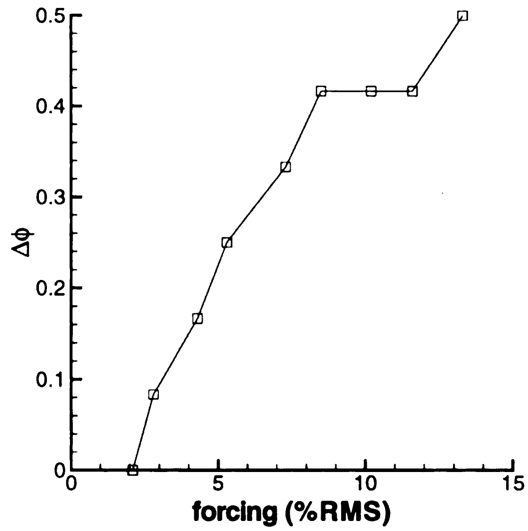

Figure 3.7: Dependence of phase time at which shedding occurs on forcing amplitude.

portions of the test section, a region of uniform u_{rms} can be seen. Figure 3.8 shows a line plot of the u_{rms} profile for several forcing amplitudes. From these data, the value of u_{rms} can be determined and compared with u_0.

Reynolds Stress

Figure 3.9 shows the Reynolds stress in the unforced wake as well as the wake forced with 4 different forcing amplitudes. The grey scale level in the flooded contour plot is used to signify the intensity of the variable being examined. Overlaid on top of the flooded contours are coarsely spaced contour lines to differentiate between the positive and negative signs of the variable. The dashed lines indicate the negatively signed data. This format will be used in many of the successive plots. In the unforced and the 2.1% forcing cases, the value of Reynolds stress is small. However, the higher forcing amplitudes show a spatial periodicity in their value. For the 11.6% and 13.3% forcing cases, the positive and negative

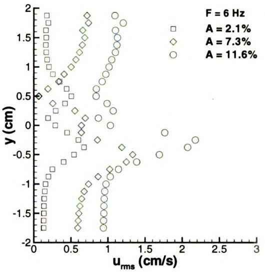

Figure 3.8: Line plot of u_{rms} for three forcing amplitudes.

signs of Reynolds stress are nearly aligned vertically. However, the 7.3% forcing shows an offset in the vertical spacing. This is quite similar to the patterns seen in the vortex spacing that will be shown in Section 3.3.

Mean Vorticity Field

Using the MTV technique, it is also possible to examine other quantities based on the 1st (and higher) spatial derivatives. These quantities, such as vorticity and strain are very useful in determining the nature of the flow field. The accuracy of the vorticity calculation has been discussed in Appendix A.

Figure 3.10 shows the mean vorticity field for an unforced wake and for the wake forced with four different forcing amplitudes. It is interesting to note that magnitude of the mean vorticity field is larger in the unforced case than in the forced case. This is the result of the vortex alignment in the forced cases which causes the positively and negatively signed

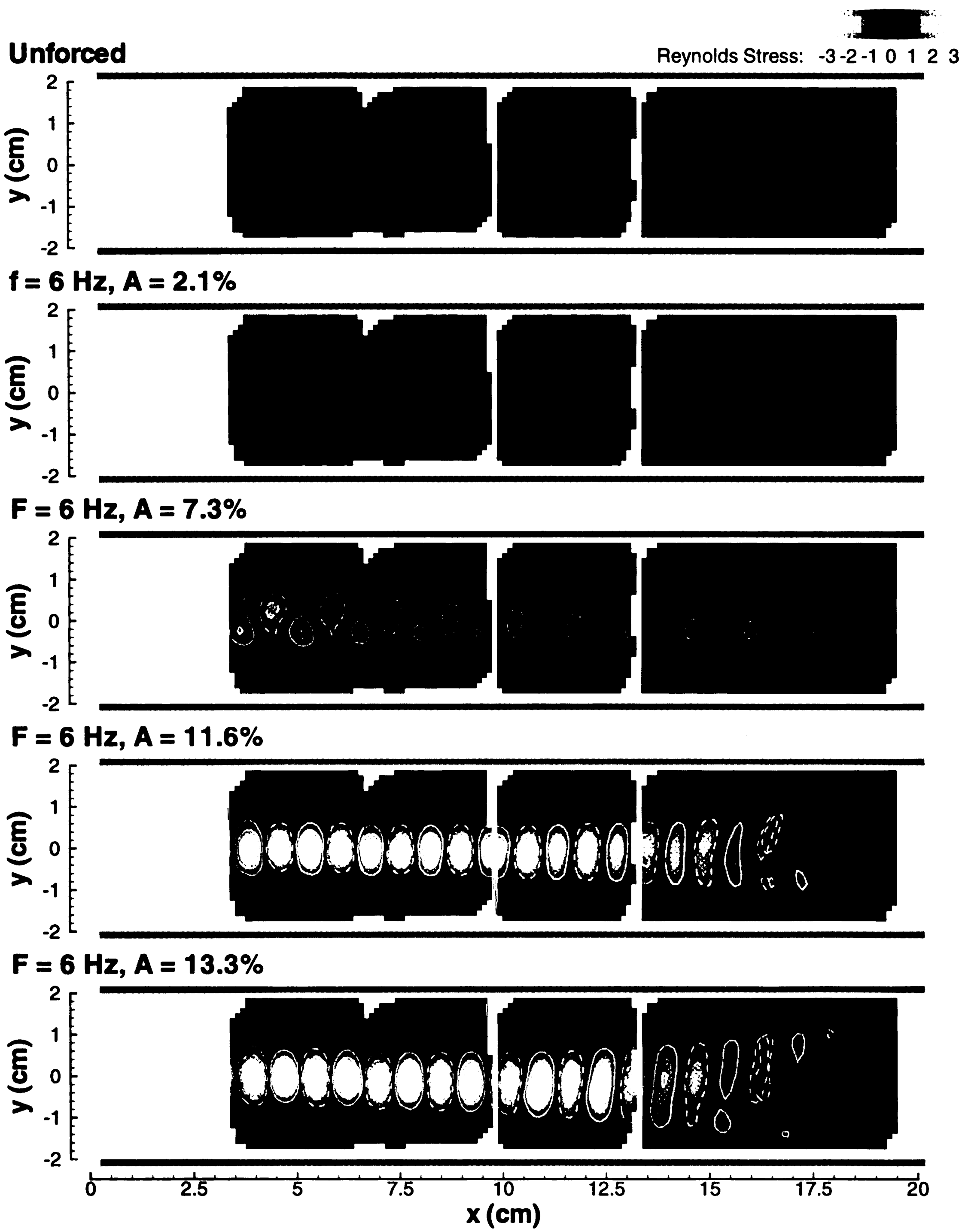

Figure 3.9: Reynolds stress distribution in unforced and forced wake. The contour lines indicate the ±*0.6*, ±*1.2*,...,±*3.0* levels.

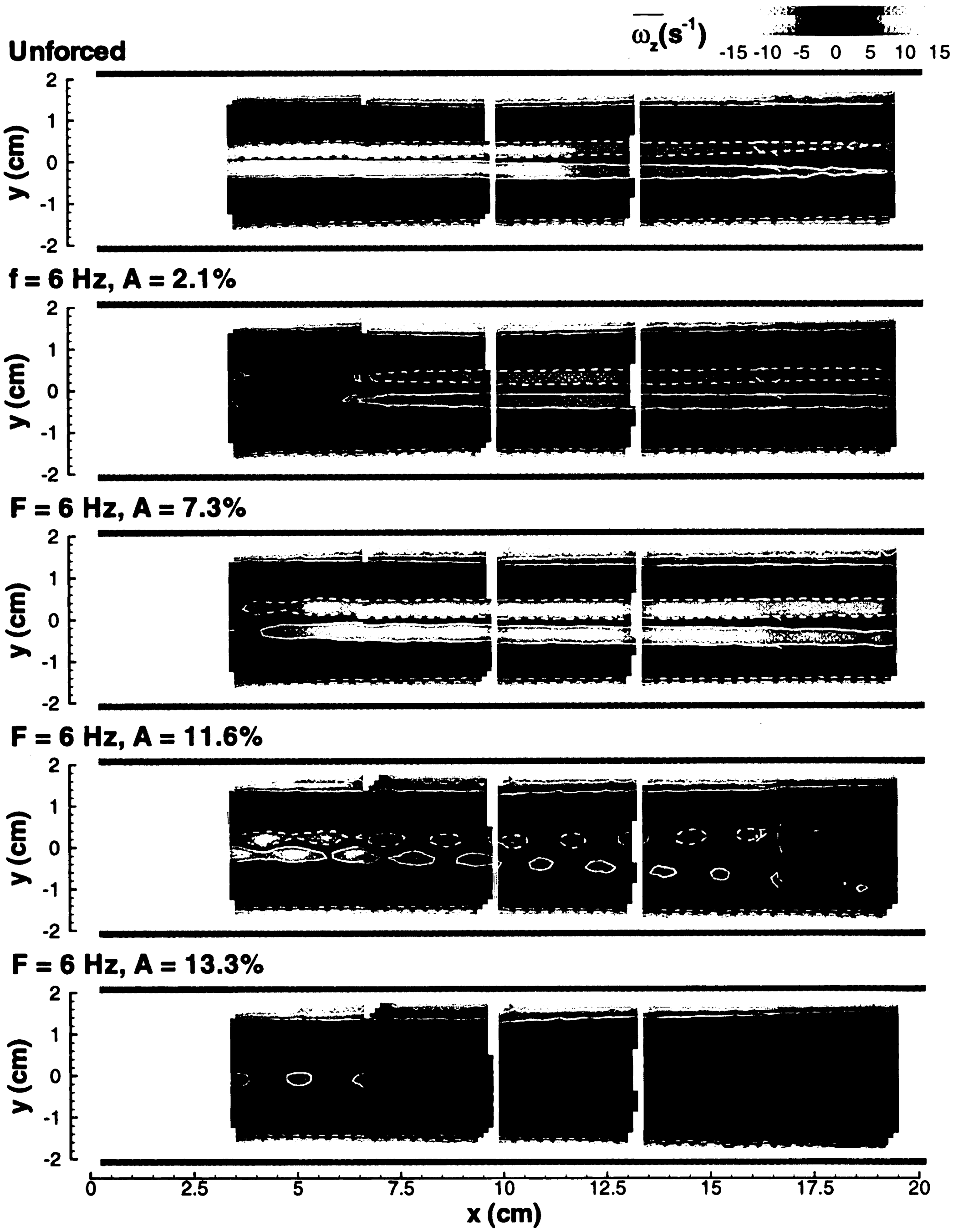

Figure 3.10: Mean vorticity field for unforced wake and wake forced at 6 Hz. Contour lines are spaced at $\pm 3\ s^{-1}$, $\pm 6\ s^{-1}$, ..., $\pm 15\ s^{-1}$. Dashes indicate negative contours.

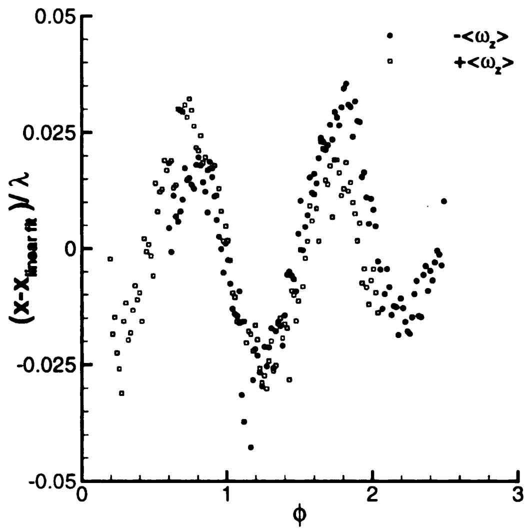

Figure 3.11: Streamwise location of phase-averaged vortex cores versus phase. A linear fit has been subtracted from the locations.

vorticity to cancel out in the mean. The vortex spacing parameter will be discussed in more detail in the following section. Between 2.1% and 7.3% forcing, the mean vorticity increases slightly, however it decreases again before the 11.6% forcing case. In the highest amplitude case (13.3%) the positively and negatively signed vortices are nearly perfectly aligned resulting in near zero mean vorticity throughout the measurement range.

In the 7.3% and 11.6% forcing case, compact regions of $\overline{\omega_z}$ are apparent. These regions are generated because the convection speed of the vortices is not constant. This was determined by plotting the x location of the positively (and negatively signed) vortex cores over several forcing cycles. A linear fit of the x location with respect to phase is then performed. The value of the linear fit is then subtracted from the actual location at each phase. The result of this process is shown in Figure 3.11. Note the oscillatory appearance which indicates that the mean convection speed is not constant. The peak difference amounts to about 2.5% of the mean vortex convection speed. The compact regions of $\overline{\omega_z}$ are also seen in the 13.3% forcing amplitude. However, the near perfect alignment between the positively and negatively signed $\overline{\omega_z}$ tends to reduce the impact of the non-constant convection speed.

Effect of forcing on $\frac{\partial w}{\partial z}$

Using the incompressible continuity equation, it is also possible to derive the spanwise derivative of the cross-stream velocity, that is, $\frac{\partial w}{\partial z}$. This term is important in the vorticity transport equation in the term for the stretching of the spanwise component of vorticity. A negative value indicates that the magnitude of the spanwise vorticity will be decreasing. As seen in Figure 3.12, the mean value of this quantity, $\overline{\frac{\partial w}{\partial z}}$ is very small for the unforced and low amplitude forcing cases. Even though the magnitude is quite small, its effect on ω_z is significant as will be discussed later. However, for the larger forcing amplitudes, negative values of $\overline{\frac{\partial w}{\partial z}}$ can be seen in a wedge shaped region in the center of the facility. On the top and bottom surfaces of the facility, $\overline{\frac{\partial w}{\partial z}}$ is positive. The sign of this quantity is consistent with a mean recirculatory flow in the cross-stream plane, as seen in Figure 3.13, which transports fluid from the sidewalls of the facility towards the center, and then back out towards the sidewalls in the region near the top and bottom walls of the facility. In Chapter 4, the cross-stream plane will be examined and it will be shown that this pattern is seen in this flow field.

It is also interesting to note that the increase in $\overline{\frac{\partial w}{\partial z}}$ corresponds quite closely with the location where the amount of mixing product was found to increase in the studies by MacKinnon, Koochesfahani, and Nelson. Figure 3.14 shows a plot of $\overline{\frac{\partial w}{\partial z}}$ for the 11.6%

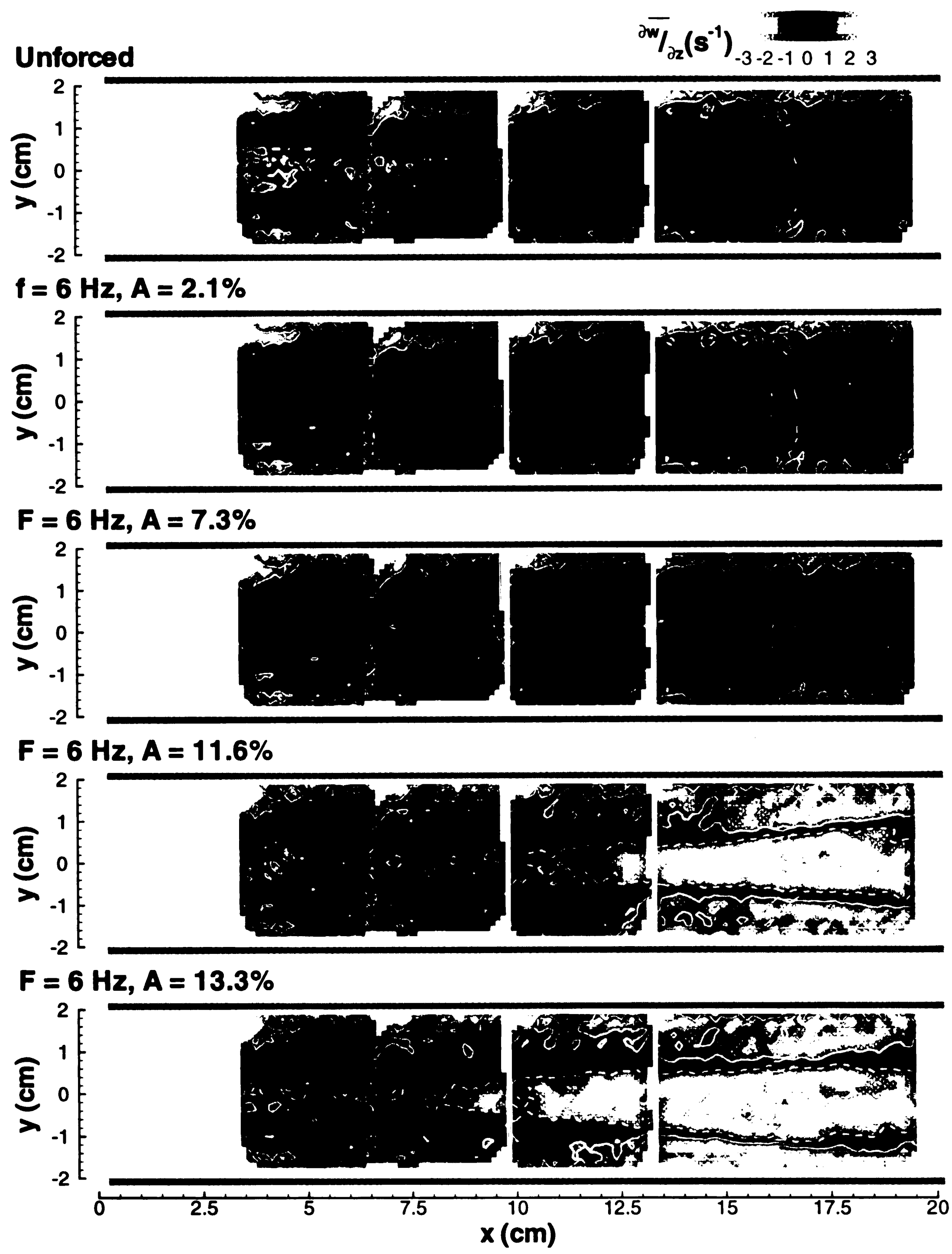

Figure 3.12: Mean $\overline{\frac{\partial w}{\partial z}}$ for the unforced wake and four perturbation amplitudes. The solid and dashed contours separate regions of positive and negative value.

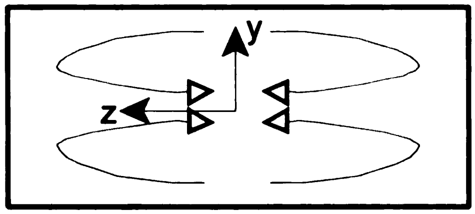

Figure 3.13: Example of recirculatory flow pattern.

forcing case overlaid on top of the $\frac{\delta_p}{\delta_1}$ curve from the high amplitude forcing case Koochesfahani and Nelson, 1997. The increase in $\overline{\frac{\partial w}{\partial z}}$ slightly precedes in streamwise location the increase in $\frac{\delta_p}{\delta_1}$. The value of $\overline{\frac{\partial w}{\partial z}}$ even exhibits a slight decrease just before the $\frac{\delta_p}{\delta_1}$ begins to level out. Note that general presence of $\overline{\frac{\partial w}{\partial z}}$ alone does not generate mixing enhancement. Rather, it is indicative of other characteristics which generate the mixing enhancement.

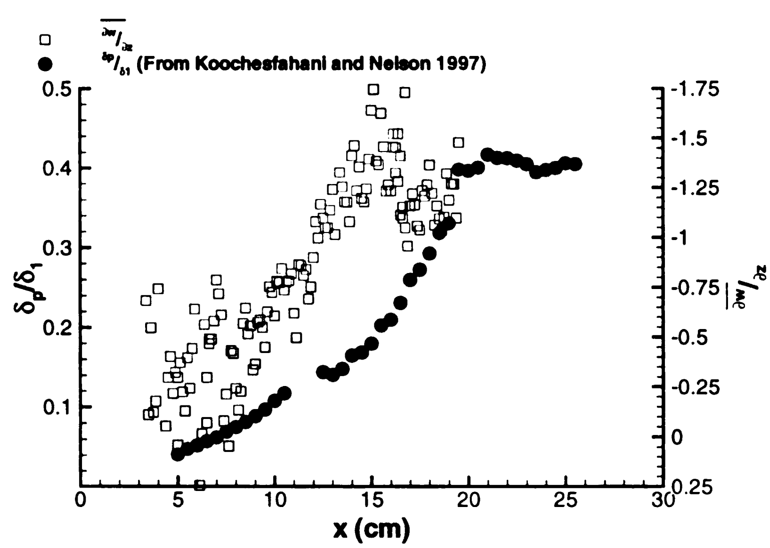

Figure 3.14: Comparison of $\overline{\frac{\partial w}{\partial z}}$ in 11.6% forcing case and $\frac{\delta_p}{\delta_1}$ from Koochesfahani and Nelson, 1997.

3.3 Phase-averaged ("instantaneous") flow properties at center span

At this point, it is useful to examine the properties of the phase-averaged $<\omega_z>$ field. In section 3.1, the phase-averaged field was found to very closely match the instantaneous realization. Figure 3.15 shows an instantaneous ω_z field for the unforced case and a representative phase bin of the $<\omega_z>$ field for 5 forcing cases. In the unforced case, it is difficult to discern organized vortical structures in the far upstream region. Structures begin to become apparent at approximately $z = 6\ cm$. However, the horizontal spacing between the structures is evolving until approximately *10 cm* downstream. By $x = 17\ cm$, the magnitude of vorticity within the spanwise rollers has decreased to a very small magnitude.

When forcing is applied, identifiable vortex core structures are apparent at the earliest downstream location measured. With increasing forcing amplitude, it is apparent that the strength of the vortical structures is increased in upstream locations. However, at locations farther downstream, the peak values of $<\omega_z>$ are lower in the high amplitude forcing cases than they are in the low amplitude forcing cases.

These effects of perturbation amplitude on the peak magnitude of the spanwise vorticity field are shown more clearly in Figure 3.16. Figure 3.16a shows the effect of forcing amplitude on peak vorticity levels for several different downstream locations. At the farthest upstream location, $x = 3.5\ cm$ (shown by the squares), as forcing amplitude increases, the peak vorticity also increase from about $15\ s^{-1}$ to nearly $40\ s^{-1}$. In the range from unforced to about 6% forcing, the rate of increase is relatively small. For forcing amplitudes larger than 6%, the peak vorticity levels increase rather quickly. As the distance from the splitter plate increases, the trend of peak $<\omega_z>$ increasing with forcing amplitude

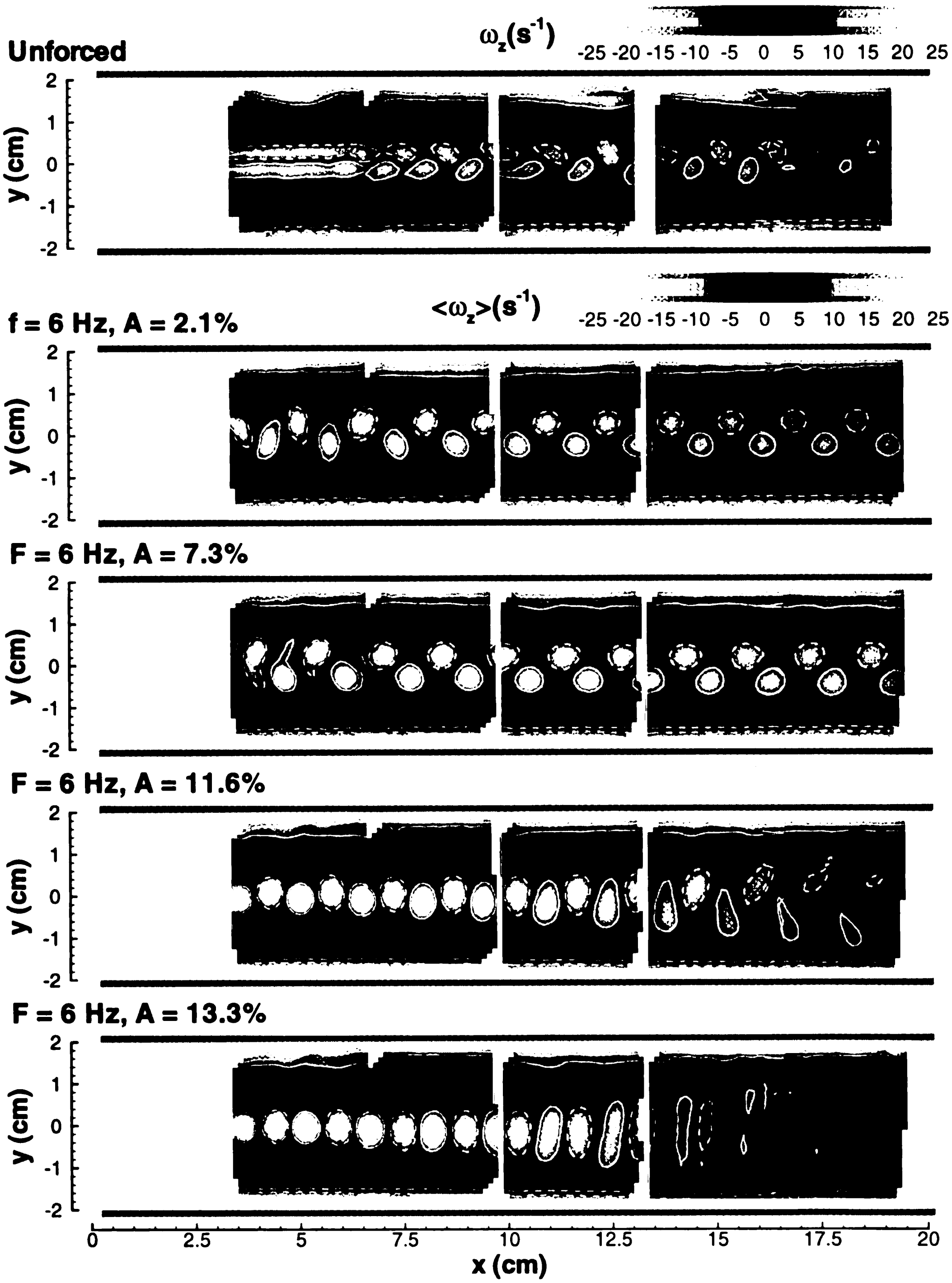

Figure 3.15: Vorticity field in forced and unforced wake. The unforced wake data are instantaneous realizations and the forced wake data are phase-averaged results. Contour lines are spaced at $\pm 5\ s^{-1}$, $\pm 10\ s^{-1}$, ..., $\pm 25\ s^{-1}$. Dashes indicate negative contours.

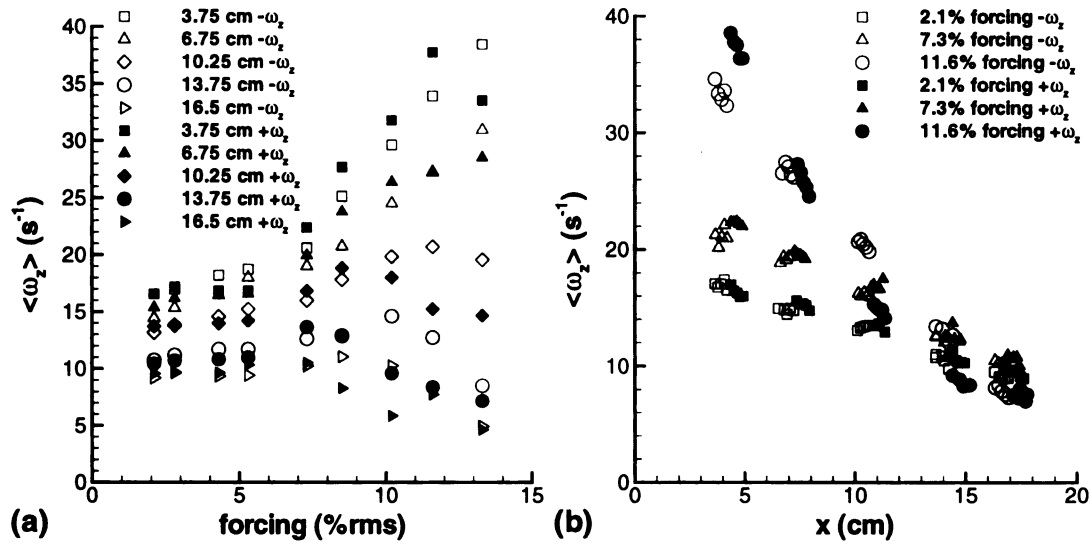

Figure 3.16: Effect of forcing on peak vorticity magnitude. (a) Effect of forcing on vorticity magnitude at several downstream locations. (b) Variation of vorticity magnitude for *3* forcing amplitudes with respect to streamwise location.

changes. At a downstream location of *10.25 cm* (diamonds), there is little change in the magnitude of the peak vorticity with increased forcing. At x = *13.75 cm* (circles) and x = *16.5 cm* (right pointed triangle), the magnitude of the vorticity peak decreases slightly as forcing amplitude is increase.

According to the results presented in Appendix A, the spatial filtering resulting from the spatially under-resolved velocity measurements in the data set will result in the peak vorticity levels being underestimated. The current data set has a L/δ (feature size measured by the vortex core radius to mean data spacing) ratio of approximately *2.5*. This will result in the peak vorticity values being underestimated by about *18%*. However, this does not affect the reported trends. Only the magnitudes of the peaks would be increased by *18%*. This results in an actual peak vorticity level of approximately $47\ s^{-1}$. This will be further examined in section 3.5.

Figure 3.16b shows the peak vorticity value as the vortices convect downstream for three representative forcing amplitudes. It is apparent that the vorticity decreases much faster for the higher amplitude forcing cases than for the other cases. Although the vorticity magnitude of the 11.6% forcing case is initially over double that of the 2.1% forcing case, by *15 cm* downstream, the magnitude of the vorticity for the higher amplitude forcing is less than that of the lower amplitude forcing.

One might think that the decrease in $<\omega_z>$ is due to viscous diffusion. However, it will be shown that the rate of decay of $<\omega_z>$ due to diffusion is much too slow to describe the decrease. Rather, the decay in the peak vorticity level is best described by negative vortex stretching, which is connected to $\frac{\partial w}{\partial z}$. The vorticity transport equation will be used to assess the drop in the peak value of $<\omega_z>$ from viscous diffusion as well as stretching. The vorticity transport equation which describes the change in phase-averaged spanwise vorticity is

$$\frac{D<\omega_z>}{Dt} = (\omega_x \frac{\partial w}{\partial x} + \omega_y \frac{\partial w}{\partial y} + \omega_z \frac{\partial w}{\partial z}) + \nu \frac{\partial^2}{\partial z^2} <\omega_z>.$$

Recall that it has been previously shown that the $<\omega_z>$ is an excellent representation of ω_z and is used in place of the instantaneous value. Assuming constant vortex convection speed, and assuming that at least initially, $<\omega_x>$ and $<\omega_y>$ are small, the above equation takes the following form.

$$\frac{\partial <\omega_z>}{\partial x} = \frac{1}{u_0}(<\omega_z> \frac{\partial w}{\partial z} + \nu \frac{\partial^2}{\partial z^2} <\omega_z>).$$

Note that the two terms describing vorticity reorientation have been eliminated and the only remaining terms are related to diffusion and stretching. Further note that the free stream velocity u_0 is used for the vortex convection speed. The vortex convection speed is actually slightly smaller than the free stream velocity.

Figure 3.17 compares the decay of the peak vorticity observed in the 2.1% and 11.6% forcing cases with the decay that would be observed due solely to stretching and solely to diffusion. For both the stretching and the diffusion results, the vortex strength and core radius at the initial location is used as a boundary condition. For computing the stretching results for both forcing amplitudes, $\frac{\partial w}{\partial z}$ is set to a constant value. For the 2.1% forcing case, $\frac{\partial w}{\partial z} = -0.35\ s^{-1}$ and for the 11.6% forcing case $\frac{\partial w}{\partial z} = -1\ s^{-1}$. These values are reasonable estimates of the actual value of $\frac{\partial w}{\partial z}$ found in the two forcing cases. However, these small values are near the detection threshold of the current experiments. The value of $\frac{\partial w}{\partial z}$ also tends to increase with the downstream development of the structures. This was not modeled.

The decay of the peak vorticity for the low amplitude forcing case is shown in Figure 3.17a. Within the measurement range, the measured peak $\langle\omega_z\rangle$ decays approximately *45%*. However, the decay estimated solely to diffusion (solid line) is only approximately *5%*. The estimated decay of peak vorticity caused by the small amount of vortex stretching agrees quite well with the decay seen in the actual results. This agreement is much more apparent in the 11.6% forcing case examined in Figure 3.15b. The dashed line indicating the decay due solely to the stretching parameter agrees quite well with the actual decay whereas the solid line indicating the decay due to diffusion does not yield the decay seen in the actual experiments. It is of course recognized that the actual decay of the peak vorticity is caused by the combination of the two effects. However, the stretching term dominates in this flow.

Although the peak vorticity magnitude is decreasing rather quickly in the high

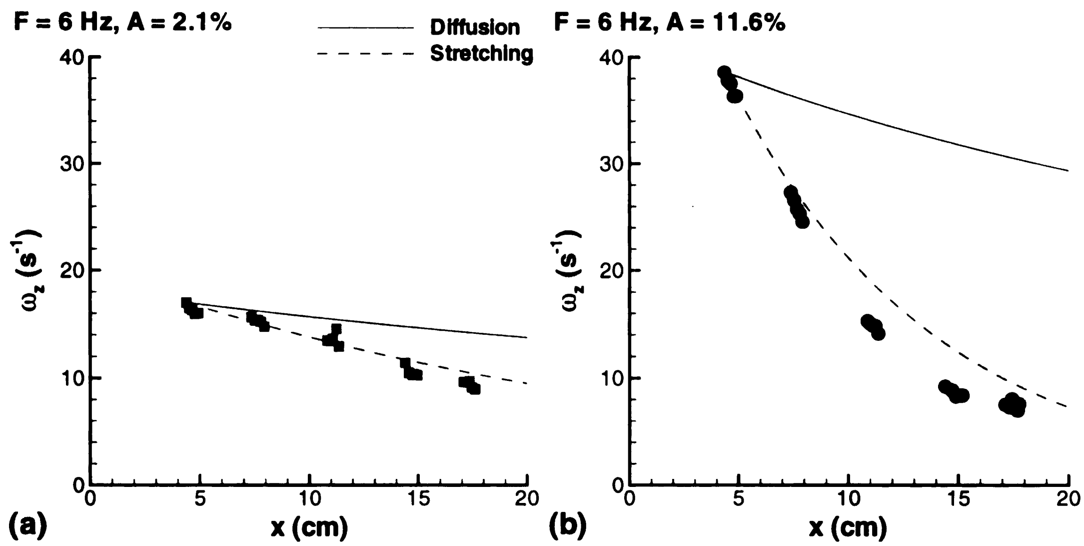

Figure 3.17: Comparison of the decay of the peak spanwise vorticity with the decay due to solely stretching and solely diffusion. (a) 2.1% forcing amplitude. (b) 11.6% forcing amplitude.

amplitude forcing cases, the circulation of the cores in this case decreases at a much slower rate. Figure 3.18a shows the effect of increasing the forcing amplitude on the circulation, Γ_z. Circulation is computed by integrating the $<\omega_z>$ above the $+1\ s^{-1}$ for the positively signed core and below the $-1\ s^{-1}$ for the negatively signed core threshold in the region within $\pm 0.5\lambda$ of the center of the core. For all downstream locations, increased forcing results in an increase in the circulation. This is in contrast to the peak vorticity plot of Figure 3.16a in which the peak vorticity decreased with forcing amplitude at $x > 10\ cm$ for forcing amplitudes greater than 10%. Figure 3.18b shows the variation of the circulation in the vortex cores for three of the forcing amplitudes. In the high amplitude forcing, the circulation decreases by approximately a factor of two over the range being examined, compared to the factor of nearly four seen in the peak vorticity. In the low amplitude cases, the circulation decreases by 25%, however, this is still a smaller decrease than is seen in the peak vorticity for this forcing amplitude. This smaller level of decrease is likely a result of

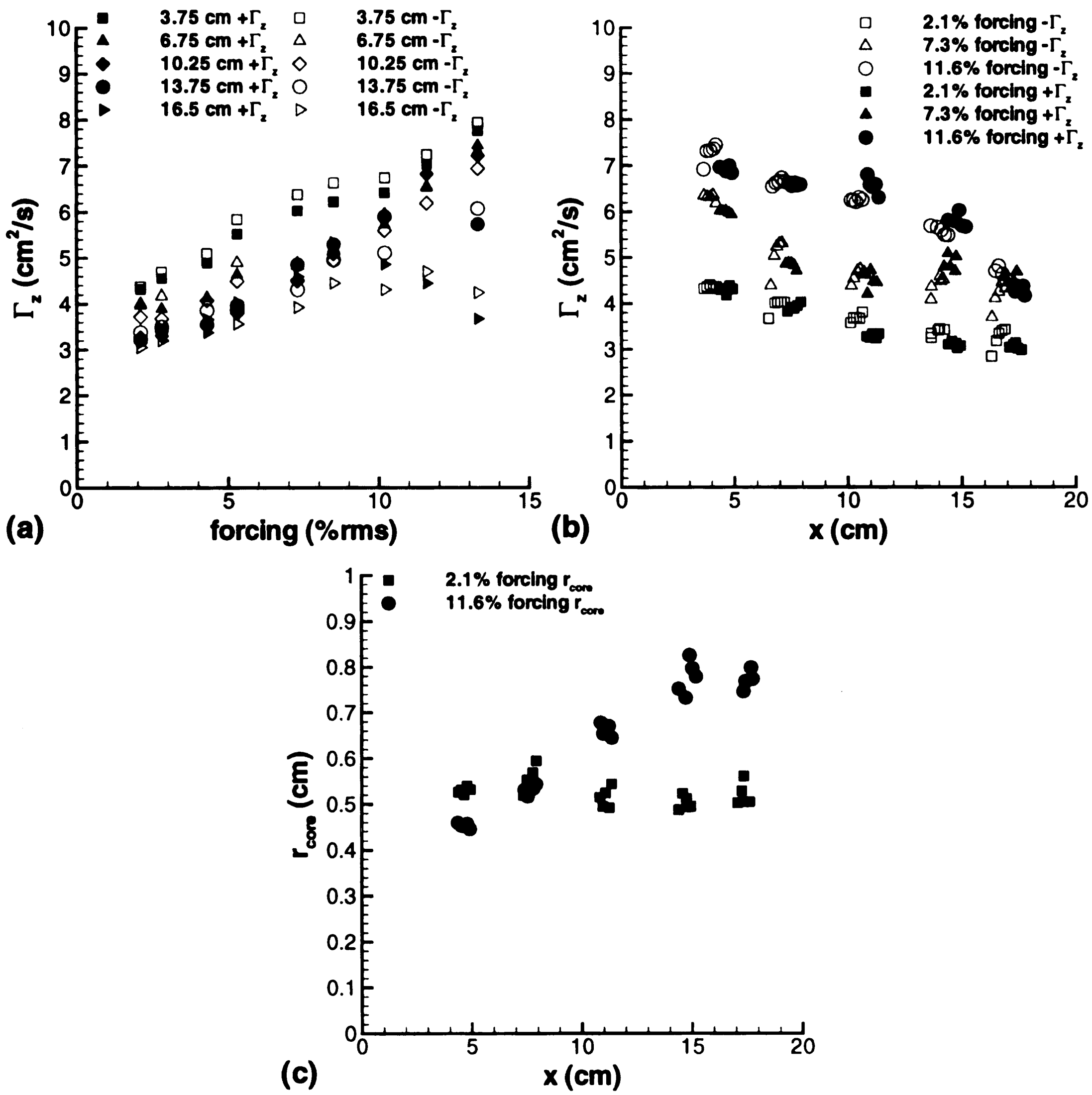

Figure 3.18: Vortex core circulation. (a) Effect of forcing on circulation at several different downstream locations. (b) Effect of downstream location for several forcing amplitudes. (c) Effect of downstream location on vortex core radius.

the core radius increasing due to the stretching term.

As the vortex cores convect downstream, the effect of stretching causes the originally Gaussian shaped vorticity profiles to flatten out and to stretch in the vertical direction. This makes it difficult to determine the core radius in terms of the location at which vorticity drops to the e^{-1} point. In order to determine an effective radius for the vortex cores, a "radius of gyration" is computed. The radius of gyration is defined as the square root of the second polar moment of inertia of vorticity divided by the circulation. That is,

$$r_{core} = \sqrt{\frac{\iint r^2 \omega dA}{\iint \omega dA}}$$

When the Gaussian vorticity profile is used with this formulation, that is $\frac{\omega}{\omega_{max}} = e^{-(\frac{r}{r_{core}})^2}$, the expected value core radius is recovered. Figure 3.18c shows the vortex core radius for two different forcing amplitudes. Note that in the 2.1% forcing condition (squares), the core radius remains nearly fixed at a value of *0.5 cm*. For the 11.6% forcing case, the core radius nearly doubles between $x = 5$ *cm* and $x = 18$ *cm*, increasing from *0.45 cm* to *0.8 cm*. This results in a threefold increase in the area of the core. Thus, the decrease in vorticity magnitude is tempered by the increase in core radius.

Figure 3.19a defines the vortex spacing parameters *a* and *b*. Re-examining Figure 3.15 and looking at the locations of the vortices, qualitatively, it can be seen that the horizontal spacing between vortices, *a*, remains fixed for all of the forcing cases. This is indicative of the nearly fixed vortex convection speed and the constant forcing frequency. The vertical spacing, *b*, appears to remain approximately constant between the 2.1% and

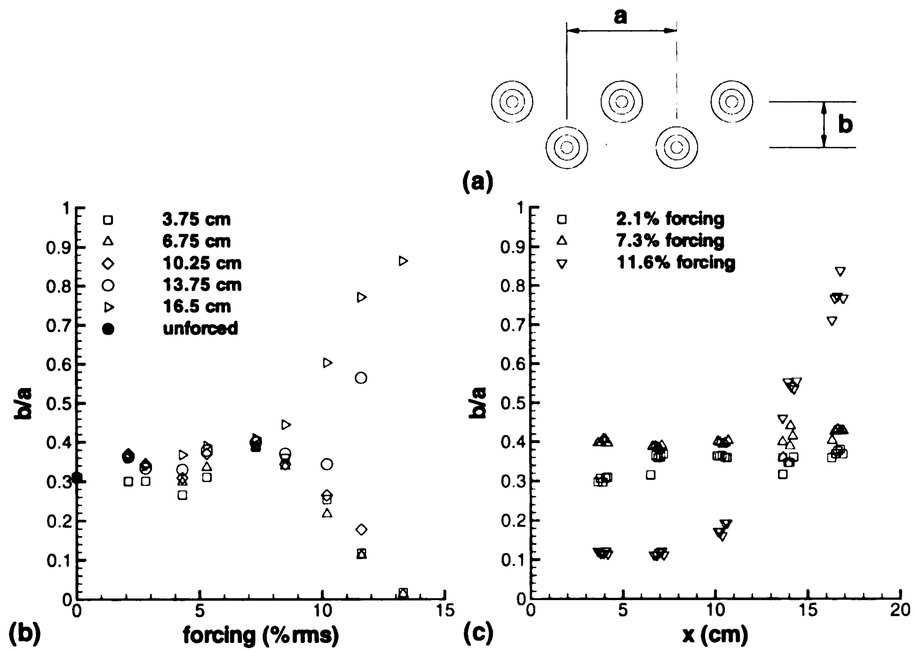

Figure 3.19: Effect of forcing on vortex spacing parameters. (a) Definition of spacing parameters. (b) Effect of forcing on spacing ratio at several different downstream locations. (c) Effect of downstream location on spacing ratio for three forcing amplitudes.

7.3% forcing cases. Then, it decreases until the vortices are nearly aligned in the 13.3% case. Figure 3.19b plots the ratio of *b* to *a*, as determined from the locations of the peak $\langle\omega_z\rangle$ and shows the effect of forcing on vortex spacing more quantitatively. The spacing parameters are measured from the location of peak vorticity within each core. For the unforced case, *b/a* = *0.31*. This value is slightly larger than the theoretical Karman spacing ratio of *0.281*. The measured value of the unforced value of *b/a* in this study is significantly different from that found in the work of Roberts (1985), where the unforced *b/a* = *0.52*. It should be noted, however, that the Roberts study measured the vortex spacing by visually locating the center of the vortex cores. Using a data set in which flow visualization and velocity/vorticity measurements were acquired simultaneously, it was found that the value of *b/a* estimated by visual methods tends to be larger than that measured by locating the center of vorticity. However, the visual estimation is highly dependent upon the individual making the measurement.

At $x = 3.75\ cm$ (squares), b/a remains relatively constant, possibly increasing slightly for forcing levels less than about 7.5%. The value is slightly larger than that of the unforced case. For larger forcing levels, the spacing ratio decreases and at 13.3% forcing, the value is nearly zero. It is believed that if the forcing amplitude is further increased, this ratio would become negative, which could indicate a thrusting type condition. However, this was not examined in this work. At locations farther downstream, such as $x = 16.5$ cm, the trend is reversed and, except for the 13.3% forcing condition, the vertical spacing increases with increasing forcing amplitude. In the 13.3% forcing case, the spacing remains nearly constant. This is likely due to the initial alignment in this case in which the positive and negative signed vortices are at the same vertical location.

Figure 3.19c shows the effect of downstream location on the spacing ratio for the several forcing cases. For the two low amplitude forcing cases, the spacing ratio remains nearly constant between *0.3* and *0.4*. However, for the 11.6% forcing case, the spacing ratio is initially a very low value, *0.1*. In the range greater than *10 cm* downstream, the spacing ratio increases dramatically to a value of *0.9*. By this downstream location however, $\langle\omega_z\rangle$ is very stretched out and no longer has a Gaussian character. In the region $x > 10$ cm it has also corresponds to the range of locations where $\frac{\partial w}{\partial z}$ values increased and where Koochesfahani and Nelson (1997) found large increases in mixing product.

The effect of variation of the forcing frequency on b/a presented in Roberts (1985) is quite different from what is seen in this study when the forcing amplitude is varied. At low forcing frequencies, Roberts found that b/a is approximately *0.52*. As the forcing frequency is increased to about twice the natural shedding frequency, *b/a* decreases to its minimum value which is slightly less than theoretical Karman spacing ratio of *0.281*. As previously mentioned, it was at this frequency where Roberts saw the largest increase in the amount of mixed fluid. At higher forcing frequencies, the spacing increased again. Plotting these spacing results versus forcing frequency would result in a u-shaped curve with a minimum located where the forcing frequency is twice the twice the natural frequency. It is interesting to note that the high mixing levels found by MacKinnon and Koochesfahani (1997) and Koochesfahani and Nelson (1997) are also for cases where the forced wake generates a small vertical spacing between vortices in the upstream locations. However, it will be shown in Chapter 5 that decreased *b/a* is most likely not an indicator of a forcing condition which will contain significant mixing enhancement.

In the current work, it has been shown that the *b/a* is influenced by the forcing amplitude as well as the downstream location at which the measurements have been made. Neither of these two characteristics were examined in Roberts (1985). The flow is going to respond differently to input perturbations at different forcing frequency. Thus, measurements need to be made to determine whether the forcing levels can indeed be compared. As the forcing frequency changes, each downstream location is a different number of forcing wavelengths downstream. Thus, at the same downstream location the vortex array may be at a different point in its evolution. Both of these effects will generate changes in the spacing which may alter the u-shaped spacing curve found by Roberts.

3.4 Flow properties away from the center span

As the spanwise vortex cores encounters the sidewalls of the test section, the boundary layers on the sides of the test section are going to affect the core. Very few studies have examined these types of flows close to sidewalls. Nelson (1996) examined mixing results at the center span location as well as two locations closer to the sidewalls of the facility. As previously mentioned, this study was conducted in the same experimental facility used in the present work. At the first off center span location, $z = -0.8\ cm$, the results of both the flow visualization and mixing levels show effects very similar to those seen at the center span. However, it appears that the spanwise vortex rollers become three-dimensional at a location farther upstream than at the center span.

At the second off center span measurement plane, $z = -2\ cm$ (halfway between the centerline and the wall), the mixing and flow visualization results were markedly different from those at the center span. In the highest amplitude forcing case, three-dimensional motion was found very far upstream. Furthermore, the vortex pattern changed dramatically as it convected downstream. It was also found that the flow is well mixed at a significantly earlier downstream location than at center span. At $x = 11\ cm$, both the visual thickness, δ_l and the product thickness, δ_p reach their maxima. Farther downstream, δ_l remains constant, while δ_p actually decreases.

Figures 3.20, 3.21, and 3.22 show the vorticity field of the 11.6%, 7.3% and 2.1% forcing cases for a common range of downstream locations at seven different spanwise locations in the flow. All plots are for a common phase which was selected such that a negatively signed vortex core is located at a common location in the $z = 0\ cm$ spanwise

Fig

stre

s^{-1}

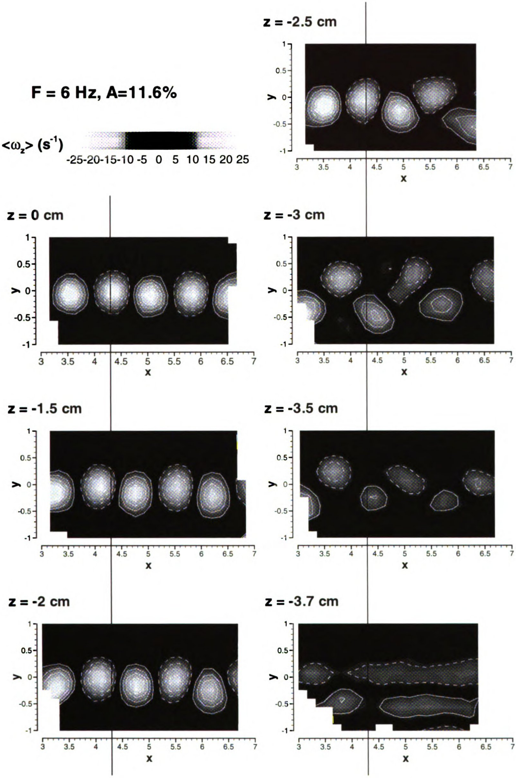

Figure 3.20: Flooded contour plots of spanwise vorticity in wake forced at 11.6% of free-stream velocity for *7* different spanwise locations. Contour lines are spaced at $\pm 5\ s^{-1}$, $\pm 10\ s^{-1}$, ..., $\pm 25\ s^{-1}$. Dashes indicate negative contours.

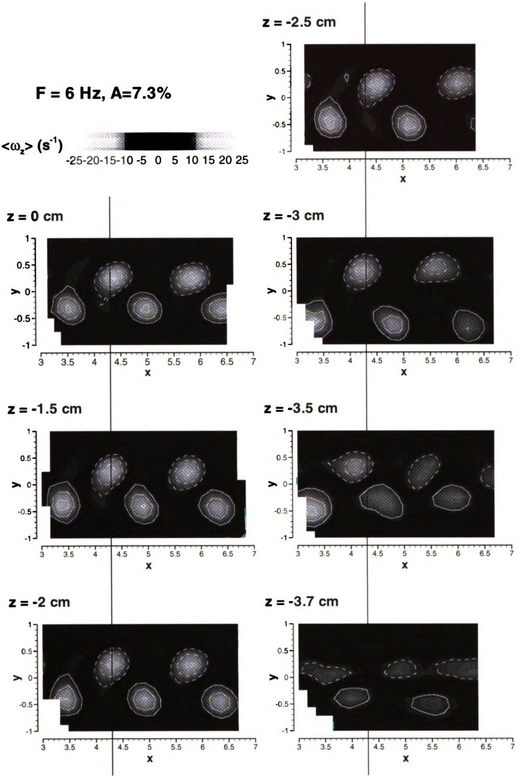

Figure 3.21: Flooded contour plots of spanwise vorticity in wake forced at 7.3% of free-stream velocity for *7* different spanwise locations. Contour lines are spaced at $\pm 5\ s^{-1}$, $\pm 10\ s^{-1}$, ..., $\pm 25\ s^{-1}$. Dashes indicate negative contours.

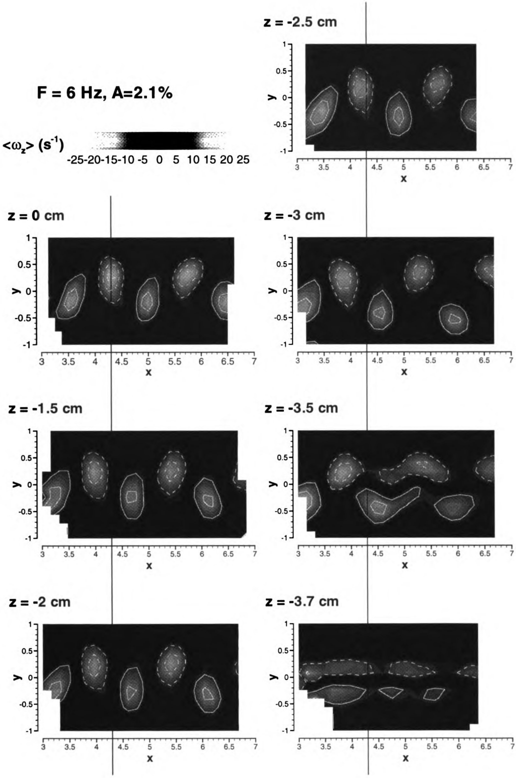

Figure 3.22: Flooded contour plots of spanwise vorticity in wake forced at 2.1% of free-stream velocity for *7* different spanwise locations. Contour lines are spaced at $\pm 5\ s^{-1}$, $\pm 10\ s^{-1}$, ..., $\pm 25\ s^{-1}$. Dashes indicate negative contours.

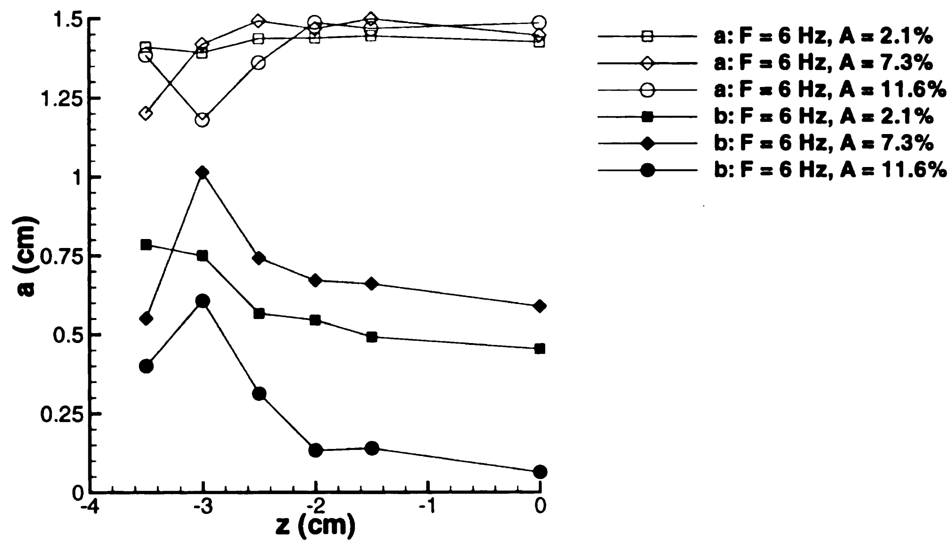

Figure 3.23: Variation of streamwise (a) and transverse (b) vortex spacing with spanwise location.

location for all three forcing amplitudes. A line has been drawn at $x = 4.3\ cm$ to allow for a comparison of the spatial location of the vortices. With the exception of the $z = -2.5\ cm$ measurement which will be described in more detail later in this section, as the measurement plane moves closer to the sidewalls, the location of the vortex core generally moves upstream. This indicates slowing of the core due to the boundary layer on the sidewall of the facility. Note that the effect is the same for the all three forcing amplitudes.

The slowing of the vortex cores can be examined quantitatively be examining the spacing between the cores. Figure 3.23 shows the variation of both the *b* and *a* parameters with spanwise location. Since the forcing frequency is fixed, a decrease in the streamwise separation between the cores indicates a decrease in the vortex convection speed. For the $A = 11.6\%$ case, between $z = 0\ cm$ and $z = -3\ cm$, a decreases from *1.49 to 1.20.* This indicates a *20%* decrease in the convection speed of the spanwise vortex rollers. A similar effect is noted in the two lower forcing amplitudes with a reduced magnitude. It is noted that

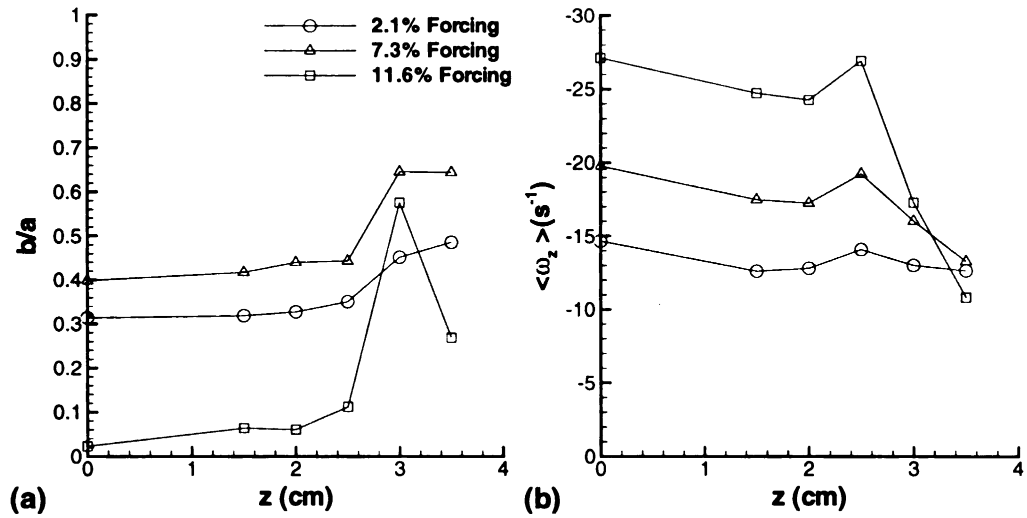

Figure 3.24: Effect of spanwise location on peak vorticity and spacing ratio at x = *4.5 cm.* (a) spacing ratio. (b) peak vorticity.

in the high amplitude forcing case, the value of a is seen to increase again at z = *-3.5 cm.* This effect is not seen in the two lower forcing amplitudes. The transverse spacing parameter, b, also shows a variation with spanwise location. In the central region of the test section, the value remains relatively constant. However, for z < *-2 cm*, b increases for the 11.6% forcing case. For the two lower forcing amplitudes, the increase in b is delayed by *0.5 cm.*

Figure 3.24a shows this variation of b/a for three forcing cases shown above. A slight increasing trend is seen in b/a for z > *-2.5 cm.* This is caused by the slight increase in b previously seen to exist in this region. At z = *-3 cm*, the value of b/a increases very rapidly in the A = 11.6% forcing case. The two lower forcing amplitudes do not exhibit this feature. At z = *-3.5 cm*, b/a decreases again in the 11.6% forcing case, however, it continues to increase in the results for the other two amplitudes. It will be shown in Chapter 4 that in the 11.6% forcing case, z = -3 cm is approximately the spanwise location where the spanwise vorticity is reoriented into the streamwise direction. However, for the lower amplitude cases, the location where the reorientation occurs is closer to the sidewalls. It is believed that a peak in *b/a* exists for these forcing amplitudes, but at a location closer to the sidewalls than could be measured.

Figure 3.24b shows the spanwise variation of the peak $<\omega_z>$ at $x = 4.5\ cm$ for the three forcing amplitudes shown in Figures 3.20-22. In the high amplitude forcing case, the peak vorticity value initially remains relatively constant as the measurement plane moves closer to the wall. From the center of the test section to $z = -2.5\ cm$, the peak vorticity level increases slightly. For $z < -2.5\ cm$, the peak vorticity levels begins a dramatic decrease. This decrease in vorticity magnitude is the result of the bending of the spanwise vortex roller. As the roller bends, the vorticity is reoriented from ω_z into ω_x. A similar effect is noted in the 7.3% forcing case, however, the increase in peak ω_x at $z = -2.5\ cm$ and the subsequent decrease at larger absolute values of z is not as substantial as that seen in the higher forcing amplitude. For the 2.1% forcing case, the peak vorticity remains nearly constant over the entire span.

In the previous discussion on peak vorticity levels, it was noted that at $z = -2.5\ cm$, ω_z is being reoriented into ω_x for the 11.6% forcing case. Further, when the locations of the spanwise vortex rollers was discussed, it was noted that as the measurement plane moved closer to the wall, the location of the spanwise vortex roller generally appears to have moved upstream. However, at this same $z = -2.5\ cm$ spanwise location where the vorticity experienced a dramatic decrease, the roller had moved downstream. At $z = -3\ cm$, the roller has moved downstream again. In order for the core to display these characteristics, it must

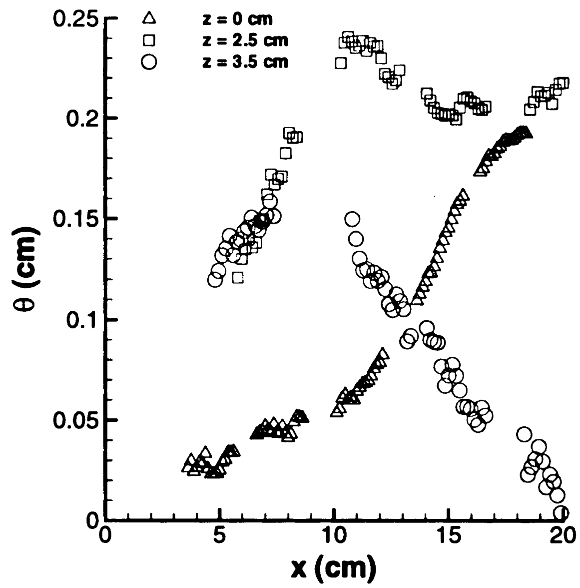

Figure 3.25: Momentum thickness of the forced wake (11.6% forcing amplitude) for the center span and two off-center span locations.

be experiencing a large amount of bending. This bending will result in the reorientation of a significant amount of ω_z into ω_x.

It is noted that it a second possibility for this arrangement is that the core closest to the line drawn at $x = 4.3$ *cm* is not a part of the same core as those seen in the locations closer to center span. That is, the core centered near $x = 4.3$ *cm* is part of the same vortex tube as the vortex seen at $x = 5.75$ *cm* at center span. This seems unlikely as it would require a very large gradient in the mean velocity of the vortex core This would likely have been seen in the plots of the spacing parameters seen in Figures 3.23 and 3.24.

Figure 3.25 shows the variation of the momentum thickness with downstream distance for the 11.6% forcing case at center-span and at two additional spanwise locations. As has been previously seen in Figure 3.4, the momentum thickness for the 11.6% forcing case increased with downstream location. Figure 3.21 shows the streamwise development of θ for the center span and two off center span locations. For both the $z = -2.5$ *cm* and $z =$

-3.5 cm spanwise locations, θ is initially nearly *0.1 cm*. This is the momentum thickness of the unforced wake at the center span. In contrast, at center span the value of θ for the A = *11.6%* forced wake is very close to zero. As the flow moves downstream, the momentum thickness increases for the spanwise location z = *-2.5 cm*. This increase is not as large as that seen at z = *0 cm*. For z = *-3.5 cm*, the trend is decreasing. In section 3.2, is was noted that the span-averaged momentum thickness, in addition to changes in the pressure field are related to the drag on the splitter plate, which must remain constant at all downstream locations. In order to determine if the span-averaged θ is constant, it would be necessary to integrate θ across the entire span. However, not enough measurement locations exist in the current set of experiments to accurately perform this integration. From these three locations, however, it does not seem likely the span-average of θ will be constant. Rather, it is likely that span-averaged θ will increase with downstream location, which would indicate increasing drag. Thus, a decrease in the mean pressure terms must account for this increase.

3.5 Higher Density Measurements

Measurements were made at twice the standard density in order to assess the effect of spatial filtering due to spatial under-resolution in the data. Only the 11.6% case was measured with the higher resolution. Figure 3.26 shows a comparison of the low density and high density measurements for the far upstream location at three different spanwise locations. In all three cases, the spacing between vortices and the general structure of the flow remain the same. However, the vorticity magnitudes are larger in the higher density measurements and there are several features that are more easily distinguishable in the higher density

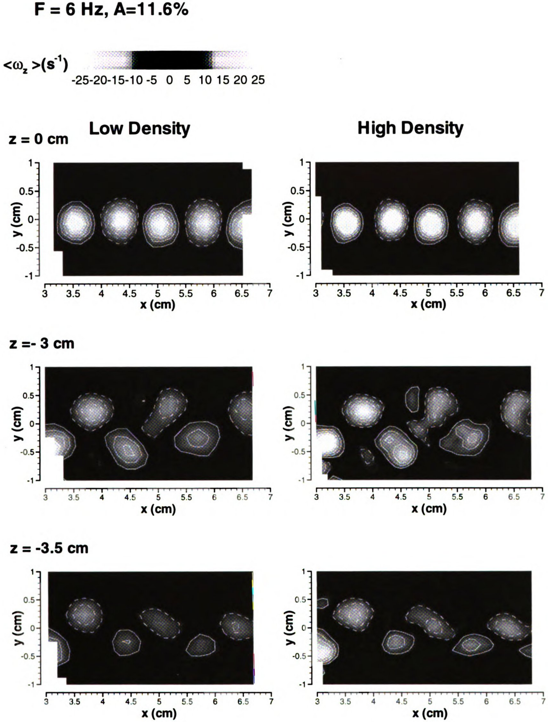

Figure 3.26: Comparison of high density and standard density measurements at three different spanwise locations. Contour lines are spaced at $\pm 5\ s^{-1}$, $\pm 10\ s^{-1}$, ..., $\pm 25\ s^{-1}$. Dashes indicate negative contours.

results.

Examining the center span ($z = 0\ cm$) results, it can be seen that the vorticity magnitudes are increased in the high density measurements as expected. The peak magnitude of the vortex core located at $x = 3.5\ cm$ is slightly more than $35\ s^{-1}$ in the low density results where $L/\delta = 2$. This is increased to nearly $46\ s^{-1}$ in the higher measurement density results where $L/\delta = 4$. Even with this large increase in vorticity magnitude, the structure of the vortex array and the locations of the peak magnitudes of the results of the two different densities looks very similar. Similarly, the high and normal density results at $z = -3.5\ cm$ are very similar. The higher density results have larger vorticity magnitudes and structures appear slightly more elongated in the streamwise direction.

This increase in vorticity magnitude is slightly larger than would be predicted by the results presented in Appendix A on the effect of grid spacing on the peak vorticity magnitude. An examination of the location of the measurement grid reveals that in this measurement set, the center of the vortex core is between two grid points in the low density data and very close to a grid point in the high density data. This effect was not examined in Appendix A, however, it is believed that it will result in the vorticity levels being further underestimated. Using the estimated error values for the 2nd order finite difference method and the high density data presented in Appendix A and the approximate number of vectors per core radius, it is estimated that the actual peak vorticity should be $47\ s^{-1}$.

Comparing the high and standard density results at the $z = -3\ cm$ spanwise location, in the high density results, it appears as if the vortex cores at this location have undergone some type of splitting process. Looking at the large positive and negative cores located at $(x, y) = (4.5, -0.5)$ and $(x, y) = (5, 0.4)$, respectively, it appears as if regions of vorticity are splitting away from the primary core. The magnitude of the peak vorticity in the secondary vortex is approximately $^1/_3$ of the peak vorticity in the primary vortex core from which it splits. Although this effect is present in the standard measurement density data, it is much more difficult to distinguish. An examination of an animation of the data further reveal that the small positively signed core located at *(4.75, 0.5)* has split off from the positive core that is located *(4.5, -0.5)*. It has convected into the upper stream as a result of the induced velocity of the negatively signed core at *(5, 0.4)*. Similarly, the negatively signed vorticity breaking off from the core located at *(5, 0.4)* will eventually move into the bottom stream. The splitting process in this flow seems similar to that found in the study of a wall jet by Visbal, Gaitonde, and Gogineni (1998).

Chapter 4

Cross-stream Measurements

4.1 Effect of out-of-plane motion on in-plane velocity measurements

In optical based velocimetry methods which track the motion of a tracer, whether it be particles or some other features, such as a phosphorescent laser grid, within a flow, out-of-plane motion can cause an apparent in-plane motion to be seen in velocity field measurements as seen in figure 4.1a. This is an issue in all flows, however, in flows where the out-of-plane component of the velocity field is of the same order, or larger than the in-plane velocities, the error generated in the velocity field measurements can be considerable and proper experimental design is very important in order to minimize its effect. The (v, w) velocity measurements discussed in this chapter require that the detector is placed parallel to the (y, z) plane such that the free-stream velocity is moving directly towards the detector. In fact, the out-of-plane velocities in this measurement plane are nearly twice that of the in-plane velocities.

The general mechanism causing this in-plane motion caused by the out-of-plane displacement is shown in Figure 4.1b. An object in the image plane (e.g. a particle, an MTV grid crossing, or some other tracer) initially located at point **A** is imaged onto point **B** on the detector array. The out-of-plane motion in the flowfield causes the tracer to move a distance Δz towards the camera to a location **A**$'$. Assuming that the tracer remains in the depth of field of the imaging system, this new point will be imaged at a location **B**$'$ on the

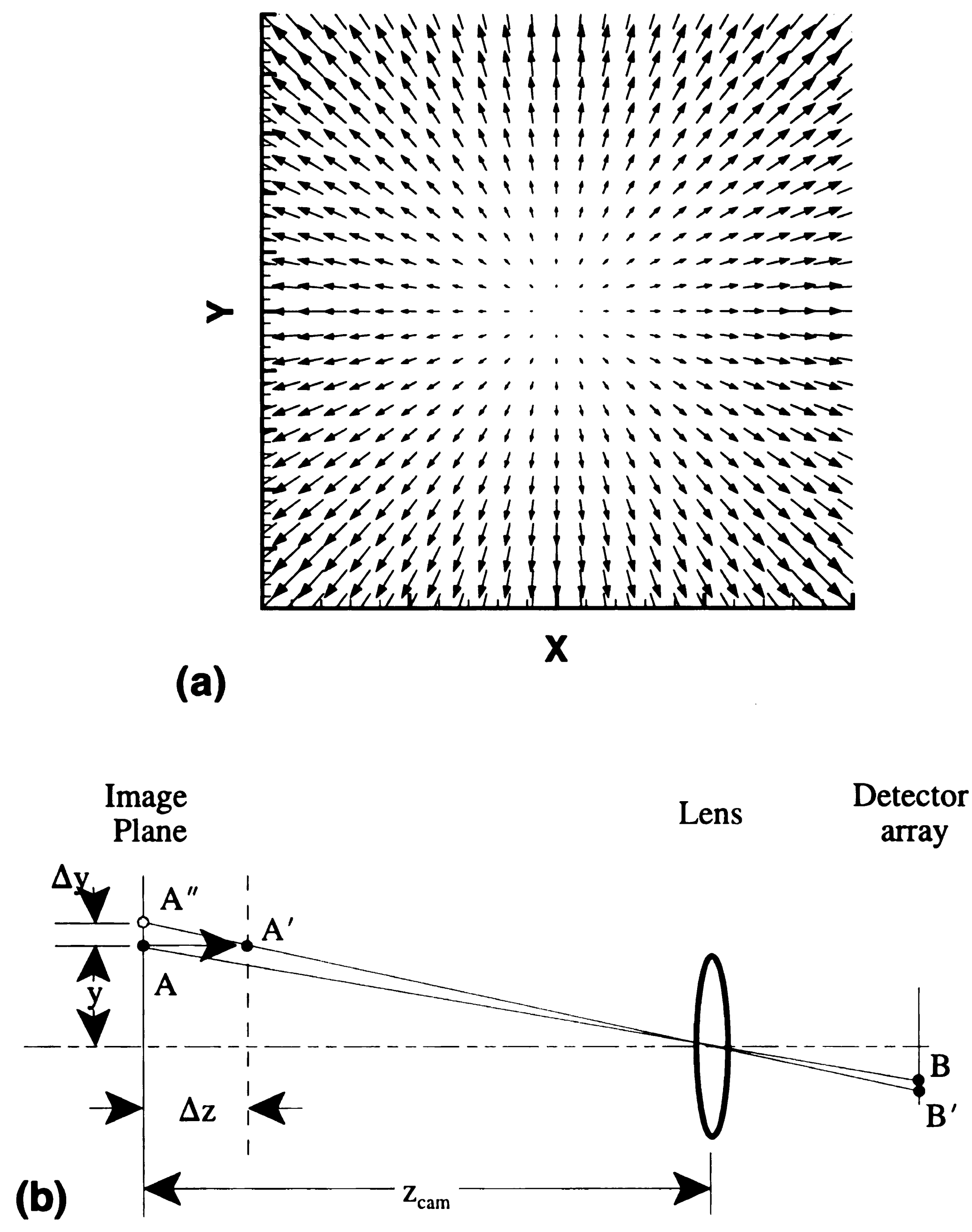

Figure 4.1: Diagram of the effect of out-of-plane motion on in-plane velocity estimates.

detector array. Using geometric optics, it can be shown that the point **B′** on the detector array is the image of the point **A″** in the image plane. Therefore, the forward motion of the tracer would be registered as an apparent upward motion on the detector.

In this arrangement, the in-plane displacement, Δx and Δy, caused by the out-of-plane motion, Δz, is related to the distance between the imaging system and the image plane, z_{cam}, and the distance from the center of the image plane, x, y. To first order, the relationship can be described by:

$$\Delta y = \frac{\Delta z}{z_{cam}} y$$

$$\Delta x = \frac{\Delta z}{z_{cam}} x,$$

where it is assumed that the out-of-plane motion Δz is small relative to z_{cam}. Similarly, the error in the velocity field measurements resulting from the out-of plane velocity for MTV (or PIV) type measurements can be found to be:

$$\Delta u = \frac{\Delta z}{z_{cam} \Delta t} x$$

$$\Delta v = \frac{\Delta z}{z_{cam} \Delta t} y,$$

where Δt represents the time delay between the successive image pairs and Δu, Δv represent the errors in the two in-plane velocity components. As seen in Figure 4.1a, the apparent velocity caused by this effect is zero in the center of the image plane and is a maximum at the edges of the image if the optical axes are exactly lined up. If the axes are not lined up, there will be an offset in the profile. The experiments reported in this chapter have been designed to attempt to minimize this effect. From the free-stream velocity and the time delay between image pairs, the mean out-of-plane motion in this experiment, Δz can be estimated to be *0.0375 cm*. The distance from the imaging plane to the camera, z_{cam}, is *75 cm*, and the maximum distance from the center of the measurement field to the edge (x and y) is *2 cm*. Thus, the maximum apparent displacement in either the x or y direction is *0.001 cm*, which corresponds to a velocity of *0.25 cm/s*. This is approximately *5%* of the peak velocities measured in this flow. Note that the *5%* error is only at the edges of the measurement. Other locations will have an error that is a smaller percentage of the peak velocity. This velocity error can be further minimized by the use of lens with a larger focal length. This would allow z_{cam} to be increased further. However, the 105 mm lens used was the largest available for use in this study.

If the out-of-plane motion is uniform, the vorticity value calculated from the in-plane velocity measurements is not affected by this error. The measured velocity can be defined as $u_{measured} = u_{actual} + \Delta u$ and $v_{measured} = v_{actual} + \Delta v$ where Δu and Δv are the apparent in-plane motions caused by the out-of-plane motion as have been defined above. Substituting the above expressions for $u_{measured}$ and $v_{measured}$ into the definition of vorticity:

$$\omega_z = \frac{\partial v}{\partial x} - \frac{\partial u}{\partial y}.$$

It is easily shown that vorticity is not affected by Δu and Δv. Returning to the expressions for Δu and Δv, it is clear that Δu is not dependant upon x, and Δv is not dependant upon y. Thus, the computed value of the vorticity field will be correct. A calculation of the vorticity field from the velocity field in Figure 4.1a confirms that the vorticity due to the out-of-plane motion is zero. Thus, even though the velocity vectors near the edges of the measurement field of view have an error which exceeds those specified in Chapter 3, the error in the vorticity field is not affected by this source of error.

4.2 Phase-averaging of cross-stream plane data

The data collected in the cross-stream measurement plane is phase-averaged in the same manner as the streamwise measurement plane data. Figure 4.2 shows a flooded contour plot of the phase-averaged streamwise vorticity, $<\omega_x>$ for four different downstream locations at a given phase. Overlaid on top of the flooded contours, contour lines of five instantaneous realizations from which the phase-averaged field is created are drawn. Note that only the right half of the test section is measured in these experiments. Both flow visualization, and a limited set of velocity and vorticity field measurements have shown that the locations of the vortical structures are nearly symmetric about $z = 0$ in this flowfield. However, the sign of the vortical structures is opposite in the two half-planes.

Figure 4.2a and 4.2b show the phase-averaged and instantaneous realizations for a typical phase at $x = 3\ cm$ and $10\ cm$ respectively. As can be seen, the instantaneous and the phase-averaged results overlay on top of each other very closely. At $x = 3\ cm$, the phase-averaged peak vorticity magnitude at this phase is $22\ s^{-1}$. At this location $(<\omega_x>_{rms})_{peak} = 1\ s^{-1}$. Discounting several points near the edges of the measurement field where some of the measurements are suspect due to the grid crossing impacting the wall of the facility, $(<\omega_x>_{rms})_{max} = 1.25\ s^{-1}$. The region where $(<\omega_x>_{rms})_{max}$ occurs at this, and all of the other streamwise locations, is in the shoulder regions of the $<\omega_x>$ distribution where a small amount of spatial wandering in this region of high gradient will result in large RMS values. At $x = 10\ cm$, structure of the streamwise vorticity field has changed rather dramatically. Several distinct structures of both positive and negative sign can be seen. The phase-averaged peak $<\omega_x>$ has dropped significantly to approximately $11\ s^{-1}$. At the location of

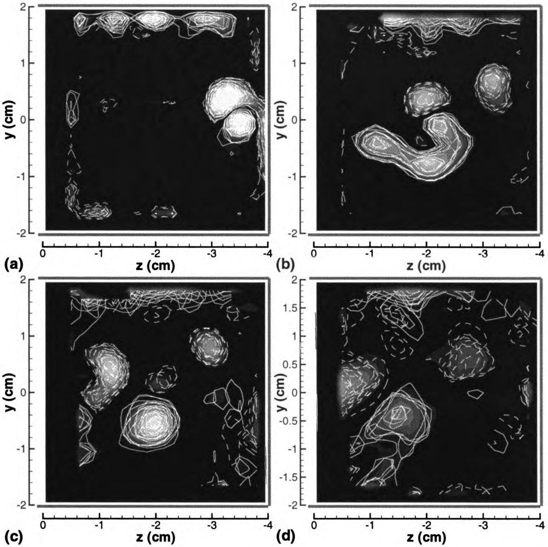

Figure 4.2: Comparison of the phase-averaged streamwise vorticity field with several instantaneous realizations of the streamwise vorticity field for four downstream measurement planes. Five instantaneous realizations are displayed in each plot and contour lines indicate the $\pm 3\ s^{-1}$, $\pm 6\ s^{-1}, \ldots, \pm 15\ s^{-1}$ with the dashed lines indicating the negative contour levels. (a) $x = 3\ cm$. (b) $x = 10\ cm$. (c) $x = 16\ cm$. (d) $x = 24\ cm$.

the $(<\omega_x>_{rms})_{peak} = 0.5\ s^{-1}$, however $(<\omega_x>_{rms})_{max}$ has increased slightly to approximately $1.5\ s^{-1}$. These results are comparable to that seen in the streamwise measurement results and are very near the expected uncertainty values inherent in the measurement.

Figure 4.2c compares the instantaneous and phase-averaged streamwise vorticity field at x = 16 cm. It is apparent that the cycle to cycle variation in the location of the regions of $<\omega_x>$ has increased from the earlier streamwise locations. The magnitude of the peak vorticity in this phase is approximately the same as that seen at $x = 10\ cm$ results, $\omega_{x,max} = 10.5\ s^{-1}$; however, $(<\omega_x>_{rms})_{peak}$ has increased dramatically to $1.5\ s^{-1}$. An increase is also seen in $(<\omega_x>_{rms})_{max} = 2.25\ s^{-1}$, nearly 25% of the peak vorticity levels. At $x = 24\ cm$, shown in 4.2d, the streamwise vorticity field shows further increases in the variation between the instantaneous realizations. The phase-averaged peak vorticity has been reduced to $7.5\ s^{-1}$ and $(<\omega_x>_{rms})_{peak}$ has increased to $1.75\ s^{-1}$ while $(<\omega_x>_{rms})_{max}$ has increased to $2.75\ s^{-1}$ at this downstream location. The increase in the spatial wandering of the $<\omega_x>$ field likely results in the peak vorticity values being reduced compared to the instantaneous results due to averaging out of the peak vorticity values. However, even with the considerable amount of deviation from realization to realization in this far downstream location, it is apparent that much commonality exists among these instantaneous realizations in terms of the general structure of the vorticity field. For example, examining at the vortical structure located at $(y, z) = (0.5, -2.75)$, it is apparent that all of the instantaneous realizations contain a positively signed vortex at this location. However, the exact location of the center of this vortex has wandered from realization to realization.

At the $x = 3\ cm$ and $x = 10\ cm$ measurement stations, it is felt that the phase-averaged results provide an accurate representation of both the spatial location and the magnitude of the instantaneous streamwise vorticity field. At these stations, the variation of the individual realizations of each phase is comparable to those in the streamwise measurements and nearly identical to the expected measurement uncertainty. As the fluid travels downstream, small scale motions and spatial wandering result in the smearing of the $<\omega_x>$ field in the phase-averaged results. This will result in the peak values of ω_x being reduced from the instantaneous realizations and the apparent size of the regions of streamwise vorticity being slightly increased. However, the phase-averaged results do provide an accurate description of the spatial location of the ω_x in this flow.

4.3 Mean flow properties of the cross-stream plane

Figure 4.3 shows the overall mean of the streamwise vorticity field for the unforced, A = 7.3%, and A = 11.6% cases at four different downstream locations. These two forcing cases were selected as they are representative of the qualitative features seen in the other forced cases. The lowest amplitude (2.1% forcing) case will not be shown in this section as the small levels of the streamwise vorticity are very difficult to discern without the extensive use of color to accentuate the vorticity field, and the qualitative features found in this forcing amplitude are also seen in the 7.3% forcing case. As has been previously described, these cases are the counterparts to the medium and high forcing amplitude cases in the mixing study of Koochesfahani and Nelson (1997).

The unforced flow shown in the first column does not show the presence of any $\overline{\omega}_x$. This absence is not the result of positively and negatively signed vorticity averaging to a small value. Rather, the instantaneous levels of ω_x are nearly zero at all *(y, z)* locations. In contrast, $\overline{\omega}_x$ is seen at all of the downstream locations studied for all of the forcing cases. At the far upstream measurement location, the presence of a counter-rotating vortex pair can be seen close to the sidewall of the facility. Generally, as the downstream location increases, the strength of the mean vorticity decreases. In the 7.3% forcing case, the peak value of $\overline{\omega}_x$ decreases from $10\ s^{-1}$ at $x = 3\ cm$, to $5\ s^{-1}$ at $x = 8.5\ cm$ and remains relatively constant at this level through the last measurement location, $x = 24\ cm$.

Examining the streamwise vorticity field for the 11.6% forcing case, it can be seen that at $x = 3\ cm$, the structure of $\overline{\omega}_x$ looks very similar to that seen in the 7.3% forcing case. However, the magnitude of the peak $\overline{\omega}_x$ is about 50% larger than in the 7.3% case, $\overline{\omega}_x$ = $15\ s^{-1}$. At $x = 8.5\ cm$, the mean streamwise vorticity field shows significant differences from the lower amplitude cases. Three distinct regions of mean $\overline{\omega}_x$ are seen; two in the upper half-plane and one in the lower half-plane. The peak vorticity among these three cores is $11\ s^{-1}$. At $x = 16\ cm$, there are at least *4* distinct regions of concentrated vorticity. The peak mean $\overline{\omega}_x = 7\ s^{-1}$ among the four regions. At $x = 24\ cm$, most of the regions of vorticity have moved near the centerline of the test section. These additional structures will have the effect of increasing the amount of mixed fluid in the wake as their presence causes more fluid from the top and bottom streams of the test section to interact.

In addition to the appearance of the additional cores, the spatial location of these cores is very different from that observed in the 7.3% forcing case. At $x = 8.5\ cm$, the streamwise vorticity field for the 11.6% forcing case occupies a region of the test section ranging from $-3.5\ cm < z < -1\ cm$. In contrast, the mean $\overline{\omega}_x$ in the 7.3% case remains less than 1 cm from the sidewall of the facility. By $x = 16\ cm$, this region of mean vorticity encompasses nearly the entire measured half of the test section in the high amplitude forcing

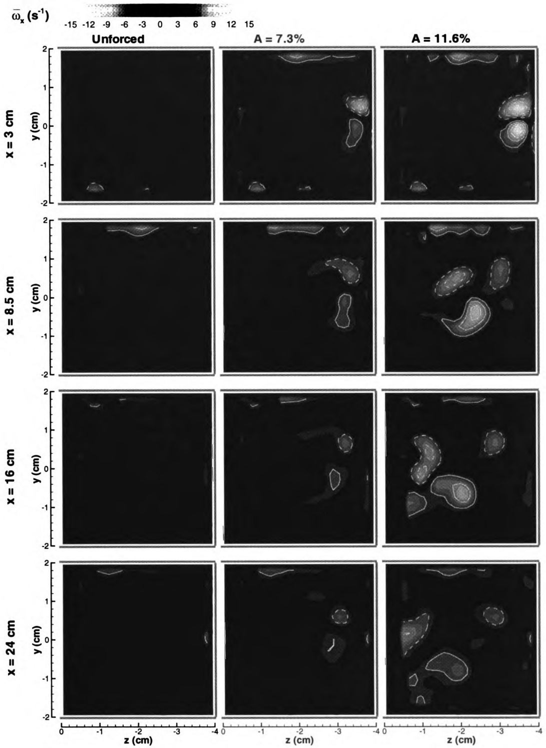

Figure 4.3: Mean streamwise vorticity field for the unforced, 7.3%, and 11.6% forcing cases at four different downstream locations. Contour lines indicate the $\pm 3\ s^{-1}$, $\pm 6\ s^{-1}$,..., $\pm 15\ s^{-1}$ with the dashed lines indicating the negative contour levels.

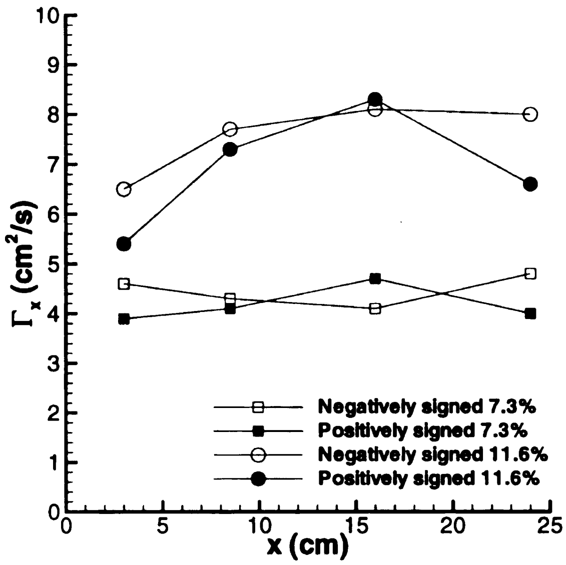

Figure 4.4: Circulation of the average vorticity field of the right half measurement plane for the 7.3% and 11.6% forcing conditions.

case, whereas these locations have changed very little in the lower amplitude case. Since the positioning of both the mean and instantaneous vorticity field is symmetric about $z = 0\ cm$, the 11.6% forcing case results in the entire test section containing regions of mean streamwise vorticity. These large scale motions generate additional surface area for the unmixed fluids to come into contact and likely result in an increase in the amount of mixed fluid. By $x = 24\ cm$ downstream, the regions of $\overline{\omega}_x$ in the 11.6% case have moved even closer to the centerline of the facility.

The additional cores found in the high amplitude forcing case after $x = 8.5\ cm$ are not the result of the primary vortices splitting. Rather, there is an increase in the amount of vortical fluid. This can be seen in the Figure 4.4 showing the mean circulation of both the positively signed and negatively signed $\overline{\omega}_x$ for the 11.6% and 7.3% forcing cases. Γ_x is computed by integrating all positive (or negative) vorticity values above the $\pm 1\ s^{-1}$ threshold over the measured half of the test section. The boundary layer regions on the top and bottom surfaces were excluded from the integration, however the boundary layer region on the sidewall was included. Small positive and negative background values of $\overline{\omega}_x$ found within the integration region will cause the value of Γ_x to overestimate the circulation values of the vortex cores. However, as these background values should be similar at the different downstream locations, it is fair to compare Γ_x with one another. For the 11.6% forcing case, there is a significant increase in the overall circulation between $x = 3\ cm$ and $x = 16.5\ cm.$ In contrast, the circulation of the 7.3% forcing case is relatively constant. It will be shown in section 4.8 that these additional structures are the result of the reorientation of the spanwise vorticity into the streamwise direction. It is noted that the value of Γ_x are not the same for the positively and negatively signed vorticity distributions. It is believed that this is caused by small differences in the velocity of the two streams. However, because of the symmetry of the flow, the $\overline{\omega}_x$ field in the left half-plane will have the same magnitude and location of those measured in the right half-plane, but with an opposite sign. This will result in a net zero circulation if the entire test section is considered.

In Figure 3.12, the $\overline{\frac{\partial w}{\partial z}}$ field for the wake forced wake at several different perturbation amplitudes was shown. For the 11.6% and larger forcing cases, the arrangement of the $\overline{\frac{\partial w}{\partial z}}$ field was consistent with the presence of a mean recirculating flow pattern in the cross-stream plane. The lower forcing amplitudes showed no indication of this type of motion. The velocity measurements over the cross-stream plane shown in Figure 4.5 confirm the presence of this flow field for the 11.6% forcing amplitude results. The mean recirculating flow pattern is most obvious in the x = 8.5 cm measurement plane, however, this pattern continues to be seen at x = 16 cm and x = 24 cm. Note that this pattern is not observed in the unforced or the 7.3% forcing results.

Based on the mean velocity and vorticity results, it can be reasoned that this

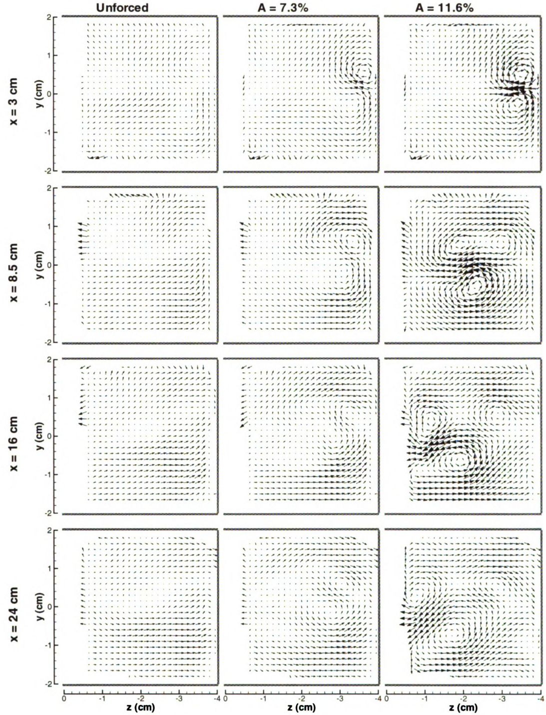

Figure 4.5: Mean velocity field over the cross-stream plane for the unforced, 7.3%, and 11.6% forcing cases at four different downstream locations.

recirculating pattern will result in more mixed fluid in the 11.6% forcing case as compared to the lower amplitude cases. The mean "pumping" action resulting from the vortex arrangement causes fluid located in the top and bottom regions of the facility which is typically unmixed, to be pumped towards the central region where they can combine. This action will result in an increase in the amount of mixed fluid. The fluid in the central region of the test section, which is typically mixed, is also pumped back into the typically unmixed top and bottom regions. This results in an increase in the thickness of the mixed fluid layer. Thus, the mean recirculatory flow pattern will result in an increase in the amount of molecularly mixed fluid, and in the mixed fluid taking up a larger width within the test section.

4.4 Downstream development of the phase-averaged streamwise vorticity

Figure 4.6 shows a perspective view of the phase-averaged streamwise vorticity field for the 11.6% forcing results at two different phases within the forcing cycle. The two phases are separated by approximately ½ of the forcing cycle. Results from *11* different measurement planes are displayed on the same plot. Note that the side-walls of the flow facility are located at $z = -4$ and no wall exists at mid-plane ($z = 0$). At both phases, the farthest upstream plane shows evidence of two distinct vortex cores located close to the side-walls of the facility. In the first phase, shown in 4.6a, the negatively signed vortex located just above the center-line has a peak $\langle\omega_x\rangle = -26\ s^{-1}$. This is twice as large as that seen in the positively signed vortex core ($13\ s^{-1}$) below the center-line. This situation is nearly reversed in the second phase shown in Figure 4.6b where the positively signed vortex core below the center-line has a magnitude ($24\ s^{-1}$) that is 50% larger than the negatively signed

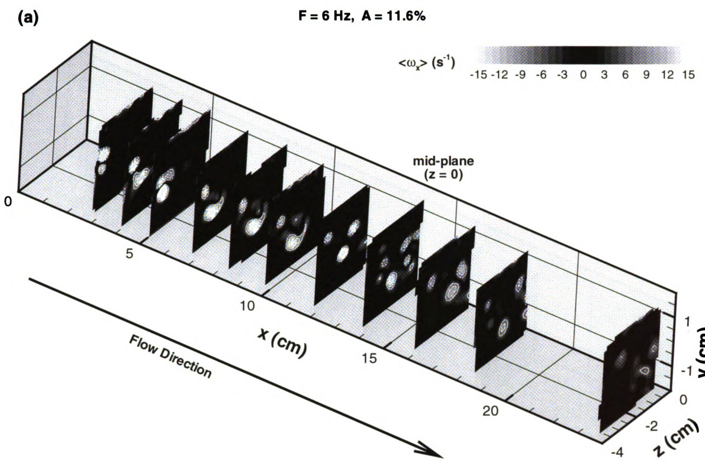

Figure 4.6: Downstream development of the phase-averaged streamwise vorticity for the 11.6% forcing case at two arbitrarily selected phases within the forcing cycle. Note that the facility sidewalls are located at $z = -4\ cm$. The axis displayed at $z = 0$ is the center of the test section. Contour lines indicate the $\pm 6\ s^{-1}$, $\pm 9\ s^{-1}, \ldots, \pm 15\ s^{-1}$ with the dashed lines indicating the negative contour levels. (a) $\phi = 0.21$. (b) $\phi = 0.62$.

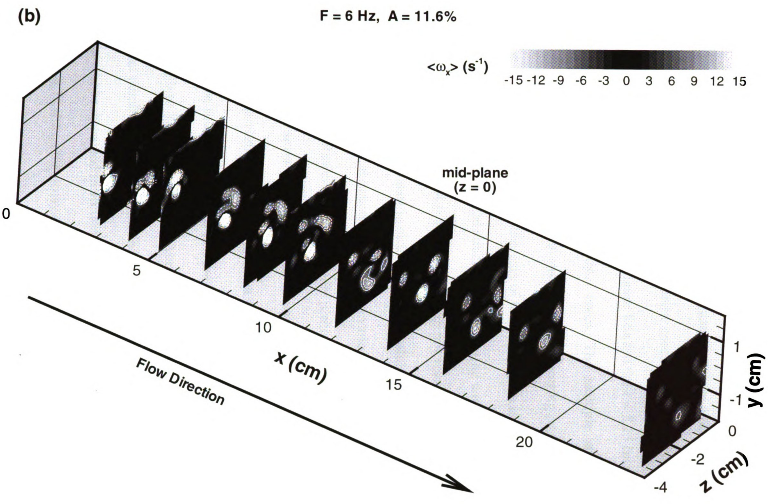

Figure 4.6: continued.

core ($-16\ s^{-1}$) above the center-line. The variation of the strength of the streamwise vorticity with phase will be discussed further in section 4.5.

An interesting effect is seen in the next two downstream planes ($x = 4.25\ cm$ and $x = 5.25\ cm$) of Figure 4.6. In both the $x = 5.25\ cm$ plane in Figure 4.6a and the $x = 4.25\ cm$ plane in Figure 4.6b, the negatively signed vortex core appears to have split into two portions. However, the $x = 4.25\ cm$ plane of Figure 4.6a and the $x = 5.25\ cm$ plane of Figure 4.6b do not show signs of these multiple cores. The multiple structures are not distinguishable at these downstream locations due to the averaging process. More vortical structures are seen as the distance downstream of the splitter plate increases. However, the magnitude of the peak vorticity of the structures is decreasing with the increasing x.

When examining Figure 4.6, it is important to not visually connect the streamwise vorticity among the various planes in order to create a volumetric image of the underlying vortex structure. The vortical structures seen in the various planes are not necessarily part of the same vortex tube. Rather, the measurement planes show the streamwise projection of the vorticity vector for several different vortex tubes. Within each measurement plane, the spanwise slice of the vorticity field will intersect with the projection of $<\omega_x>$ for different vortex tubes. The multiple structures that are seen in several planes are the result of the measurement plane intersecting multiple vortex tubes Each measurement phase plane will cut a different number of tubes. A detailed description of the topology of the vorticity field in this flow will be discussed in section 4.8.

Figure 4.7a shows the decay of the peak levels of $<\omega_x>$ with downstream distance. This value was determined by searching for the peak level of $<\omega_x>$ within all of the phases at a given x location. For the 11.6% forcing case the absolute value of the peak streamwise

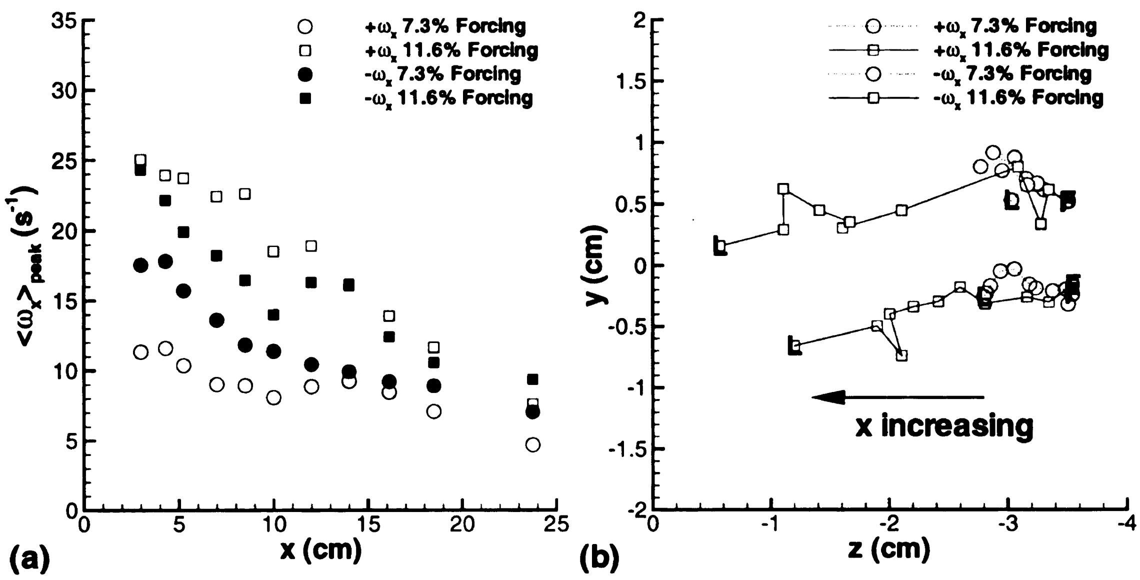

Figure 4.7: Variation of the magnitude and position of the peak value of $<\omega_x>$ field for the 7.3% and 11.6% forcing cases. (a) Variation of peak magnitude of $<\omega_x>$ with downstream distance. (b) Change in location of peak $<\omega_x>$ with downstream distance. The farthest upstream location ($x = 3.25\ cm$) is marked with an "F" and the farthest downstream location ($x = 23.75\ cm$) is marked with an "L".

vorticity is $<\omega_x>_{max} = 25\ s^{-1}$ at $x = 3\ cm$. This value decreases to $11\ s^{-1}$ by $x = 24\ cm$. Note that this value may be underestimated by the smearing of the phase-averaged vorticity due to the spatial wandering of the streamwise vortices. For the 7.3% forcing case, the initial peak streamwise vorticity level is $<\omega_x>_{max} = 18\ s^{-1}$ at $x = 3\ cm$ and decreases to about $9\ s^{-1}$ at $x = 24\ cm$. This is similar to decay of the spanwise vorticity where it was found that the peak vorticity decreased with streamwise location. As is also seen in the $<\omega_z>$ results, the rate at which $<\omega_x>$ decays for 11.6% forcing is faster than the rate at which $<\omega_x>$ decreases in the 7.3% forcing and lower forcing levels.

Comparing the peak streamwise vorticity levels with the peak spanwise levels at the same downstream location, $\frac{<\omega_x>_{max}}{<\omega_z>_{max}} = 0.6$ for the 11.6% forcing case. For the 7.3% forcing case, this value is found to be even larger with $\frac{<\omega_x>_{max}}{<\omega_z>_{max}} = 0.8$. These values are considerably larger than those found in the free wake studies conducted by LeBoeuf and Mehta (1996), who found the ratio of the peak streamwise vorticity to spanwise vorticity values to be 40%, and the study by Weygandt and Mehta (1995), who found this ratio to be 20%. The Reynolds number for these studies was $Re_\theta \approx 350$, which is slightly higher than the present work

It is believed that the true value of the ratio of $<\omega_x>_{max}$ to $<\omega_z>_{max}$ in the forced confined wake flow depends on downstream location and has a peak value of at least *1*. In Appendix A, the effect of spatial filtering on the peak vorticity levels is examined. It was found that as the measurement density decreased, the peak vorticity levels are underestimated by an increasing amount. As the streamwise vortex cores are generally seen to be more compact, the normalized measurement density, L/δ, is smaller than that found for the spanwise vortex cores and the resulting bias error in the measurement will be larger. Thus the peak values of $<\omega_x>_{max}$ are expected to be underestimated by a larger fraction than that for $<\omega_z>_{max}$. This matter will be examined further in section 4.9 where the standard density measurements will be compared with a set of higher density measurements.

The spatial location where the peak streamwise vorticity occurs within the cross-stream plane, seen in Figure 4.7b, reveals an interesting difference between the 11.6% and the 7.3% forcing cases. This plot displays the (y, z) location where the peak vorticity is found. The first and last streamwise locations for each vortex is specially marked. In general, x increases towards the left. For both forcing cases, the peak positive vorticity is always located in the bottom half of the test section while the peak negative vorticity is located in the top half of the test section. For the 11.6% forcing case, the spanwise location of the peak streamwise vorticity moves in from near the sidewall of the test section located at $z = -4$ *cm* towards the center. However, for the 7.3% forcing case, the location of the peak vorticity remains confined in the region $-3.75cm < z < -2.75\ cm$. This effect was also seen in the results for the overall mean vorticity

The location of the phase-averaged streamwise vortical field with respect to downstream location for the 7.3% forcing case can be seen in the perspective plot found in Figure 4.8. At the farthest upstream planes, there is evidence of only one negatively signed region of vorticity. As will be seen in section 4.5, this is a result of the particular phase selected. Other phases show the presence of a positively signed vortex core in the bottom half-plane. As the flow develops downstream, the existence of additional streamwise vortical structures closer to the center-plane is noted, however, their strength is considerably weaker than that of the regions of vorticity close to the wall. In contrast, the regions of ω_x that move towards the center in the 11.6% forcing case are stronger than those close to the wall.

4.5 Variation of the streamwise vorticity field with phase

A = 11.6%

As with the variation seen with downstream location, the streamwise vorticity field also shows a large variation with phase at each downstream location. The variation of the strength of the $<\omega_x>$ field at $x = 3\ cm$ for eight equally spaced phases, ϕ, within the forcing cycle can be seen quite clearly in Figure 4.9. Recall that ϕ varies in the range $0 < \phi < 1$ in this study. In order to more easily reference the phases shown in the figure, they have been labeled *1-8*. The vorticity magnitude of the two structures is clearly changing between a peak

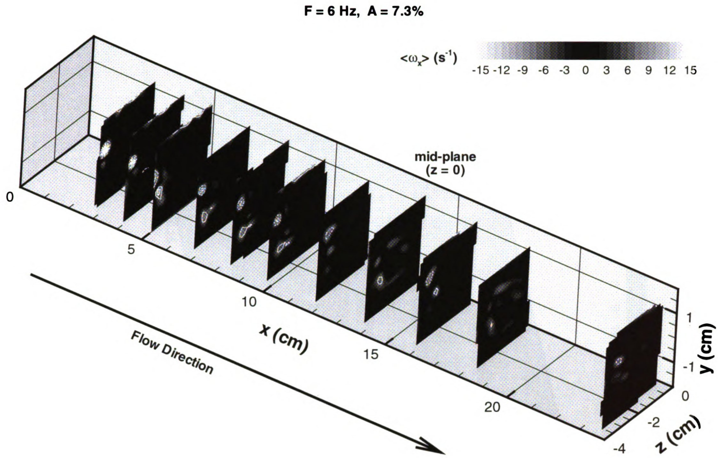

Figure 4.8: Downstream development of the phase-averaged streamwise vorticity for the 7.3% forcing condition for $\phi = 0.21$. Note that the facility sidewalls are located at $z = -4\ cm$. The axis displayed at $z = 0$ is the center of the test section. Contour lines indicate the $\pm 6\ s^{-1}$, $\pm 9\ s^{-1}, \ldots, \pm 15\ s^{-1}$ with the dashed lines indicating the negative contour levels.

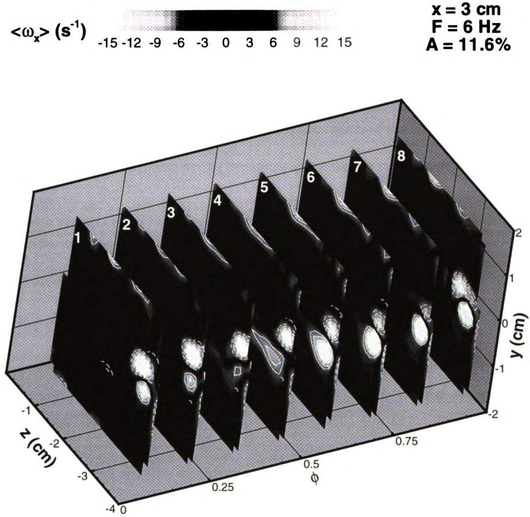

Figure 4.9: Variation of the streamwise vorticity with phase at $x = 3\ cm$ for the 11.6% forcing amplitude. Contour lines indicate the $\pm 6\ s^{-1}$, $\pm 9\ s^{-1}$,..., $\pm 15\ s^{-1}$ with the dashed lines indicating the negative contour levels.

of the negatively signed streamwise vortex tube, located in phase *2*, and a peak in the ositively signed streamwise vortex tube located in phase *6*. Both peaks are located at a spanwise location of $z = -3.5\ cm$. In between these vorticity peaks, such as in phase *4* and *8*, there are phases in which the streamwise vorticity extends out from the wall towards the center region of the test section. Note that these levels are less than the smallest contour line displayed, however, they can still be seen in the flooded contour.

Figure 4.10 shows the variation with respect to phase for the downstream location $x = 5.25\ cm$. In this plane, the spanwise location of the region of peak vorticity has moved inwards to $z = 3\ cm$. Some noteworthy dynamics are occurring in this measurement plane. Starting from phase *1*, two distinct vortex cores are noted. A positively signed core is located in the lower half-plane and a negatively signed core is located in the upper half-plane. At the second phase, two nearly distinct negatively signed vortex cores are apparent in the upper half-plane. In this plane, the outermost core has a larger radius and peak vorticity. It is hypothesized that these two cores are the result of the reorientation of the primary spanwise vorticity from two of the negatively signed $<\omega_x>$ cores located one wavelength apart.

Although the splitting mechanism described in Visbal, Gaitonde, and Gogeneni (1998) was seen in the streamwise measurements presented in section 3.5, it is believed that this mechanism is not responsible for the increase in the number of regions of streamwise vorticity and the enhanced mixing field found in this flow. In section 3.5, it was seen that the regions of negative $<\omega_z>$ that split off of the "primary" negative spanwise vortex roller moved from the bottom half of the test section to the top half of the test section. These "secondary" cores became aligned horizontally with the positively signed primary roller in

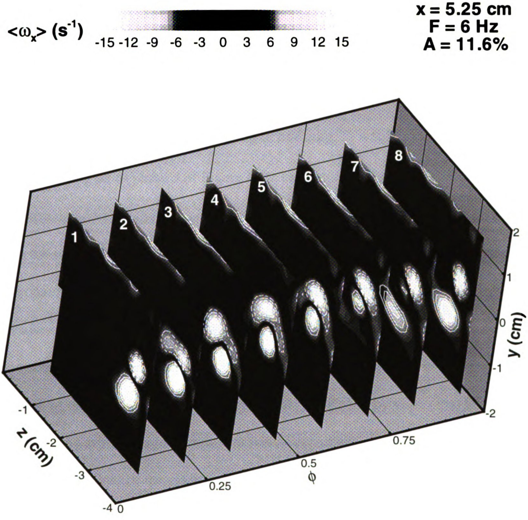

Figure 4.10: Variation of the streamwise vorticity with phase at x = *5.25 cm* for the 11.6% forcing amplitude. Contour lines indicate the $\pm 6\ s^{-1}$, $\pm 9\ s^{-1}$,...,$\pm 15\ s^{-1}$ with the dashed lines indicating the negative contour levels.

the top half of the test section. Similarly, the secondary cores split from the positively signed spanwise roller moved into the bottom half of the test section. If these secondary cores, which were generated by splitting from the primary core, are reoriented into the streamwise direction, regions of both positive and negative $<\omega_x>$ would be seen in both the top and bottom halves of the test section. This is not the case. It is believed that if these secondary cores are reoriented into the streamwise direction, they are quickly canceled by reoriented primary roller. Furthermore, in Figure 4.4, it was found that Γ_x increased with *x*. If the multiple cores were the result of the splitting of one core, Γ_x would remain constant.

Continuing on to phase *3* of Figure 4.10, two regions of negatively signed vorticity are still present, however, they are not as distinct as seen in phase *2*. The lack of distinctness is due to the lack of sufficient spatial resolution to properly distinguish the two regions. It is also apparent that in this phase, the innermost (farthest away from the wall) core has a larger radius and vorticity value. In phase *4*, the weakening outermost region of negatively signed vorticity is drawn around the positively signed region, which is at its maximum value. This region of negatively signed vorticity is further weakened by vortex cancellation as it merges with the positively signed vortex, or will be absorbed into the boundary layer region.

The second half of the cycle is nearly the reverse of the first half. From phase *4* to *5*, the region of positively signed vorticity shrinks in core radius. This continues into phase *6*, however, a second positively signed core can be just seen to the inside of the core weakening outer (closer to the sidewall) region of positively signed vorticity. As this core becomes smaller it is continues to move around the strengthening $<\omega_x>$. In phase *7*, the "new" region of positively signed $<\omega_x>$ is clearly apparent while the "old" region has nearly disappeared. In phase *8*, two oppositely signed regions of vorticity are again noted much as in phase *1*. In this phase, the region of positively signed streamwise vorticity is a maximum.

The appearance of this new region of streamwise vorticity in phases *2* and *6* can be connected to the passage of the spanwise vorticity at this x location. This effect will be shown by examining the causes for the development of the new region of $+\langle\omega_x\rangle$ at approximately $z = -3\ cm$ in phase *6* of Figure 4.10. Figure 4.11 shows the spanwise vorticity field for the $z = -2.5\ cm$, $-3\ cm$, $-3.5\ cm$ measurement planes at the phase corresponding to phase *6* of Figure 4.10. In $z = -3\ cm$ plane of Figure 4.11, a positively signed spanwise vortex is positioned at the streamwise location of the measurements seen in Figure 4.10, $x = 5.25\ cm$. This location is marked with a line in the three streamwise plane measurements. Examining the streamwise locations of the spanwise rollers in Figure 4.11, the x location of the spanwise roller at $z = -2.5\ cm$ is seen to be located nearly $\frac{1}{2}\lambda$ downstream of the location of the roller streamwise position at $z = -3\ cm$. Between $z = -3\ cm$ and $z = -3.5\ cm$, spanwise location of the tube remains nearly constant, however the magnitude of the peak vorticity within the core has decreased dramatically.

The new region of $\langle\omega_x\rangle$ formation in phase *6* of Figure 4.10 is the result of the reorientation of the positively signed spanwise vortex tube as it passes this location. From the measurements of the spanwise vorticity, it can be seen that the spanwise roller is experiencing a large amount of bending in the streamwise region where the new $\langle\omega_x\rangle$ is formed. This bending is the reorientation of the vortex tube. As the phase continues to increase, the magnitude of the peak vorticity of the streamwise vorticity increases as the central part of the roller convects downstream and the streamwise "legs" are stretched. The maximum magnitude of streamwise vorticity is achieved 1/4 of the forcing cycle later in phase *8*.

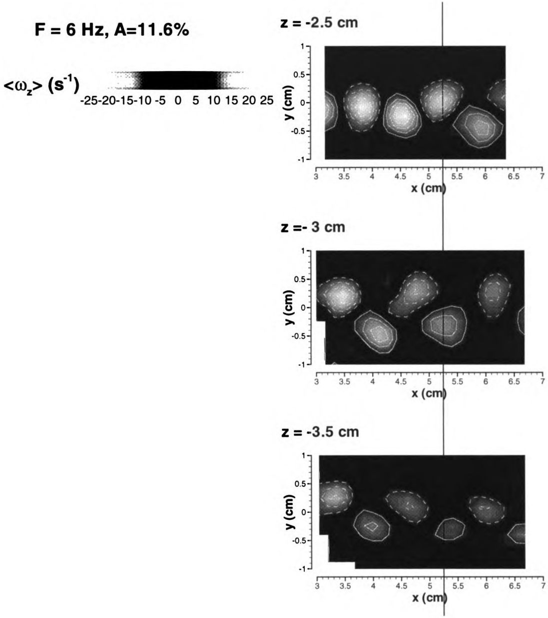

Figure 4.11: Spanwise vorticity field in the range *-3.5 cm < z < -2.5 cm*. The phase corresponds to phase **6** of Figure 4.10. Contour lines indicate the $\pm 5\ s^{-1}$, $\pm 10\ s^{-1}$,...,$\pm 25\ s^{-1}$ with the dashed lines indicating the negative contour levels.

In the study of the free-wake conducted by LeBoeuf and Mehta (1996), it was found that the location of the peak streamwise vorticity values were coincident with the locations of the peak spanwise vorticity values. In the semi-confined wake of the current work, the peak magnitude of the streamwise vorticity at a particular location in the flow occurs after the passage of the spanwise vorticity at that point.

Figure 4.12 shows the streamwise vorticity distribution for the 11.6% forcing cases for several phases at $x = 8.5cm$. This plot contains the same type of information displayed in Figures 4.9 and 4.10; however, the inward movement of the streamwise vorticity makes it difficult to discern important features in the three-dimensional perspective plot. As seen at $x = 5.25\ cm$, multiple vortical structures are apparent at all phases within the forcing cycle. These structures, occupy a considerably larger region of the test section than the regions of $\langle\omega_x\rangle$ at $x = 5.25\ cm$. The variation in the streamwise vorticity field with respect to phase is caused by the passage of the most recent spanwise vortex tube, which generates more streamwise structures the reorientation, and the interaction of the new $\langle\omega_x\rangle$ with the "legacy"$\langle\omega_x\rangle$ created earlier by the passage of spanwise vortices several forcing cycles prior. Examination of an animation of these data reveal that the "newest" regions of streamwise vorticity are generated closer to the center of the test section. This process will be described further in section 4.8. As the flow continues downstream, more of these structures are generated. Figure 4.13 shows the streamwise vorticity distribution for this forcing case *16 cm* downstream of the splitter plate. At this location, even more structures are apparent than in the $x = 8.5\ cm$ case and the vast majority of the test section is occupied by vortical fluid.

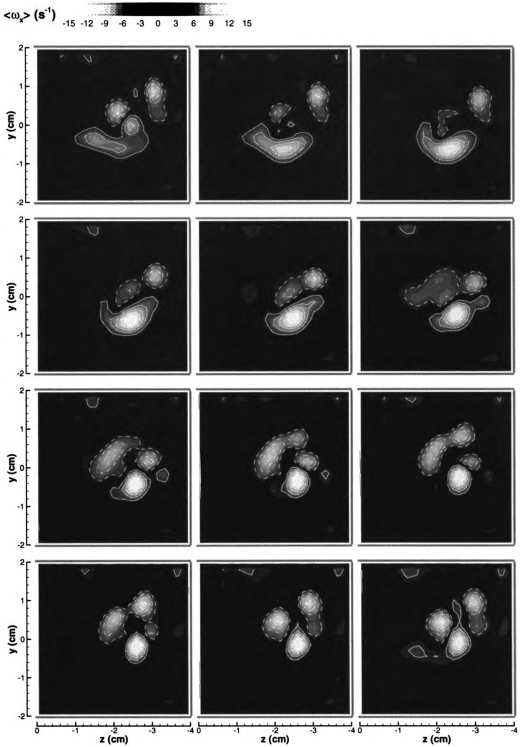

Figure 4.12: Variation of the streamwise vorticity with phase at x = *8.5 cm* for the 11.6% forcing amplitude. The displayed phases are separated by approximately $\Delta\phi$ = *0.08* and phase runs from right to left and then top to bottom. Contour lines indicate the $\pm 3\ s^{-1}$, $\pm 6\ s^{-1}$,...,$\pm 15\ s^{-1}$ with the dashed lines indicating the negative contour levels.

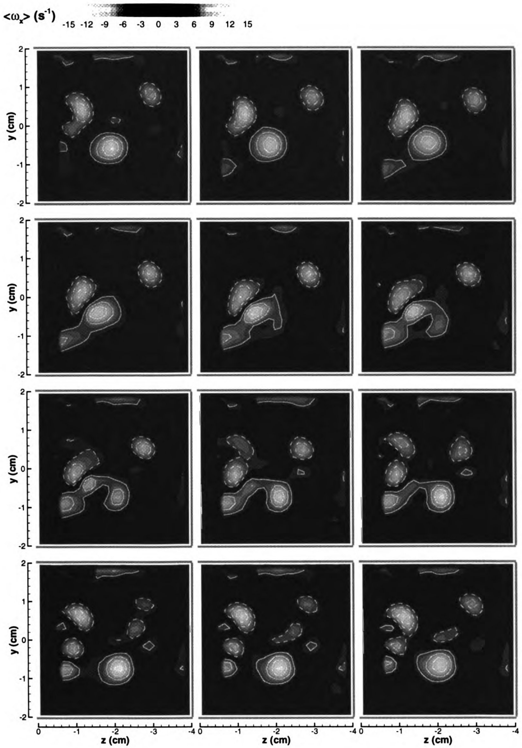

Figure 4.13: Variation of the streamwise vorticity with phase at x = *16 cm* for the 11.6% forcing amplitude. The displayed phases are separated by approximately $\Delta\phi = 0.08$ and phase runs from right to left and then top to bottom. Contour lines indicate the $\pm 3\ s^{-1}$, $\pm 6\ s^{-1}$,..., $\pm 15\ s^{-1}$ with the dashed lines indicating the negative contour levels.

A = 7.3%

As with the 11.6% forcing case, the 7.3% forcing case also shows a large variation with phase. Figure 4.14 shows a perspective plot of *8* different phases in the forcing cycle for the streamwise location of $x = 3\ cm$. As with the measurements of this plane for the 11.6% forcing case, two regions of streamwise vorticity are noted; a negatively signed region in the upper half plane, and a positively signed region in the lower half plane. Unlike in the 11.6% case, there are many phases where one of the signs of $<\omega_x>$ is not present. Note that the region of negative $<\omega_x>$ in phases **3-8** is located very close to the sidewall and is difficult to resolve.

The 7.3% forcing amplitude case develops additional streamwise vortices as the flow develops. Due to the decreased magnitude of the spanwise vorticity, from which the streamwise vorticity is generated through the reorientation, the additional vortices have a significantly reduced magnitude. Figure 4.15 shows the streamwise vorticity field at $x = 5.25\ cm$. Similar to the results of the 11.6% forcing, the locations of the new regions of $<\omega_x>$ are farther apart in the transverse (y) direction. This is similar to the effect noted in the 7.3% forcing case in Chapter 3 where it was found that the transverse spacing among regions of $<\omega_z>$ increased. Phase **1** shows the presence of two regions of ω_x. As phase increases, a second region of streamwise vorticity begins to develop starting in phase 3. It is located farther away from the sidewall of the facility and is closer to the top wall of the facility. Continuing on in phase development, the negatively signed streamwise vortex increases in intensity as it is stretched while the positively signed streamwise vortex decays. In phases 7 and 8, the positively signed region streamwise vorticity field is regenerated by the passage

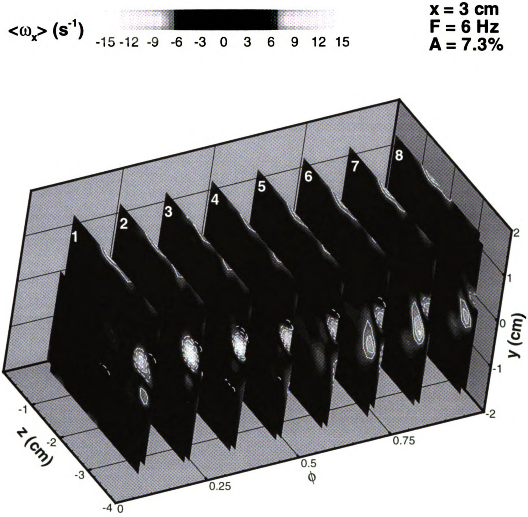

Figure 4.14: Variation of the streamwise vorticity with phase at $x = 3\ cm$ for the 7.3% forcing amplitude. Contour lines indicate the $\pm 6\ s^{-1}$, $\pm 9\ s^{-1}$,..., $\pm 15\ s^{-1}$ with the dashed lines indicating the negative contour levels.

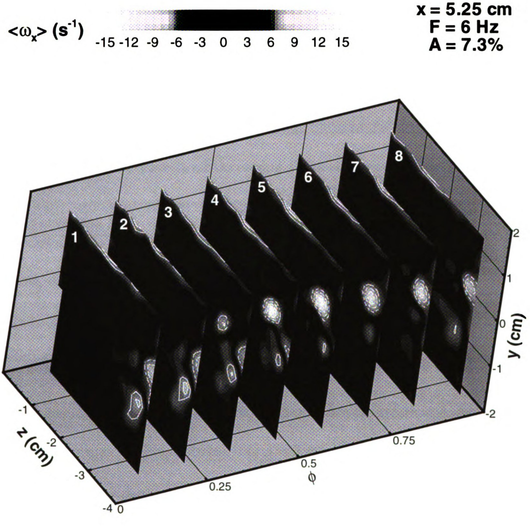

Figure 4.15: Variation of the streamwise vorticity with phase at x = *5.25 cm* for the 7.3% forcing amplitude. Contour lines indicate the $\pm 6\ s^{-1}$, $\pm 9\ s^{-1}$,..., $\pm 15\ s^{-1}$ with the dashed lines indicating the negative contour levels.

of the positively signed spanwise vortex which is reoriented into the streamwise direction at a location farther from the sidewall and closer to the bottom wall of the test section.

The process of the creation of streamwise vorticity from the reorientation of spanwise vorticity continues at locations farther downstream. Figure 4.16 shows the streamwise vorticity field at $x = 8.5\ cm$. At this downstream location, the presence of multiple vortical structures of both sign is apparent. Note that the perspective view makes some of these structures difficult to discern. Unlike the 11.6% forcing results, these structures have not moved towards $z = 0\ cm$. Rather, they are staying close to the sidewall of the facility. Although the peak vorticity levels are decreasing, the qualitative characteristics remain the same; multiple regions streamwise vorticity is noted, however, these structures remain close to the sidewall. As seen earlier in Figure 4.7b, although the peak vorticity levels are decreasing, the mean circulation value remains constant through $x = 24\ cm$.

4.6 Relationship of streamwise vorticity field to mixing results

Several interesting comparisons can be made between the streamwise vorticity results and the mixing results of Nelson (1996). For $A < 7.3\%$, the regions of both $\overline{\omega}_x$ and $<\omega_x>$ remain close to the sidewalls of the facility and no $\overline{\omega}_x$ or $<\omega_x>$ is present in the central region of the test section. This is consistent with the mixing results of Nelson (1996) where it is shown that when the low and middle amplitude forcing are applied, the z location of the peak amount of mixed fluid is initially located near the sidewall of the facility. As x increases, the region of peak mixed fluid also moves very slowly towards the center of the test section. In contrast, in the high amplitude forcing results, the z location of peak mixing moves towards the center of the test section very quickly. This is the same as the behavior

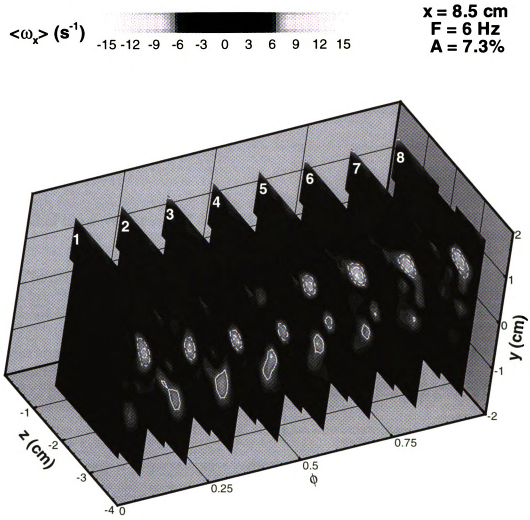

Figure 4.16: Variation of the streamwise vorticity with phase at x = *8.5 cm* for the 7.3% forcing amplitude. Contour lines indicate the $\pm 6\ s^{-1}$, $\pm 9\ s^{-1}$,..., $\pm 15\ s^{-1}$ with the dashed lines indicating the negative contour levels.

of the regions of $\overline{\omega}_x$ and $<\omega_x>$.

Generally, increases in the amount of mixed fluid in this type of flow have been attributed to increases in the amount streamwise vorticity in a flow. At center span, the Nelson found that the middle amplitude forcing case was a better mixer than the low amplitude forcing case which was a better mixer than the unforced case. This was seen in Figure 1.3. However, the present study shows that no $\overline{\omega}_x$ or $<\omega_x>$ are found at this spanwise location for any of these forcing conditions. Thus, the mixing increase for these cases must be a result of the increase in ω_z.

4.7 Model of the development of the vorticity field in the highly forced wake

The data presented point to a model of the development of the vorticity field in the forced, confined wake flow. Figure 4.17 shows a simplified schematic of this model. The spanwise vorticity at the splitter plate is shed into the free stream. This vorticity organizes itself into a predominately spanwise vortical field. Very close to the sidewall, the boundary layer slows the spanwise vortical tube and it begins to reorient itself into the streamwise direction. As the rollers of the spanwise vortical field convect downstream, the streamwise vorticity is stretched, causing the core radius to decrease and the peak vorticity to increase. It is believed that some of these small radius, high peak vorticity regions were not observed in the present measurement set as the size of the vortical region was reduced beyond the limits that could be measured in the current experiment. It is recognized that as the core continues to decrease in size, the spatial gradients will increase which will eventually increase the effect of diffusion.

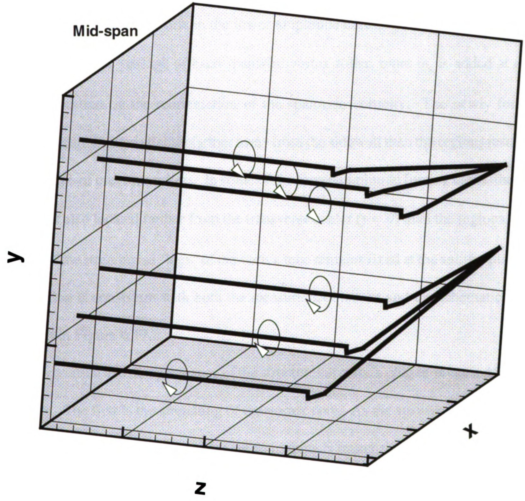

Figure 4.17: Diagram of the development of the vorticity field in the forced wake.

The streamwise vorticity field at each measurement location is the result of the reorientation of all of the spanwise rollers which have passed by that particular point in space. As will be described later, not all of these regions are separately distinguishable in the current data. As the measurement plane moves farther downstream more of these "legs" are observed. In the high amplitude forcing case, the location of these legs moves towards the center of the test section while in the lower amplitude cases, this motion is much less pronounced. With the passage of each spanwise vortex roller, more ω_x is added at each downstream location by the reorientation of the spanwise vorticity. The newly formed vortical regions are located slightly farther away from the sidewall than the regions resulting from the passage of previous rollers. In some of the lower amplitude forcing cases, the new region of ω_x is also located farther from the transverse center ($y = 0$) than the regions. Note that the end of the streamwise "legs" of the vortex tube remains fixed at the splitter plate tip. This description is consistent with both the measurement results and the schematic of the model shown in Figure 4.17.

The variation and disappearance of the structures at certain phases is caused by three broad effects. The first is the stretching of the vortex core. As the spanwise vortex rollers convect downstream, the streamwise legs are continuously stretched. This results in the core size decreasing and the peak vorticity increasing. The second reason for the variation in the magnitude of the peak vorticity is the lack of spatial resolution in the experimental measurements. Since the data density remains constant during the measurements, as the core radius shrinks, the effective L/δ decreases. The results presented in Appendix A show that as L/δ decreases, the bias error increases. This will result in a decrease in the measured value of the vorticity. As r_{core} continues to decrease because of the stretching, a point will be reached where the core radius is smaller than size which can be measured in the current experiment. Section 4.9 will also show that in upstream regions where the spacing between the regions of streamwise is small, the lack of spatial resolution results in multiple vortex cores having the appearance of a single core. The third reason for the variation in the $<\omega_x>$ structure is diffusion. As the regions of $<\omega_x>$ are stretched, the core radius will decrease and the peak vorticity will increase. This increase in spatial gradients will result in an increase in the effect of diffusion. However, it should be noted that diffusion is a slow acting process.

4.8 Evidence of axial flow along the cores of the spanwise vortices in the forced wake

As described in the introduction, core-wise axial flow has been found to exist along vortex cores in a large number of vortex dominated flows. One of the questions this study set out to answer was whether axial flow exists along the cores of the vortices in the forced wake. Figure 4.18 shows vector plot of the (v, w) velocities in the (y, z) plane at $x = 5.25\ cm$ for the phase corresponding to the passage of the negatively signed spanwise vortex core. When this core passes the $x = 5.25\ cm$ plane, a well-defined, jet-like flow can be seen moving from right to left at $y = 0\ cm$. The width of the core-wise jet is approximately $0.6\ cm$, which is approximately 60% of the spanwise vortex core diameter, and it is located near the vertical center of the test section where the spanwise cores are located for this forcing amplitude. The peak velocity within the core-wise jet is 15% of the free stream velocity. It is also approximately $^1/_3$ of the peak velocity of the jet of fluid resulting from the pair of counter-rotating streamwise vortex cores that develops in the cross-stream plane.

Due to its small size and velocity, it is believed that the axial flow does not play a primary role in the mixing increase in this flow. The amount of fluid transported by the

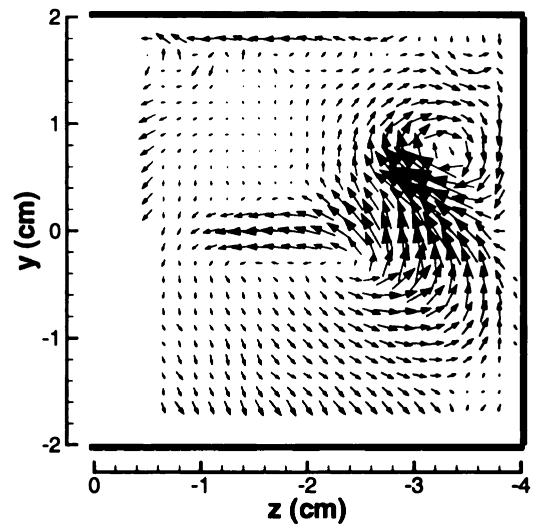

Figure 4.18: Axial flow in the A = *11.6%* wake at x = *5.25 cm.*

streamwise vortices is significantly more than that transported by the axial velocity. Furthermore, the fluid transported by this core-wise velocity is located within the vortex cores. Visualization and mixing results indicate that the fluid within each of the vortex cores is from only one of the two streams. Thus, the fluid transported by the core-wise flow will not come into contact with fluid from the other stream, and therefore, cannot mix..

4.9 Higher density measurements

The effect of spatial filtering on the $<\omega_x>$ field due to the measurement density was examined by means of a limited set of measurements conducted at twice the standard measurement density in each direction. Due to vortex stretching, the size of the streamwise vortical structures has been found to vary with the phase of the measurement. This results in a distribution of the non-dimensional measurement density, L/δ ranging from *2.5* to less than *1* in the standard density results. As the actual r_{core} decreases to smaller than the mean spacing between measurements, the vorticity will appear to be spread over a larger region

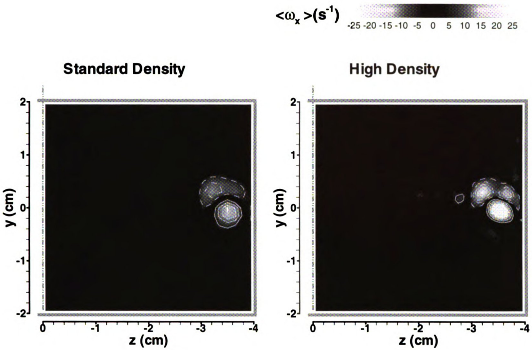

Figure 4.19: Comparison of the standard and high density measurements of the streamwise vorticity at $x = 3\ cm$. Contour lines indicate the $\pm 5\ s^{-1}$, $\pm 10\ s^{-1}$,..., $\pm 25\ s^{-1}$ with the dashed lines indicating the negative contour levels.

than it actually covers. If multiple cores are located within this region, they will appear as a single structure. If r_{core} is much smaller than the measurement density, the structure might not be detected at all. Doubling the resolution allows some of these features to be distinguished.

Figure 4.19 compares the high and standard measurement density data for the 11.6% forcing case at $x = 3\ cm$. This pair of images displays the effect of the increased spatial resolution. In the lower density measurements, a single negatively signed structure can be seen in the upper half-plane. However, the higher density measurement clearly shows two distinct negatively signed vortical structures. In the lower density measurement, the limited resolution resulted in the two structures appearing to be one. The appearance of the additional structures lends further credence to the model described in section 4.8 as it shows further evidence of multiple vortical structures decreasing in radius due to stretching.

As expected, the magnitude of the measured vorticity has also greatly increased with the increase in spatial measurement density. In the standard density results, $L/\delta = 1.5$. The peak measured vorticity level at this phase of the positively signed vortical structure is $20\ s^{-1}$. In the higher density measurements with $L/\delta = 3$, this value has doubled to $40\ s^{-1}$. From the results presented in Appendix A, the mean bias error for the high density results is approximately *5%*. Using this value, the vorticity values can be corrected to yield an actual estimated peak $<\omega_x> = 42\ s^{-1}$ for this phase. This value will be called the "corrected" peak vorticity. $L/\delta = 1.5$ was not examined in Appendix A, however, a bias error of a factor of two is not viewed as unreasonable given the very low measurement density.

When comparing the ratio of the peak levels of streamwise vorticity to the peak levels of spanwise vorticity, different normalized measurement densities can result in this quantity being reported incorrectly. As the physical size of the regions of streamwise vorticity is typically smaller than the spanwise vorticity, $\frac{<\omega_x>_{max}}{<\omega_z>_{max}}$ is likely to be under reported. Examining the downstream location $x = 4.25\ cm$, it is found that the corrected peak $<\omega_x> = 37\ s^{-1}$. At this location, the corrected peak $<\omega_x> = 44\ s^{-1}$, resulting in $\frac{<\omega_x>_{max}}{<\omega_z>_{max}} = 0.85$. Using the uncorrected values from the experimental results, this ratio is calculated to be only *0.65*. As the streamwise vortex core stretches, its peak vorticity will increase and its core radius will decrease. As the core radius decreases however, the peak vorticity levels will be underestimated by a larger fraction. It is believed that this effect results in the peak levels of streamwise vorticity reported in this series of experiments to be underestimated even after they have been corrected because as the core radius shrinks to less than the mean spacing between points, the structures will not be detected. It is at these small radii where the peak levels of $<\omega_x>$ will be found.

The true value of $\frac{<\omega_x>_{max}}{<\omega_z>_{max}}$ for this flow could be greater than or equal to *1*. As was shown in the previous sections, the streamwise vorticity is primarily formed by the reorientation of the spanwise vorticity. Since the total circulation cannot change within the vortex tube, the streamwise legs must have the same circulation as the spanwise vortex roller. Thus, in the absence of effects which tend to reduce vorticity levels, such as diffusion which has a relatively long time scale, as the "leg" is stretched, its peak levels $<\omega_x>$ could increase to levels larger than the peak levels of $<\omega_z>$.

Chapter 5

Measurements at the 4 Hz and 8 Hz Forcing Frequencies

This section will discuss the results of measurements made for the 4 Hz and 8 Hz forcing frequencies. These frequencies have been selected as flow visualization results indicate that the general structure of the flow observed at these frequencies is similar to that seen at 6 Hz. Note that the range of measurements in this study is significantly smaller than that of Roberts (1985). Although there are many similarities between these sets of measurements and the 6 Hz results presented in the previous two chapters, some interesting differences are found. Unfortunately, as of present, no molecular mixing studies have been conducted in the experimental facility at these frequencies, so the velocity and vorticity fields cannot be compared to mixing field data.

5.1 Mean streamwise measurement plane flow properties at center span

Figures 5.1 and 5.2 show the mean velocity fields at three downstream locations for the 4 Hz and 8 Hz forcing conditions respectively. These are quite similar to the patterns seen in the 6 Hz case. In the 4 Hz case, however, the free stream region, especially on the top side of the test section, is very thin in comparison to the unforced results. This makes it to determine the value to be used for the free stream velocity as there is no region where the streamwise velocity is constant.

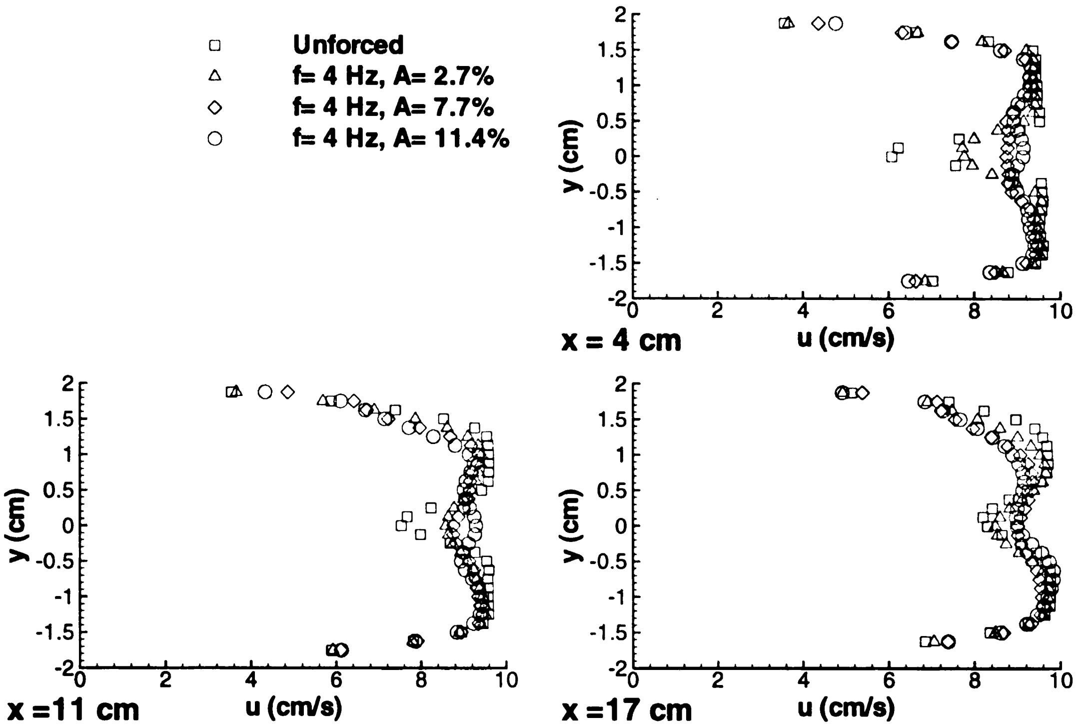

Figure 5.1: Mean velocity profiles for the wake forced at 4 Hz at three streamwise locations.

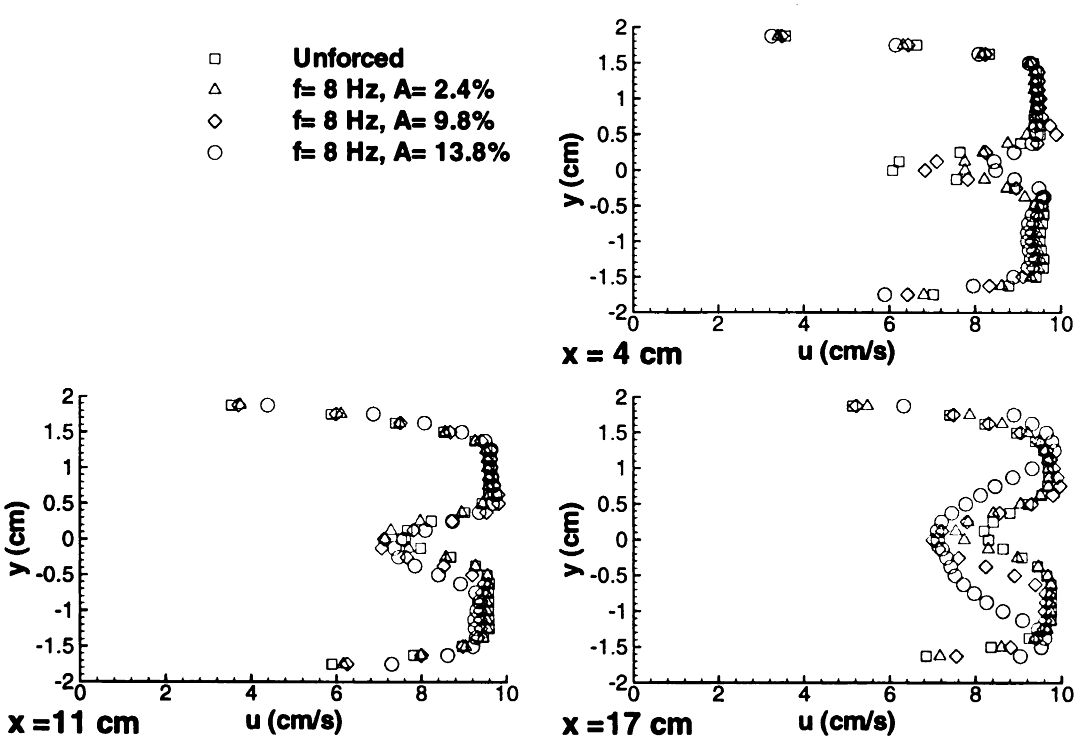

Figure 5.2: Mean velocity profiles for the wake forced at 8 Hz at three streamwise locations.

In the 4 Hz forcing cases, the peak velocity deficit of the wake, measured by the difference between the free-stream velocity and the minimum velocity of the wake, always decreases when forcing is applied. An increase in the forcing amplitude usually corresponds to a decrease in the velocity deficit. However, at $x = 11\ cm$ and $x = 17\ cm$, the deficit is constant for all three forcing amplitudes.

Similar trends are seen in the 8 Hz forcing results. As would be expected, at $x = 4\ cm$, the minimum deficit occurs for $A = 13.8\%$, the largest of the three forcing amplitudes. However, the largest deficit is found for the middle *9.8%* forcing level, not in the smallest amplitude results as was found in the 4 Hz and 6 Hz results. For $x = 11\ cm$, the wake deficit of all of the forced cases as well as the unforced are nearly identical. At $x = 17\ cm$, the deficit of the three forcing cases remains approximately the same, however, the deficit of the unforced case is lower than that of the forced cases. Between these two streamwise locations, the width of the wake, measured as the distance from the free-stream region on the bottom and top surface of the wake differs dramatically. Since the wake deficit for the different cases is similar, this measure of the wake width can be easily seen in Figures 5.2. At $x = 11\ cm$, the width of the wakes for the different forcing amplitudes and the unforced case are nearly identical. By $x = 17\ cm$, it can be seen the velocity deficits the three forcing cases varies dramatically. This is especially noticeable in the high amplitude case where the wake occupies nearly the entire width of the test section. A similar effect was seen in the 6 Hz forcing results for the $A = 11.6\%$ forcing amplitude. The *2.7%* forcing amplitude has the narrowest wake and the *13.8%* is in between.

Figure 5.3 shows the effect of the 4 Hz and 8 Hz forcing on the momentum thickness at center span. In Chapter 3, it was discussed how this quantity could be related to the drag.

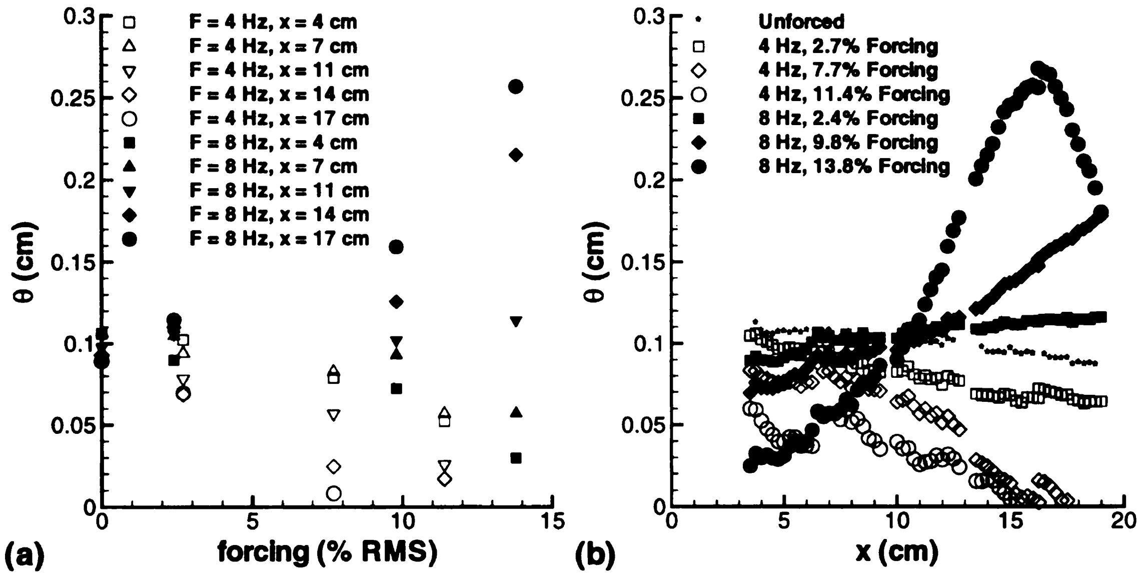

Figure 5.3: Effect of forcing on the momentum thickness across the 4 Hz and 8 Hz forcing frequencies. (a) Effect of forcing amplitude on θ at constant streamwise location. (b) Effect of streamwise location on θ at constant forcing conditions.

The dependence of θ on the forcing amplitude is shown in Figure 5.3a. For the 4 Hz forcing results, θ decreases slightly from the unforced value of *0.1 cm* with increased application of forcing. For the 8 Hz results, as in the 6 Hz, at $x = 4$ *cm* and $x = 7$ *cm*, the momentum thickness decreases as forcing increases. For the locations farther downstream, θ increases with forcing amplitude.

Figure 5.3b shows the downstream development of θ for the 4 Hz and 8 Hz frequencies. For the 4 Hz cases, θ decreases with downstream distance. This is likely an artifact of the value used for the free-stream velocity. As in Chapter 3, the value of u_0 used in the calculation of the momentum thickness is estimated from the average of the upper and lower free stream velocities at the x location where θ is computed. As the measurement moves downstream into regions where no free stream value can be found, such as at $x = 17$ *cm* for the 4 Hz cases, the value of u_0 tends to be overestimated due to the growth of the top and bottom boundary layers.

For the 8 Hz forcing cases, an increase in θ is apparent at all forcing amplitudes. The $A = 2.7\%$ forcing shows a very slight increase. For $A = 9.8\%$, θ triples as x increases from 4 cm to 20 cm. The momentum thickness for the 13.8% forcing case starts out very small and then rapidly increases by more than factor of *10* (from *0.02 cm* at $x = 3$ *cm* to *0.28* at $x = 15$ *cm*). This is very similar to the $F = 6$ *Hz*, $A = 11.6\%$ case. However, for $x > 16$ *cm*, θ begins to decrease in the $F = 8$ *Hz*, $A = 13.8\%$ results, which was not seen in the θ results for $F = 6$ *Hz*, $A = 11.6\%$. However, at the location of the maximum value of θ in the $F = 8$ *Hz*, $A = 13.8\%$, $x = 15$ *cm*, the *8 Hz* results have traveled through *13* forcing cycles whereas the *6 Hz* results have only traveled through *9.5* forcing cycles at this downstream location. Thus, a maximum on θ for the *6 Hz* results may exist at $x = 25$ *cm*, which is *13* forcing cycles downstream for this forcing frequency.

In the results for the 6 Hz forcing described in Chapter 3, a spatial periodicity was noted in the u_{rms} field. This same periodicity is seen in the example of the u_{rms} of the 4 Hz and 8 Hz cases in Figure 5.4a and 5.4b respectively. For both forcing frequencies, a spatial periodicity with a wavelength equal to the forcing wavelength is seen. Although only the highest measured amplitude results are shown, the effect is also seen in the lower amplitude forcing results for these frequencies however with a reduced magnitude. The v velocity RMS for these same two forcing cases is shown in Figure 5.4c and 5.4d. Generally, a pattern with the largest RMS values in the middle of the layer and the values decrease moving towards the top and bottom of the facility. However, in the $F = 8$ *Hz*, $A = 13.8\%$ the pattern begins to split apart similar to what will be seen for the $\overline{\omega}_z$ later in this section and for $<\omega_z>$ in section 5.2.

Examining the 4 Hz results, it can be seen that the region of spatial periodicity

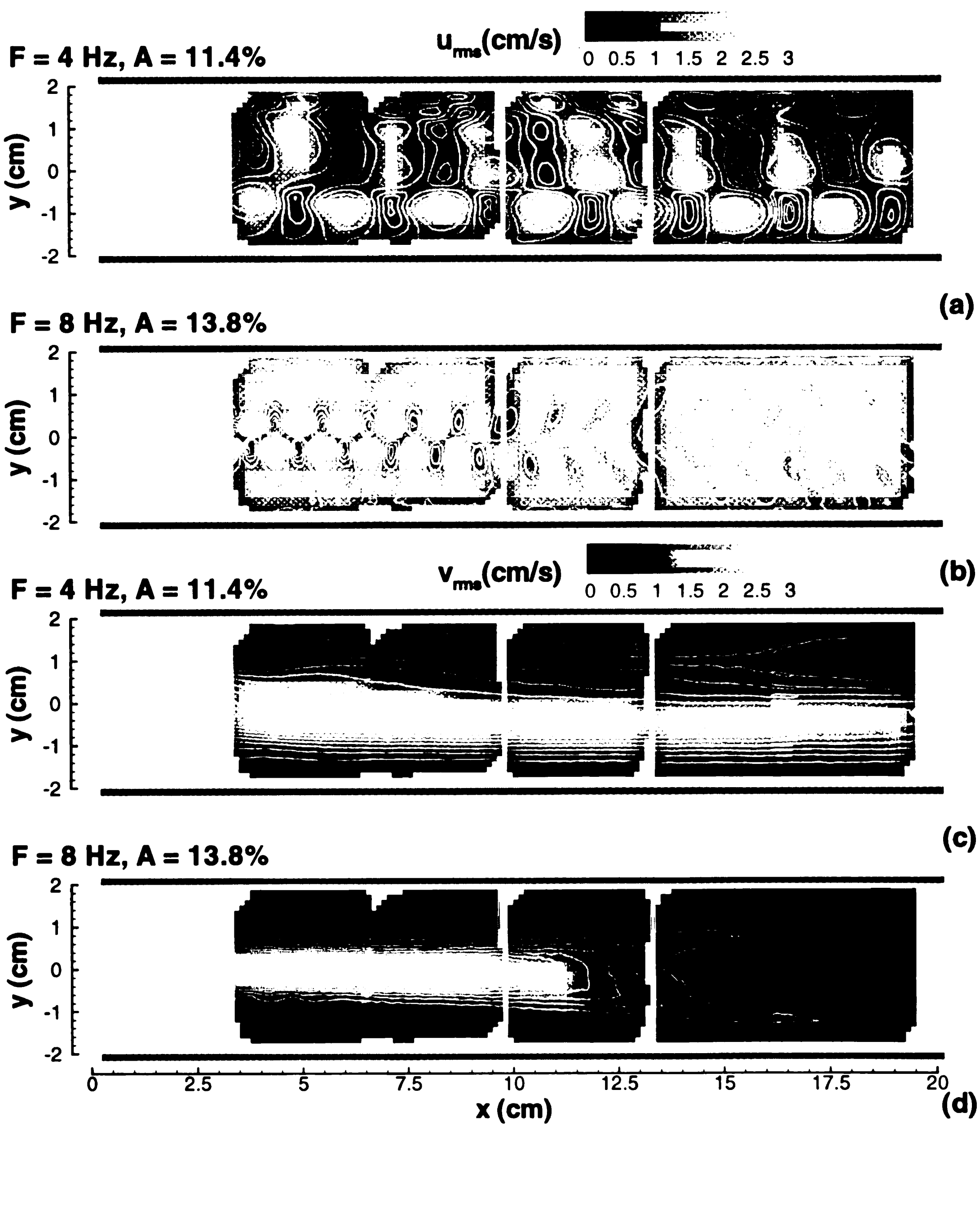

Figure 5.4: RMS of streamwise (u) velocity and transverse (v) velocity for the highest amplitude cases of the 4 Hz and 8 Hz forcing. The contour lines start at *0.2 cm/s* and spaced every *0.2 cm/s*. (a) u_{rms} for F = 4 Hz, A = 11.4%. (b) u_{rms} for F = 8 Hz, A = 13.8%. (c) v_{rms} for F = 4 Hz, A = 11.4%. (c) v_{rms} for F = 8 Hz, A = 13.8%.

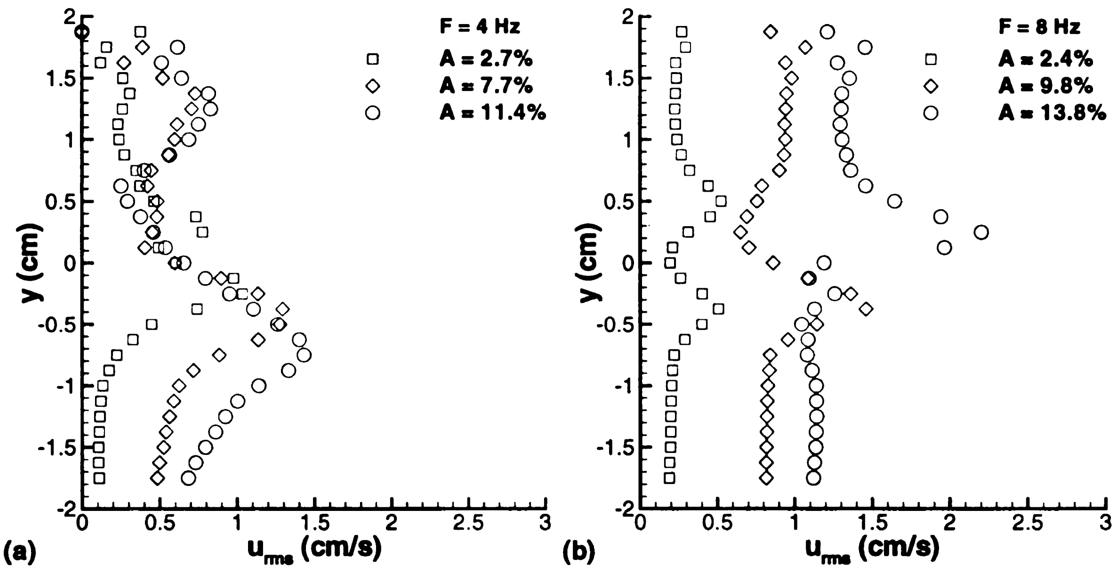

Figure 5.5: RMS of streamwise velocity vs y location at x = *4 cm*. (a) 4 Hz forcing. (b) 8 Hz forcing.

reaches nearly to the wall of the test section. For this forcing case, no region of a uniform value for the u_{rms} can be seen at any downstream location. This is also apparent in line plots of the u_{rms}, an example of which is seen in Figure 5.5. For the two higher forcing amplitude of the 4 Hz results in Figure 5.5a, no uniform region of u_{rms} is found with transverse location. It is therefore not possible to measure an exact, constant value for the free-stream fluctuation levels as the value of the u_{rms} is always changing. For this reason, it was noted in Chapter 2 that the forcing levels listed for the 4 Hz forcing frequency are used only for labeling the different cases. For the 8 Hz results displayed in Figure 5.5b, a steady region of u_{rms} is seen. This was also seen in the 6 Hz results discussed in Chapter 3.

Figures 5.6 and 5.7 show the mean vorticity field for three measured forcing amplitudes for the 4 Hz and 8 Hz forcing frequencies as well as the unforced measurement results. For the 4 Hz forcing results, a region of nonzero $\overline{\omega}_z$ is seen in the lowest forcing amplitude at early x locations. As will be seen in section 5.3, this is the region where the

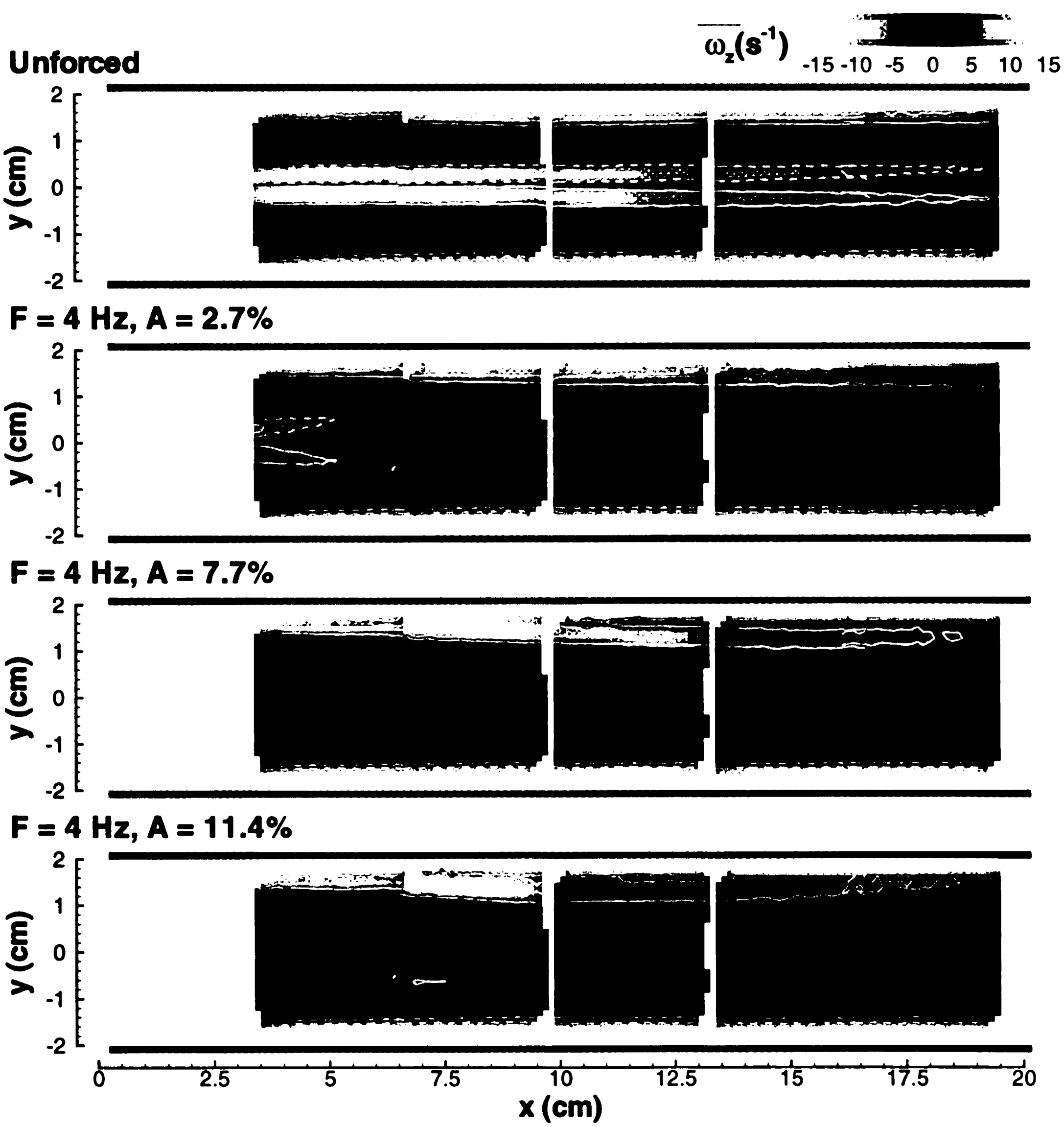

Figure 5.6: Mean streamwise vorticity for unforced case and three different amplitudes for the 4 Hz forcing. The contour lines indicate the ±*3*, ±*6*, ..., ±*15* s^{-1} contour lines with the dashed lines indicating the negative values.

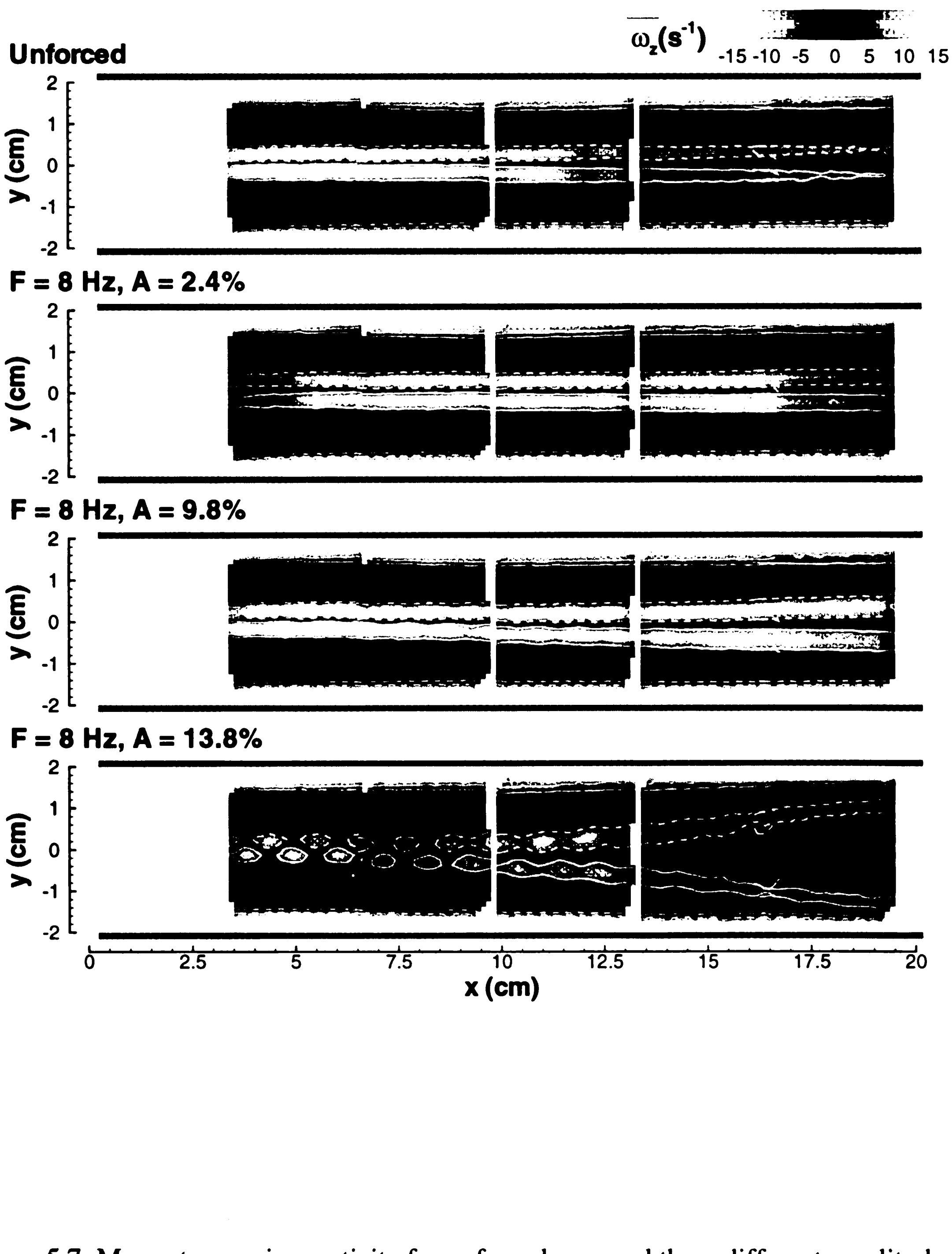

Figure 5.7: Mean streamwise vorticity for unforced case and three different amplitudes for the 8 Hz forcing. The contour lines indicate the ± 3, ± 6, ..., ± 15 s^{-1}contour lines with the dashed lines indicating the negative values.

vorticity shed from the splitter plate is forming into the gaussian shaped spanwise vortex tubes. In the higher forcing amplitudes, $\overline{\omega}_z$ is nearly zero in the wake region. This is very different from what was seen in the 6 Hz forcing amplitude results in which regions of mean vorticity were seen in the all but the highest forcing amplitude.

The $\overline{\omega}_z$ field for the 8 Hz forcing results is very similar to the mean field for the 6 Hz forcing. Two regions of non-zero $\overline{\omega}_z$ are seen for the 2.4% and 9.8% forcing amplitudes, a negative region in the top half-plane and a positive region in the bottom half-plane. For the 13.8% forcing amplitude, two regions of mean vorticity are seen again. However, these regions split apart with the negative mean vorticity moving towards the top wall of the test section while the positive region moves towards the bottom of the test section. A similar effect was previously seen in the v_{rms} field. This splitting apart of the mean vorticity field was not seen in the 6 Hz forcing results. In the 6 Hz forcing frequency results, isolated regions of mean vorticity were seen. In Chapter 3, this was explained by the variation of the convection speed of the spanwise vortex rollers. This same effect is also seen in the 8 Hz forcing results.

In Chapter 3, the mean field of $\overline{\frac{\partial w}{\partial z}}$ at $z = 0\ cm$ was seen to be a good predictor of the x location where molecular mixing field begins the increase dramatically for the 6 Hz forcing. Figures 5.8 and 5.9 display the $\overline{\frac{\partial w}{\partial z}}$ field for the 4 Hz and 8 Hz forcing frequencies. No region of increased $\overline{\frac{\partial w}{\partial z}}$ is seen in the 4 Hz forcing results. However, a wedge-shaped region of strong negative $\overline{\frac{\partial w}{\partial z}}$ is seen in the highest amplitude 8 Hz forcing results. In section 5.3, it will be shown that the strong recirculatory flow pattern found in the $F = 6\ Hz$, $A = 11.6\%$ case is also found for this forcing case. It is believed that this will indicate a rapid increase in the amount of mixed fluid. Without molecular mixing results, however,

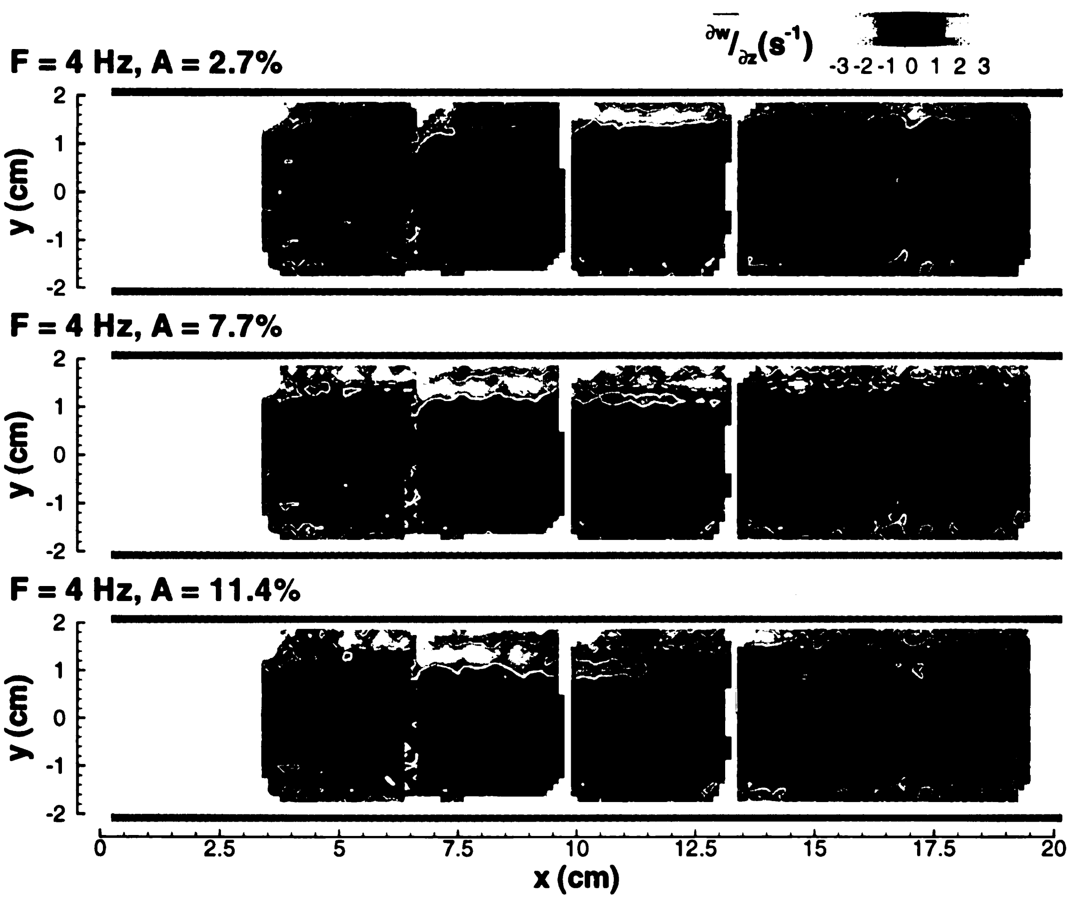

Figure 5.8: Mean $\overline{\frac{\partial w}{\partial z}}$ field for 4 Hz forcing at three perturbation amplitudes. The contour lines indicate regions of positive and negative sign.

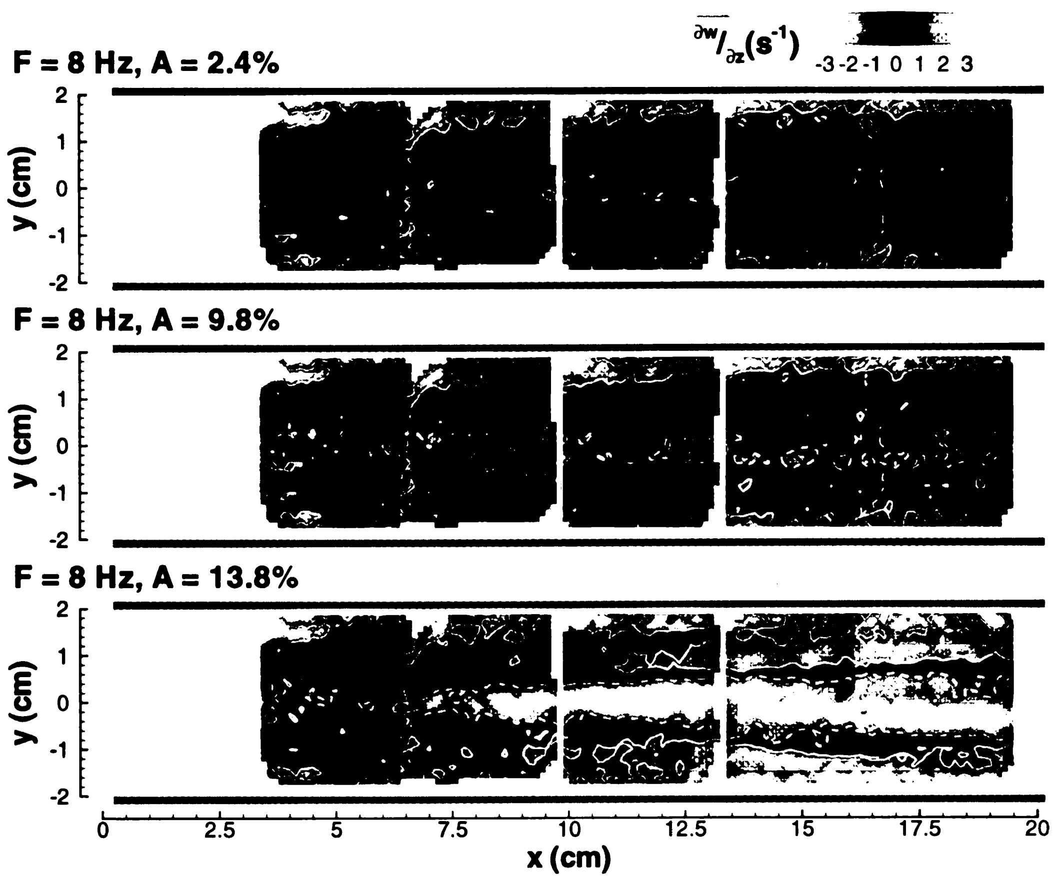

Figure 5.9: Mean $\overline{\frac{\partial w}{\partial z}}$ field for 8 Hz forcing at three perturbation amplitudes. The contour lines indicate regions of positive and negative sign.

this cannot be confirmed.

5.2 Phase-averaged streamwise measurement plane results at center-span

In Figure 5.10, a sample of the instantaneous vorticity field for the unforced case as well as the phase-averaged vorticity field for the three 4 Hz forcing frequencies cases. In the upstream region of the $F = 4\ Hz,\ A = 2.7\%$ case, the process of the vortices forming into well-defined, circular cores can be seen. Initially, the vorticity is continuously shed from the splitter plate. As the vorticity convects downstream, the elongated, isolated regions of $<\omega_z>$ form. In addition to convecting downstream, it is apparent from animations of the data that the elongated regions are also rotating about their center. As these regions rotate and convect downstream, the cores become circular in shape and take on the Gaussian vorticity profile. This is close to the classic picture of the formation of vortex cores.

In the $F = 4\ Hz,\ A = 7.7\%$ results, the vortex street is nearly vertically aligned. This alignment was seen in the $F = 6\ Hz,\ A = 11.6\%$ forcing case which was one of the high mixing cases. This case, however, does not exhibit any of the other characteristics found in the high mixing case such as a region of negative $\overline{\frac{\partial w}{\partial z}}$,a mean recirculatory pattern in the cross-stream plane velocity field and regions of streamwise vorticity moving towards the spanwise center of the test-section. As previously stated, no mixing results exist for this forcing condition so it is not possible to confirm that this case will not result in increased molecular mixing.

In the highest amplitude forcing case for the 4 Hz forcing case, the vortex cores shed from the splitter plate exhibit a splitting type process. At each downstream location where

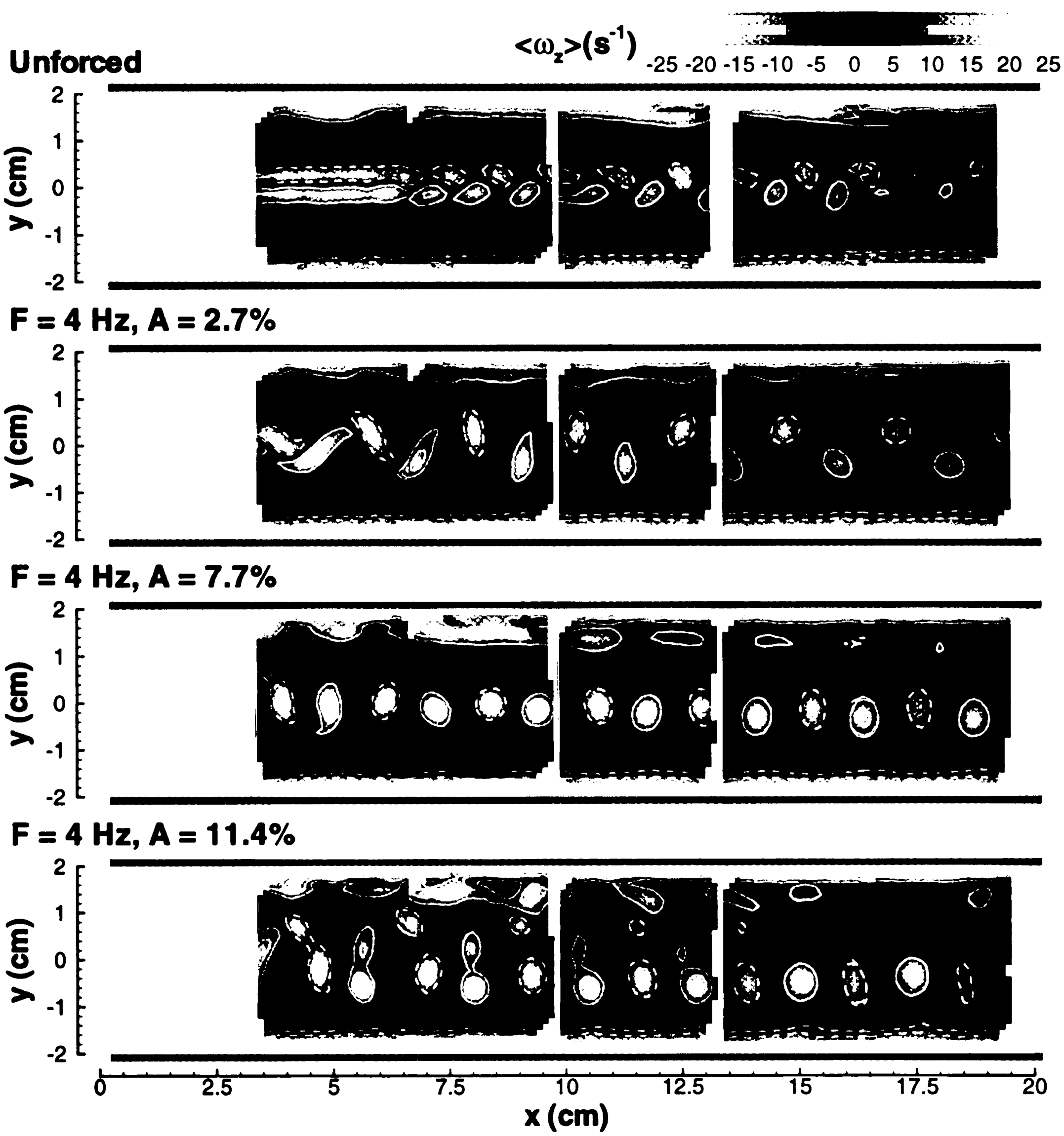

Figure 5.10: Phase-averaged streamwise vorticity for unforced case and three different amplitudes for the 4 Hz forcing. The contour lines indicate the ±*5*, ±*10*, ..., ±*25* s^{-1}contour lines with the dashed lines indicating the negative values.

$<\omega_z>$ is present, two vertically aligned vortex cores of the same sign are seen. For $x < 8\ cm$, these regions are connected. As the cores convect downstream, the splitting process completes and two separate cores can be.

Along the top wall of the facility, a second region of vorticity is being shed from the top wall boundary layer. Although this second shedding region is most apparent in the 11.4% forcing, it can be seen in the 7.7% forcing results as well. A similar effect is not seen on the bottom boundary layer. These shed vortices are not observed in the 6 Hz or 8 Hz forcing cases. It is believed that the 4 Hz forcing is exciting a disturbance in the surface of the top wall which is then shedding vorticity. This disturbance is not excited in the other two forcing frequencies studied.

Figure 5.11 displays the phase-averaged 8 Hz forcing frequency results. Although the peak vorticity magnitudes of the *2.1%* and *9.8%* forcing amplitudes are differ significantly, the spacing between these two cases is nearly identical for all streamwise locations. In the *13.8%* forcing results, the peak values of $<\omega_z>$ in the vortex array are larger yet. In this case, however, the transverse separation between the vortex cores increases dramatically. For $x > 12.5\ cm$, the negatively signed $<\omega_z>$ moves towards the top wall while the positively signed $<\omega_z>$ moves towards the bottom wall. This pattern is similar to what was seen for the $F = 6\ Hz$, $A = 11.6\%$ case, however the effect is greatly enhanced in the high amplitude 8 Hz forcing case.

Figure 5.12a shows the effect of the 8 Hz forcing amplitude on the peak levels of ω_z as the vortex tube convects downstream. For all three forcing amplitudes, the vorticity levels are the largest at the locations farthest upstream, but then decreases. At $x = 4\ cm$, the peak levels of ω_z range from $20\ s^{-1}$ for to 2.4% forcing amplitude to $40\ s^{-1}$ for the 13.8% forcing

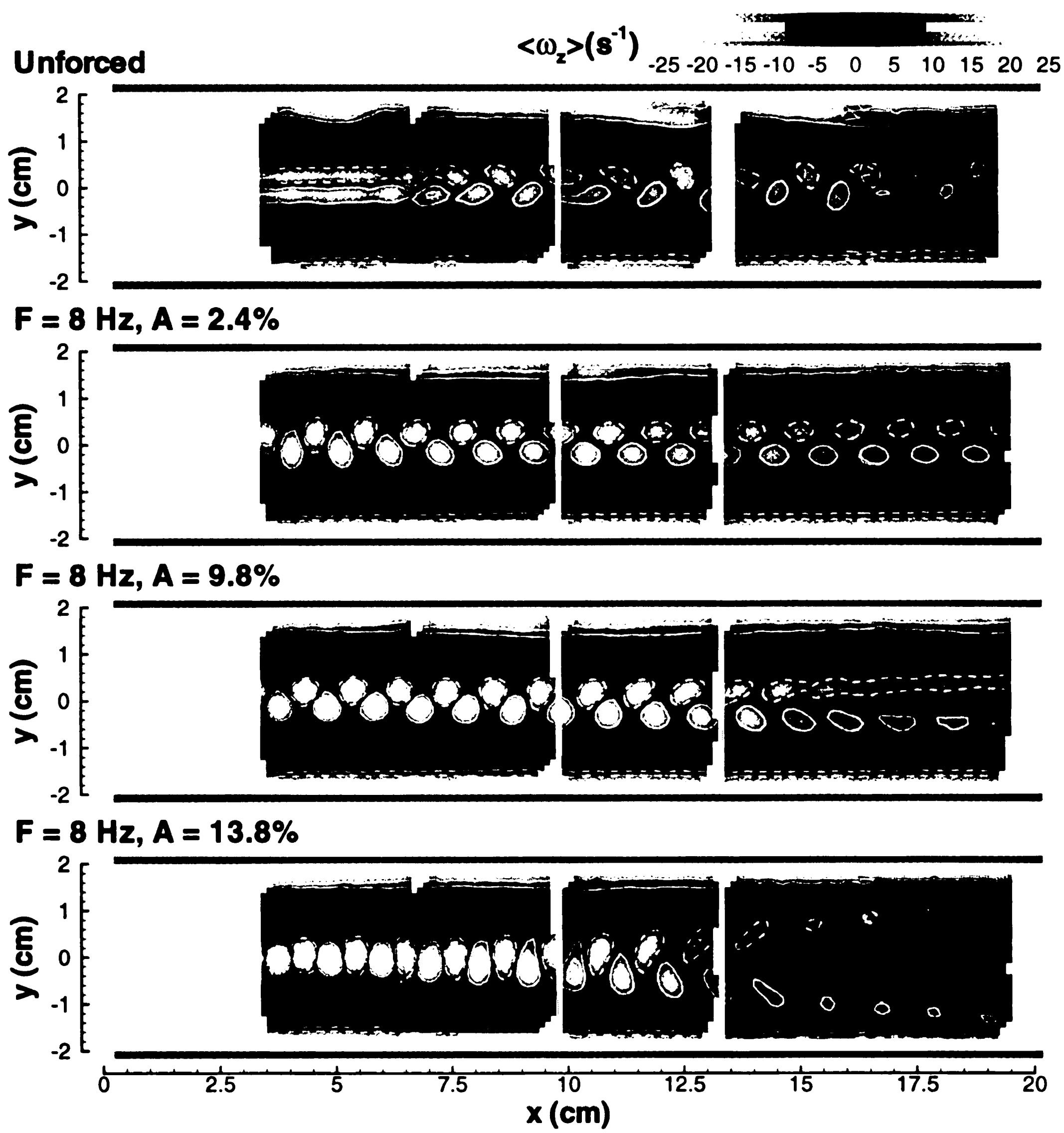

Figure 5.11: Phase-averaged streamwise vorticity for unforced case and three different amplitudes for the 8 Hz forcing. The contour lines indicate the ±*5*, ±*10*, ..., ±*25* s^{-1}contour lines with the dashed lines indicating the negative values.

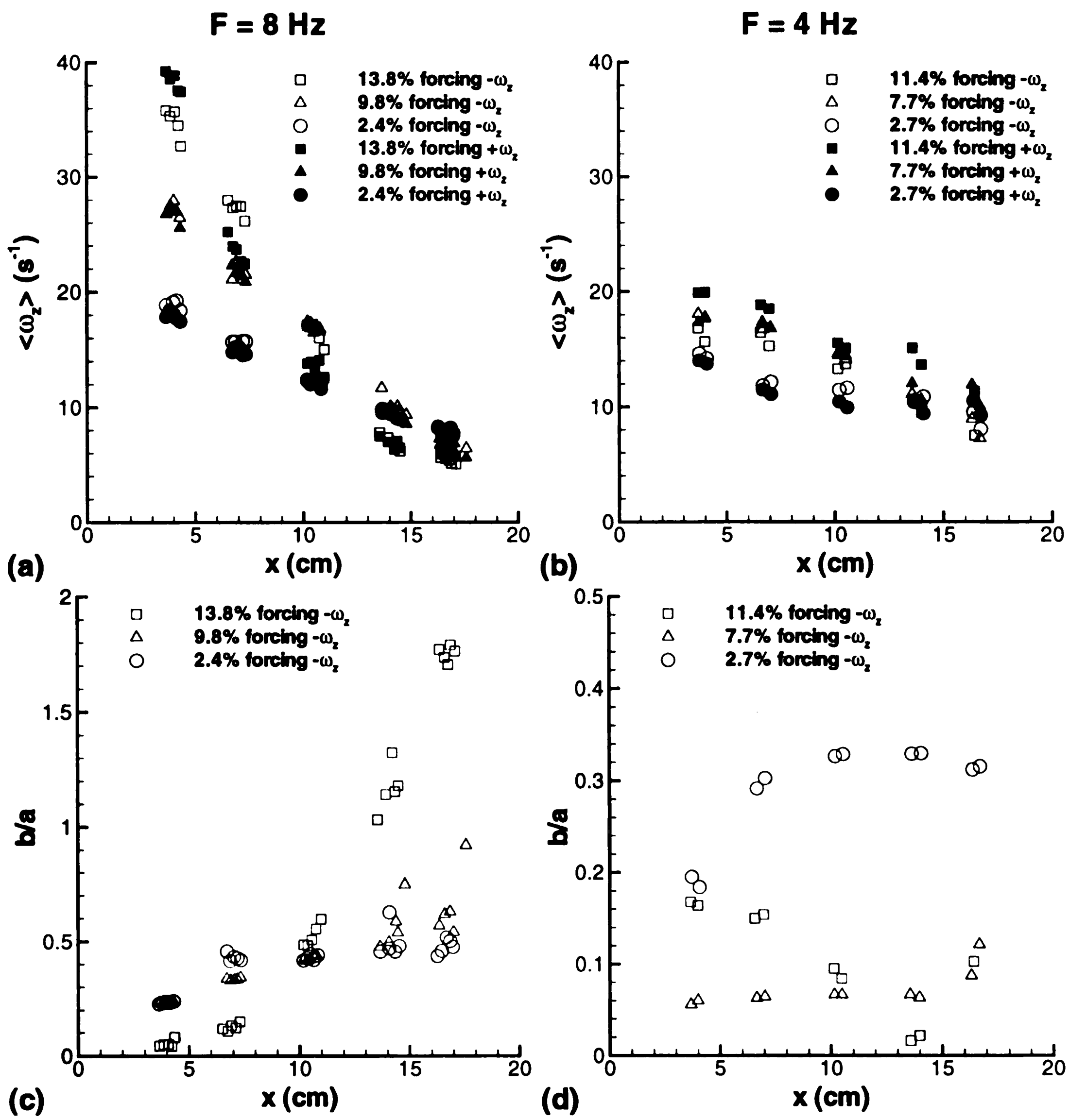

Figure 5.12: Effect of downstream location on peak $<\omega_z>$ and spacing ratio. (a) Peak vorticity for 8 Hz forcing. (b) Peak vorticity for 4 Hz forcing. (c) *b/a* for 8 Hz forcing. (d) *b/a* for 4 Hz forcing. Note that the scale in (c) and (d) are not the same.

amplitude. The decay rate of the vortices is significantly different and at $x = 17.5\ cm$, $\omega_z = 6\ s^{-1}$ for all three forcing amplitudes. This rate of decay of the peak $<\omega_z>$ is slightly faster than that observed with the 6 Hz forcing amplitude. This is likely the result of the larger values of $\overline{\frac{\partial w}{\partial z}}$ found in the 8 Hz forcing frequency results.

The behavior of the peak $<\omega_z>$ for the 4 Hz cases, seen in Figure 5.11d, is significantly different than that of the 6 Hz or 8 Hz forcing. Unlike the 6 Hz and 8 Hz cases, the magnitude of the peak $<\omega_z>$ only increases by 50% with increases in the forcing amplitude. In the 6 Hz and 8 Hz cases, increasing the forcing amplitude results in the peak $<\omega_z>$ increasing by over a factor of two. The vorticity levels of the 4 Hz forcing cases are also significantly lower than in the other cases. The highest forcing amplitude for the 4 Hz cases has a maximum $<\omega_z> = 20\ s^{-1}$. This value is approximately the same as the peak values seen for $A = 2.4\%$ for the 8 Hz case and $A = 2.1\%$ for the 6 Hz forcing. As the vortices convect downstream, the decay of the peak $<\omega_z>$ for the 4 Hz forcing amplitude is significantly less than that of the other two forcing frequencies. In the range $3\ cm < x < 20\ cm$, the peak $<\omega_z>$ only drops by a factor of two for all forcing amplitudes. This is again similar to the low amplitude results of the other two forcing frequencies. It is worthwhile to noted that the value of $\overline{\frac{\partial w}{\partial z}}$ which causes the majority of the decrease in peak $<\omega_z>$ values, measured for the 4 Hz forcing frequency is also of the same order as that of the low amplitude forcing results for the 6 Hz and 8 Hz cases.

The non-dimensional spacing between the vortices, *b/a*, for the 8 Hz and 4 Hz forcing is found in Figures 5.2c and 5.2d respectively. Note that the scale on the two plots is different because of the large differences in *b/a* between these two cases. For the 8 Hz forcing, the highest amplitude forcing initially has a value very close to zero. This indicates the near alignment seen in Figure 5.11. As the flow convects downstream, it increases to a value of nearly two. At locations far downstream, the *b/a* quantity may be misleading since the two-dimensional rollers likely do not exist at these downstream location. This is approximately double the maximum value seen in the 6 Hz forcing results. This dramatic increase in spacing is clearly seen in Figure 5.11 where the positive and negative vortices split apart with the negatively signed rollers moving towards the top of the test section and the positively signed rollers moving towards the bottom of the section. The two lower forcing amplitude cases for 8 Hz forcing also show an increase, however it is not nearly as large as seen in the $A = 13.8\%$ results.

In both the 6 Hz and 8 Hz forcing data, the high amplitude forcing results show a large increase in spacing with x. For the 4 Hz case shown in Figure 5.11d, however, the spacing ratio remains relatively constant for the higher amplitude results. An increase in *b/a* is only observed in the lowest amplitude forcing results where *b/a* increases from *0.2* to *0.32* between $x = 4\ cm$ and $x = 11\ cm$. The ratio remains constant for $x > 11\ cm$. It is believed that the small values seen for $x < 11\ cm$ is due to the formation process of the vortex core. From Figure 5.10, it appears that the vortex cores are still in the process of evolving into the tightly wound core. Since the regions of vorticity are initially shed from the splitter plate, they are closer together then in the fully formed vortex street.

5.3 Mean streamwise vorticity and cross-stream plane velocity results

Figure 5.13 shows the development of the $\overline{\omega_x}$ field for three forcing amplitudes of the 4 Hz forcing frequency. For the lowest amplitude, no streamwise vorticity can be seen

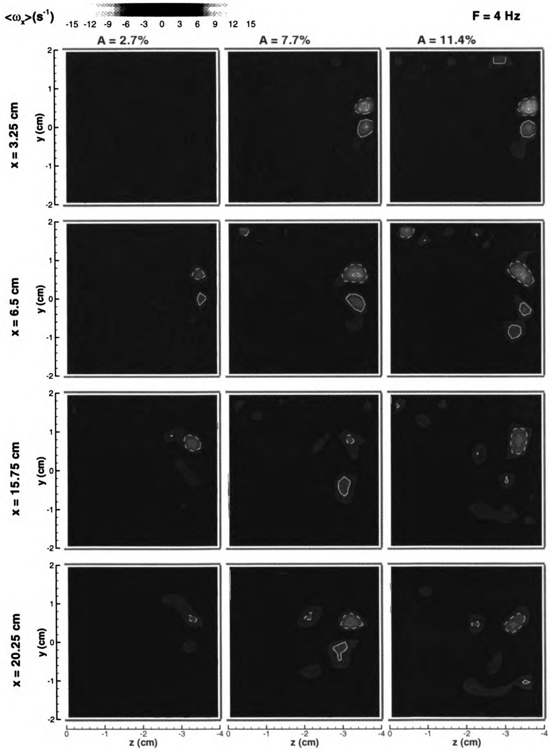

Figure 5.13: Mean ω_x at 4 streamwise locations for the 4 Hz forcing frequency cases. The contour lines indicate the $\pm 3, \pm 6, \ldots, \pm 15$ s^{-1}contour lines with the dashed lines indicating the negative values.

at the farthest upstream location. As the flow develops downstream, regions of $\overline{\omega_x}$ can be seen at $x = 6.5\ cm$. As the measurement plane moves further downstream, both the peak magnitude of the $\overline{\omega_x}$ as well as the size of the region where vortical structures are found decreases. For $A = 7.7\%$ and $A = 11.4\%$ two counter-rotating regions of $\overline{\omega_x}$ are seen at the farthest upstream location. As the flow develops downstream, these regions show a small increase in the value of peak vorticity, reaching a maximum at $x = 6.5\ cm$. Further downstream, the peak magnitude of these regions begins to decrease. Multiple regions of $\overline{\omega_x}$ are seen at the farthest downstream locations. However, these regions remain close to the sidewall.

The development of the $\overline{\omega_x}$ field for the 8 Hz forcing seen in Figure 5.14 is very similar to the 6 Hz forcing results. For $A = 2.4\%$ and $A = 9.8\%$, the counter-rotating streamwise vortex pair is present. The downstream development of these cases is similar to the $F = 6\ Hz$, $A = 7.3\%$ results. As the measurement plane moves downstream, these regions weaken and they remain relatively close to the wall. For $A = 13.8\%$, the counter-rotating pair of mean $\overline{\omega_x}$ splits into multiple regions at farther downstream locations. As the measurement plane moves farther downstream, the regions of mean streamwise vorticity moves towards the center of the test section. This is similar to what was seen in the high mixing case of $F = 6\ Hz$, $A = 11.6\%$.

The cross-stream plane velocity field (v-w velocities in the y-z plane), for the 8 Hz case, shown in Figure 5.15, also displays characteristics similar to the 6 Hz forcing. For the $A = 13.8\%$ forcing, a mean recirculatory pattern is seen at $x > 6.5\ cm$. This is again reminiscent of the results seen in the cases which have shown a large amount of mixed fluid. The lower forcing amplitude results do not show the presence of the mean recirculatory

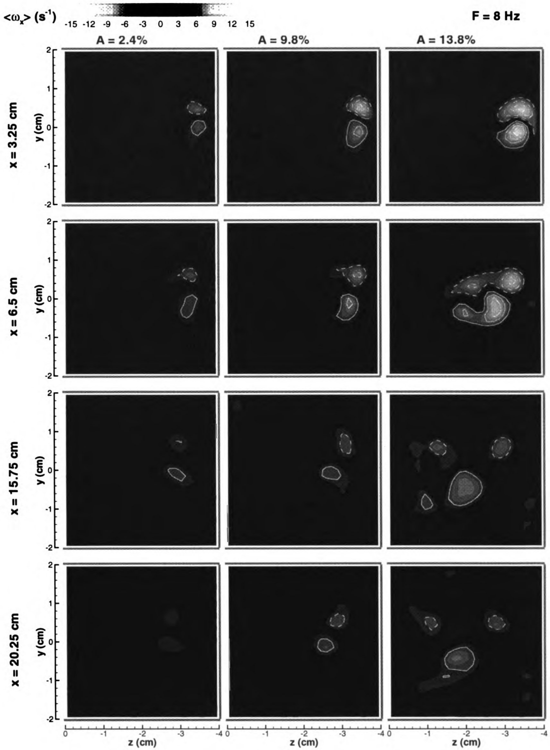

Figure 5.14: Mean ω_x at 4 streamwise locations for the 8 Hz forcing frequency cases. The contour lines indicate the ± 3, ± 6, ..., ± 15 s^{-1}contour lines with the dashed lines indicating the negative values.

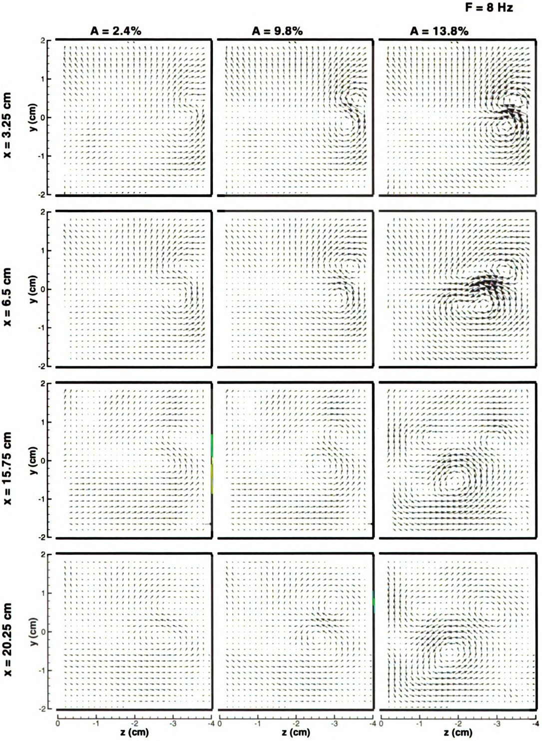

Figure 5.15: Mean v-w velocities in the y-z plane at *4* streamwise locations for the 8 Hz forcing frequency cases.

pattern. The mean cross-stream plane velocity field for the 4 Hz forcing (not shown here) does not display the recirculatory pattern at any of the forcing amplitudes.

5.4 Phase averaged streamwise vorticity and cross-stream plane velocity results

As with the 6 Hz forcing results, the streamwise vorticity field for the 4 Hz and 8 Hz forcing cases display a variation with phase. Figure 5.16 shows the variation of the *8 Hz, A = 13.8%* forcing case with phase at $x = 3.25\ cm$. As the flow moves through the forcing cycle, a variation between the peak of the positively signed streamwise vortex tube and the negatively signed vortex tube is seen as the flow convects past the measurement location. At $x = 20.25\ cm$, shown in Figure 5.17, the regions of streamwise vorticity have moved towards the center of the test section and nearly the entire test section is occupied with regions of streamwise vorticity. For the low amplitude, 8 Hz forcing cases and all of the 4 Hz cases, this inward movement is not seen.

Based on the data presented, it is believed that the $F = 8\ Hz$, $A = 13.8\%$ case will exhibit enhanced mixing seen in the $F = 6\ Hz$, $A = 11.6\%$ case. It displays the characteristics seen in this known, high mixing case such as region of negative $\overline{\frac{\partial w}{\partial z}}$, a recirculatory flow pattern in the cross-stream plane, and regions of $\langle\omega_x\rangle$ moving quickly towards center span. None of the other 4 Hz and 8 Hz measurement exhibit these features. It will be interesting to see if mixing studies will confirm this hypothesis.

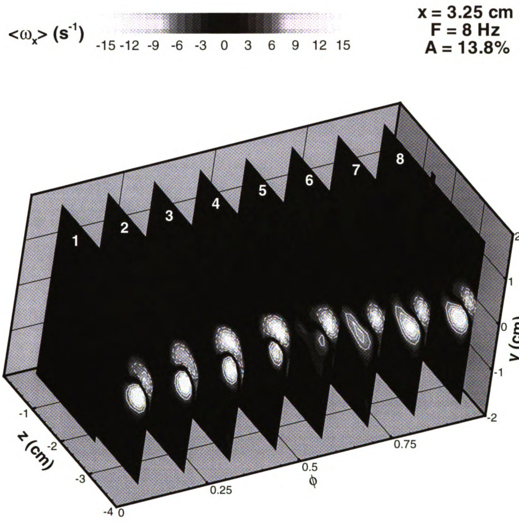

Figure 5.16: Variation of phase-averaged ω_x with phase for $F = 8\ Hz$, $A = 13.8\%$ at $x = 3.25$ cm. The contour lines indicate the ± 6, ± 9, ..., ± 15 s^{-1}contour lines with the dashed lines indicating the negative values.

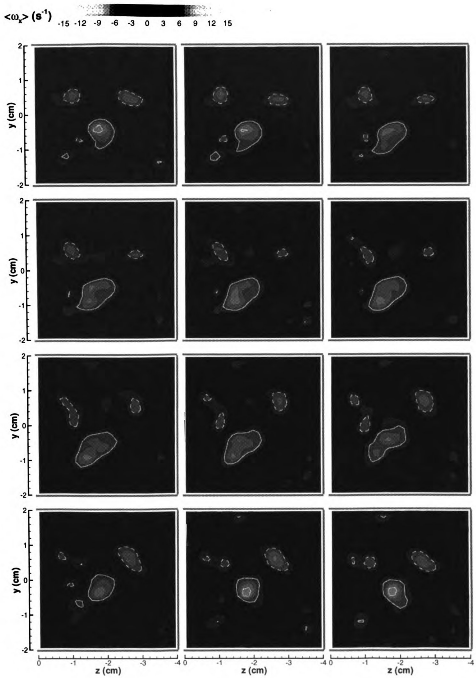

Figure 5.17: Variation of $<\omega_x>$ with phase for *F = 8 Hz*, *A = 13.8%* at *x = 20.25 cm*. The displayed phases are separated by approximately $\Delta\phi = 0.08$ and phase runs from right to left and then top to bottom. Contour lines indicate the ± 3, ± 6, ..., ± 15 s^{-1}contour lines with the dashed lines indicating the negative values.

Chapter 6

Conclusions

Velocity and vorticity field measurements were made in a forced, confined wake in order to both better understand the vorticity interactions in this flow and to examine the mechanisms which may lead to the mixing enhancement that has been found in previous studies. Molecular Tagging Velocimetry (MTV) was used to measure two components of the velocity field over the streamwise plane (u-v velocity components in the x-y plane) as well as over the cross-stream plane (v-w velocity components in the y-z plane). The spanwise and streamwise vorticity is computed from their respective velocity fields.

The experimental results represent several advances in the MTV measurement technique. Between 600 and 800 velocity vectors were measured per image plane. This represents an increase of more than 50% over previous MTV studies. The present study also represents the first time that this technique has been used to make whole-field measurements in a plane where the mean flow is moving directly out of the measurement plane. Advances were also made in the post-processing of data and the determination of the best methods to remap velocity data onto a regular grid and to compute the vorticity.

The results over the streamwise plane measurement yielded new information about the overall flow properties. The u_{rms} field shows a distinct spatial periodicity that is not found in the unforced case or in unconfined forced flows such as in the wake of an oscillating airfoil. A model was developed which relates this spatial periodicity, which is a consequence of the confinement, to the phase difference between the forcing input into the flow, and the shedding of vorticity. From these data, it was determined that the phase at which vorticity is shed from the splitter plate is dependant upon the forcing amplitude, highlighting the non-linear nature of the shedding process.

The forced wake flow is dominated by the shedding of concentrated, spanwise vortex cores. The behavior of these cores is highly amplitude dependant. As forcing amplitude increases, the vortex spacing ratio, *b/a*, initially decreases. However, as the flow develops sufficiently far downstream, *b/a* increases with increased forcing amplitude. It is recognized, however, that at some point downstream, concentrated regions of ω_z no longer exist and the meaning of *b/a* at those locations is unclear. As the regions of ω_z convect downstream, the levels of peak vorticity within the cores decrease. This decrease has been shown to be dominated by vortex stretching rather than diffusion. A very small negative value of $\frac{\partial w}{\partial z}$ has been found to be sufficient to generate a very large decrease in peak vorticity levels.

In addition to causing the decay of peak vorticity levels in this flow, the enhanced mixing in the center span was found to be well correlated with increases in $-\overline{\frac{\partial w}{\partial z}}$ at center span. A large region of mean $-\overline{\frac{\partial w}{\partial z}}$ is found in the central region of the test section and a large region of $+\overline{\frac{\partial w}{\partial z}}$ is found near the top and bottom walls of the test section for the forcing cases which resulted in large amounts of mixed fluid. This pattern is consistent with a mean recirculatory flow-field found in the cross-stream plane. It is of course recognized that in general, the presence of $-\overline{\frac{\partial w}{\partial z}}$ alone does not result in mixing enhancement. However, in this confined flow, it is indicative of patterns generated by the streamwise vorticity which generates the increased mixing.

An examination of the structure of the spanwise vortex rollers close to the sidewalls of the facility was also conducted. For the high amplitude forcing cases (for 6 Hz forcing, those cases with A > 11.6%) the level of peak spanwise vorticity decreases at locations within the tube that are closer to the sidewall. This is likely connected to the vortex tube reorienting into the streamwise direction. However the peak ω_z, remains relatively constant for the low and moderate amplitude results (A < 8.5%). Further, it was found that the spacing ratio between the vortex cores increases only slightly as the tube moves closer to the wall for these lower amplitude results, whereas it shows a large increase in the ratio is seen for the higher amplitude results.

Although core-wise axial flow was found to be present within the spanwise rollers, its likely does not result in a large increase in the amount of molecularly mixed fluid. The velocity generated by this motion is small and it is only present over a very small spatial extent. Further, the axial motion is located in the center of the vortex core where mixing results indicate the presence of fluid from only one of the two streams. Rather, it is the streamwise vorticity generated by the reorientation of the primary spanwise vorticity which generates the increased molecular mixing. In the high amplitude forcing case, multiple regions of streamwise vorticity are present. These regions generate a recirculating type flow pattern which will result in large quantities of unmixed fluid to be pumped from the free-stream regions in the top and bottom of the test section into the middle where they can interact. These regions also generate small scale motions which will increase the surface area over which the unmixed fluid can interact and mix.

Results of the measurements in the cross-stream plane show that for the high amplitude forcing cases a mean recirculatory pattern is present. This feature is absent in the lower forcing amplitude cases. This flow pattern is consistent with the measurements of $\partial w / \partial z$

previously discussed. In the high amplitude results, multiple regions of $\overline{\omega_x}$ can be found close to center of the facility sufficiently far downstream. Mixing is of course generated by the instantaneous ω_x (or $\langle\omega_x\rangle$) which is also found in the central region. In contrast, the regions of both $\overline{\omega_x}$ and $\langle\omega_x\rangle$ remain close to the wall in the lower amplitude cases.

The development of $\langle\omega_x\rangle$ differs dramatically between the high and lower forcing amplitude cases. Initially, a counter-rotating pair of streamwise vortices is found close to the side wall of the facility for all forcing amplitudes. As the flow develops downstream, these regions begin to move closer to the center of the test section. However, the rate at which these vortices move inward differs greatly between the low and high forcing cases. For the 6 Hz forcing frequency, at 11.6% forcing, the regions of streamwise vorticity quickly occupy the entire test section. For amplitudes of 7.3% and lower, they remain close to the sidewalls of the facility. Furthermore, multiple regions of $\langle\omega_x\rangle$ are found in the high amplitude cases. Although present in the lower amplitude results, the number as well as the strength of these structures is greatly reduced.

A model was developed to account for the development of streamwise vortical structures in this flowfield. As the spanwise rollers convect downstream, the spanwise vorticity is reoriented into the streamwise direction. The ends of these streamwise legs are fixed near the tip of the splitter plate. The multiple regions of $\langle\omega_x\rangle$ in each cross-stream measurement plane are the result of the passage of multiple reorientated spanwise rollers. As a $\langle\omega_z\rangle$ roller convects past a particular downstream location, a region will be reoriented into the streamwise direction. The newly reoriented $\langle\omega_x\rangle$ located closest to the center plane. The "legacy" $\langle\omega_x\rangle$ from the passage of the roller the previous cycle moves closer to the side wall under the action of the newest region.

Similar effects were seen in the development of the velocity and vorticity field for frequencies both larger (8 Hz) and smaller (4 Hz) than 6 Hz case. No mixing studies are available at those frequencies to compare with the present results. From the velocimetry data at these frequencies, it is believed that enhanced mixing will be present in the high amplitude 8 Hz forcing. This case had many of the characteristics, such as a mean recirculatory region and regions of $<\omega_x>$ moving quickly towards the center of the facility that were present in the cases where it is known that a large amount of mixing occurs at the 6 Hz forcing frequency. It is believed that little to no mixing enhancement will be found in any of the 4 Hz forcing cases studied. However, mixing studies need to be conducted to confirm this hypothesis.

Appendices

Appendix A

The Placement of Irregularly Spaced Velocity Measurements on a Regular Grid and the Calculation of Out-of-Plane Vorticity

A.1 Introduction

In recent years, many authors have made use of full-field, two-component optical velocity measurement techniques, such as Particle Image Velocimetry (PIV) to derive other flow quantities such as the out-of-plane vorticity. The data gathered from PIV are normally thought to be gathered on a uniformly spaced grid which allows for a variety of methods to be utilized to calculate these quantities. The development of Molecular Tagging Velocimetry (MTV) has placed an additional complication on the calculation of these quantities in that the data are not normally collected on a uniformly spaced grid. This section deals with the questions related to remapping the MTV data onto a regularly spaced grid and the method used to compute the out-of-plane vorticity component from these remapped data sets.

Molecular Tagging Velocimetry is a full-field optical diagnostic which allows for the non-intrusive measurement of a velocity field in a flowing medium. This technique takes advantage of molecules which have long-lived excited states when tagged by a photon source. The evolution of the luminescence of these molecules is tracked over the luminescence lifetime in order to determine an estimate of the velocity field. MTV has been used by several authors such as Gendrich *et al* (1994), Stier (1994), Cohn *et al.* (1995), Hill

and Klewicki (1996), Koochesfahani *et al.* (1996), Cohn and Koochesfahani (1997), Gendrich, Bohl, and Nocera (1997), and Gendrich, Koochesfahani, and Nocera (1997) to make measurements in a wide variety of flows.

This technique can be thought of as the molecular equivalent of Particle Image Velocimetry. Rather than tracking particles placed in the flowing medium, the luminescence lifetime of the tracer molecules is tracked. A more complete description the implementation of the molecular tagging technique and the parameters necessary for an optimal experiment can be found in Gendrich and Koochesfahani (1996) and Gendrich (1998). The accuracy of velocity measurements made using Molecular Tagging Velocimetry is equivalent to that of PIV. Gendrich and Koochesfahani (1996) report that the *95%* confidence interval for the accuracy of this technique is *0.1* pixel. This means that *95%* of the measurements are more accurate than *0.1* pixel. Thus, a displacement of 10 pixels will yield a dynamic range of *100*.

In the implementation of MTV, a series of laser-lines is used to generate a two-dimensional spatial distribution in the intensity field within the flowing medium. Figure A.1 shows a sample grid used in MTV images. As seen in this figure, these measurement points are typically not regularly spaced. Thus, it is necessary to place data on a regular grid before flow variables can be computed via standard finite difference techniques. It should be noted that it is possible to generate the lines on a regular grid. However, both a study at MSU and Spedding and Rignot (1993) have reported that the best estimate of the velocity value acquired through the use of a measurement technique which tracks a tracer in a flow is located at a point midway between the initial and final location of the feature being tracked. Thus, even if the laser-lines shown in Figure A.1 were uniformly spaced, it would still be necessary to remap the data onto a regular grid. Further, unless special care is taken in the

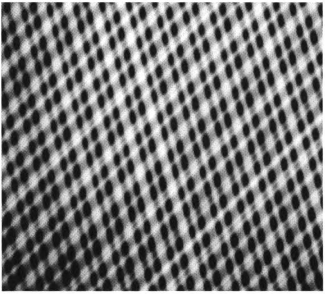

Figure A.1: Sample MTV measurement grid.

selection of the measurement windows, data collected from PIV measurements is not actually on a uniformly spaced grid and should be re-mapped onto a regular grid to achieve the most accurate results.

Agui and Jimenez (1987) examined several different means of interpolating velocity data acquired through the use of particle tracking onto a regularly spaced grid. Comparing the root mean square of the difference between the interpolated velocity and the actual velocity in a simulated flow, it was found that the best results were obtained using certain polynomial interpolaters and a "k-rigging" technique. However, the advantage was small with respect to others methods, so interpolation was performed using a simple convolution with an "adaptive Gaussian window". No additional comparisons between the techniques were included.

Spedding and Rignot (1993) compared the adaptive Gaussian window technique with a "global basis function" in both the accuracy of the interpolation of velocity information and the calculation of out-of-plane vorticity information. Using the root mean square error of the entire flow field, comparisons were made of the results of both the simulated velocity field of an Oseen vortex and the "bootstrap" error between several computed and one real flow field. This error calculation method attempts to place together into one measurement both the mean bias component and the random component of the error found in the entire remapped velocity (or vorticity) field. It will be shown in the following sections that this may lead to misleading results. This study found that the global basis function produced results that were generally superior to the adaptive Gaussian window. It was reported that using the global basis function, the velocity field could be reconstructed to an overall accuracy of *2.5%* and the vorticity field could be reconstructed to an overall accuracy of *5%* given a suitable choise of grid density.

Several studies have examined the accuracy of vorticity calculations from data already on a regular grid. Abrahamson and Lonnes (1995) compared calculating the vorticity from the local circulation of the velocity field as well as using a local least-squares method to calculate the vorticity field. It should be noted that computing the vorticity on by the use of the circulation method is identical to the use of a finite difference calculation on a specially filtered version of the velocity field. This will be shown in the next section. The study by Abrahamson and Lonnes found that both methods spatially filter the flow field and had the largest error in the regions of local maxima and minima in the flow field. However, the circulation method generally out-performed the least-squares technique in this study.

Luff, *et al.* (1999) used the simulated Oseen vortex field to compare the effect of noise on 1^{st} and 2^{nd} order finite difference techniques as well as the 8-point circulation method for the calculation of vorticity. The 8-point circulation method will also be used in the present study and will be described in the next section. Luff, *et al.* studied the propagation of uncertainties into the vorticity field from several sources including the experimental velocity uncertainty, smoothing of the velocity field in order to eliminate spikes in the vorticity data, and spurious or "drop-out" velocity vectors generated in the velocity field. It was found that the circulation and 1st order finite difference methods produced smaller experimental uncertainties than the 2nd order finite difference technique. However, the average uncertainty was found to be $\pm$*37%* of the average value of vorticity ($\pm$*6.5%* of the peak vorticity) with a uncertainty of the order of *550%* of the average value of vorticity (*97%* of the peak vorticity). The use of an "FS-smoothing" procedure resulted in a factor of *10* improvement in both the average and peak uncertainties.

Fouras and Soria (1998) separated the error in the vorticity computation into two portions, the mean bias error and the random error due to the propagation of the error in the velocity field measurements to the vorticity field. The mean bias error is a result of the spatial filtering of the original data and is the cause of the underestimation of the peak vorticity levels. The random error is the result of the errors in the original velocity measurement technique used to acquire the velocity information. These two errors cannot be minimized simultaneously as they are both effected by the spacing between velocity measurements. As the distance between the velocity measurements decrease, the value of the computed vorticity measurement will more closely match the exact value. However, decreasing this spacing makes the measurement more sensitive to the random error found in the initial measurements. In many cases, the mean bias error is significantly larger than the random error propagated into the vorticity field from the velocity field. Simulations of an Oseen Vortex showed that for data already on a uniformly spaced grid this study found that, differentiating a local 2nd order polynomial least squares fit produced more accurate results then estimating the vorticity using a 1st order finite difference technique.

The present study makes use of a simulation of an Oseen vortex in order to study the effect of remapping an irregularly spaced velocity field onto a regular grid and on the calculation of the out-of-plane vorticity component. The velocity field will be remapped by fitting the irregularly spaced data to a 2nd, 3rd, or 4th order polynomial. The vorticity field will then be calculated through the use of one of four methods: differentiating the polynomial fit, 1st and 2nd order finite difference techniques, and an 8-point circulation method.

A.2 Comparison Method

In order to determine the accuracy of the various remapping and vorticity calculation techniques, a simulation with the often used Oseen vortex was conducted. This velocity field has been used in the majority of the previously mentioned studies to determine the accuracy of various interpolaters. This flow has an out-of-plane vorticity, ω_z, and an azimuthal velocity, u_θ profile described by:

$$\omega_z = \omega_{max} e^{-(r^2/r_{core}^2)}$$

$$u_\theta = \frac{\omega_{max} r_{core}^2}{2r}\left(1 - e^{-(r^2/r_{core}^2)}\right).$$

In order to simulate the irregular spacing found in the MTV velocity field caused by the laser grid generation and the placement of the velocity vectors in between the initial and final location of the feature being tracked, the initial velocity measurements are irregularly spaced as shown in Figure A.2a. The irregular spacing was generated by sub-dividing the measurement field into δ x δ sized regions, where δ is the mean spacing between velocity measurement points. A random number generator is then used to place each velocity

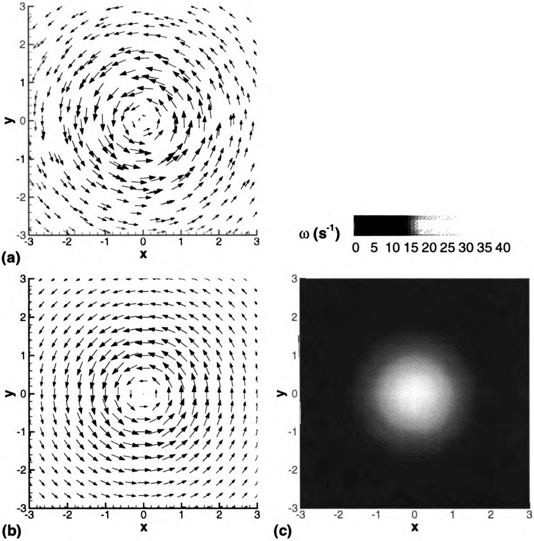

Figure A.2: Sample velocity and vorticity field of Gaussian core vortex. (a) Original velocity vector field. (b) Velocity vector field placed on a regular grid. (c) Flooded contour plot of the vorticity field.

measurement point at a random location within the δ x δ sized regions. In this manner, the mean spacing between measurement points will remain a constant value of δ, however the actual location of the measurements will vary.

In Figure A.2b the irregular velocity field shown in Figure A.2a is remapped onto a regular grid by one of the polynomial interpolaters. It is interesting that even though the irregularly and the regularly spaced measurements have the same mean densities, the Oseen vortex seems more distinguishable in Figure A.2b. From these regularly spaced measurements, the vorticity field can be computed through the use of many methods. Figure A.2c shows a flooded contour plot of the vorticity field computed from the regular grid data is seen in Figure A.2c.

The data will be remapped onto a regular grid by means of a local two-dimensional least squares fit to a 2nd, 3rd, or 4th order polynomial. The *u* and *v* velocity fields are fit separately. After the fits for the two velocity components are generated, each local fit is evaluated at the regular grid point location to determine the velocity at that particular grid point. In all cases, the fit is over-determined. That is, for any order fit, there is a minimum number of points necessary in order to perform the fit. It can be found that the minimum number of points necessary for a fit to be properly determined is *(order+1)*(order+2)/2*. So, for the 2nd order polynomial fit, a minimum of *6* points is necessary for the fit to be properly determined. For all of the measurements reported more than the minimum number of points are used in the fit. This will tend to reduce the random errors found in the original measurements.

The computation of the out-of-plane vorticity component will be computed in four different ways. The first three methods differ in the manner in which they estimate the spatial derivatives of the velocity field. The out-of-plane vorticity, ω_z can be computed from the spatial derivatives of the velocity field using the relation

$$\omega_z = \frac{\partial v}{\partial x} - \frac{\partial u}{\partial y}.$$

In the first method, the velocity derivatives will be estimated by directly differentiating the local polynomial fit. As the fit is a polynomial, the calculation of the derivative from the fit is straight-forward and does not require any added computation after placement onto a regular grid. This method has the advantage that it can also be used to compute the vorticity on the original irregular grid.

Once the velocity is on a regularly spaced grid, it can be numerically differentiated using finite difference techniques. Two different finite difference methods will be examined: a first order central (2[nd] order accurate) and second order central (4[th] order accurate). In the first order central method, the two spatial derivatives used in the vorticity calculation are defined by

$$\left(\frac{\partial u}{\partial y}\right)_{i,j} = \frac{u_{i,j+1} - u_{i,j-1}}{2h}$$

$$\left(\frac{\partial v}{\partial x}\right)_{i,j} = \frac{v_{i+1,j} - v_{i-1,j}}{2h},$$

where (i,j) subscript indicates the relative location of the point in the regular grid. These locations are indicated in Figure A.3a. This is the standard algorithm used in several commercial packages for the computation of ω_z. The 2[nd] order central (4[th] order accurate) utilizes 8 points in the estimation of the spatial derivatives to provide a higher order estimation of the spatial derivatives. The location of the measurement points used can be seen in Figure A.3b. The spatial velocity derivatives for the 2[nd] order method are defined by

$$\left(\frac{\partial u}{\partial y}\right)_{i,j} = \frac{-u_{i,j+2} + 8u_{i,j+1} - 8u_{i,j-1} + u_{i,j-2}}{12h}$$

$$\left(\frac{\partial v}{\partial x}\right)_{i,j} = \frac{-v_{i+2,j} + 8v_{i+1,j} - 8v_{i-1,j} + v_{i-2,j}}{12h}$$

will be examined.

The final vorticity calculation method computes the circulation around a rectangular circuit that extends one regular grid point in each direction around the point to be examined as shown in Figure A.3c. This circulation value is then divided by the area in order to determine the vorticity. Using this method, the vorticity can be calculated using the relation:

$$\omega_{z;i,j} = \frac{1}{4h^2}\{2h(\tfrac{1}{4}u_{i-1,j+1} + \tfrac{1}{2}u_{i,j+1} + \tfrac{1}{4}u_{i+1,j+1}) +$$
$$2h(\tfrac{1}{4}v_{i+1,j-1} + \tfrac{1}{2}v_{i+1,j} + \tfrac{1}{4}v_{i+1,j+1}) +$$
$$2h(\tfrac{1}{4}u_{i-1,j-1} + \tfrac{1}{2}u_{i,j-1} + \tfrac{1}{4}u_{i+1,j-1}) +$$
$$2h(\tfrac{1}{4}v_{i+1,j-1} + \tfrac{1}{2}v_{+1i,j} + \tfrac{1}{4}v_{i+1,j+1})\},$$

where h is the separation between neighboring grids and the integrals are estimated using the trapezoidal rule. It can be shown that this method is identical to a filtered version of the 1st order central finite difference technique where the velocity at each point (i,j) is replaced with its "3-point average" defined as :

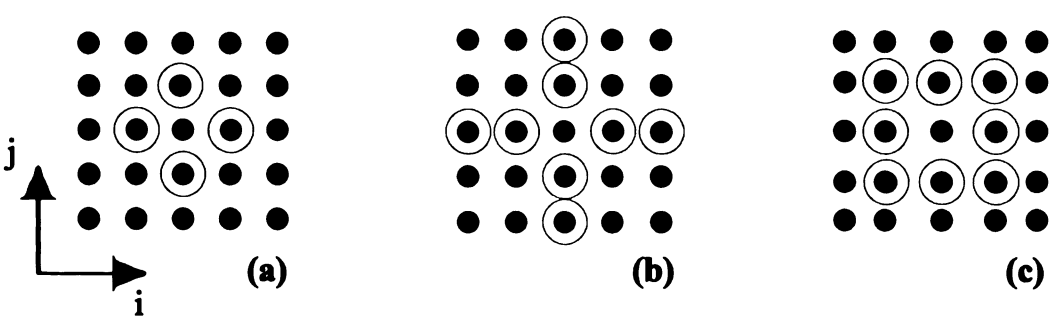

Figure A.3: Schematic of velocity measurement locations used in the estimation of the spatial derivatives. (a) 1st order finite difference. (b) 2nd order finite difference. (c) 8-point circulation method.

$$u_{i,j} = \frac{1}{2}u_{i,j} + \frac{1}{4}(u_{i+1,j} + u_{i-1,j})$$
$$v_{i,j} = \frac{1}{2}v_{i,j} + \frac{1}{4}(v_{i,j-1} + v_{i,j-1}).$$

The use of the 1st order central difference relation on the above filtered field will recover the previous expression for vorticity.

There are several parameters which are important in the determination of the accuracy of both the remapping scheme and the calculation of ω_z. In this study, we will examine the effect of the mean spacing of the original velocity measurements, δ, and the radius R, from which points are drawn from for use in the fitting procedure. The mean spacing between the original velocity measurements yields information about the smallest structure size which can be resolved by the measurement technique. This size must be larger than δ. In order to examine this effect, the ratio of the structure size in the simulation, L to δ will be examined. The characteristic flow scale used in this study is the vortex core radius, r_{core} defined as the distance from the peak vorticity to the location where the vorticity has dropped by a factor of e^{-1}. Simulations will be conducted for values of L/δ ranging from *2.5* to *10.5*.

Using the interpolation techniques, it is possible to create a regularized velocity field that has a mean spacing between points, h, that is larger or smaller than that of the original field. For all of the studies described here, $h = \delta$. If the interpolater is used to generate data with $h < \delta$, it may appear that information about small-size structures can be determined, however, no new information can be generated during the interpolation process. Information is simply re-used. The information a. If $h > \delta$, information about small-size structures could be lost.

As previously described, the least-squares fitting process was over-determined for all of the simulations performed in this study. However, it was found that the radius from which points are drawn, R, for use in the fit can play a significant role in the estimation of both the velocity and vorticity field. R will be normalized by δ for the results presented in this study. Decreasing the size of this region has the of decreasing the number of points available for use in the fitting procedure and will provide a more local estimate of the velocity and vorticity field. This typically results in an increase in the accuracy of the measurement, however it also tends to increase the propagation of error from the velocity measurement.

Since higher order polynomials require more points for the fit to be properly determined, when the results of the remapping and vorticity calculations are compared between different fit orders, different R values are used for the different order polynomial fits. For each fit order, there will be a minimum radius, R_{min} necessary for the fit to be properly determined. For the studies comparing the different fit orders, R/R_{min} is kept at a constant value of *4.5*. This results in R values for the 2^{nd}, 3^{rd}, and 4^{th} order polynomial fits of 2.9δ, 3.8δ, and 4.6δ respectively.

As in the results of Fouras and Soria (1998), the accuracy of the three different polynomial least-squares fit orders and the different vorticity calculation methods are measured by the mean bias error caused by spatial filtering and a random error caused by both the propagation of the error in the original measurements to the remapped field and the placement of the randomly spaced points onto the regular grid. Within each sample set, *100* random simulations are conducted. The mean bias error will be denoted by the subscript *bias* and refers to difference between the mean value of these *100* measurements and the exact value at a point in the flowfield. The random error is quantified by the root mean square of difference between the interpolated velocity or computed vorticity value and the actual value at each point in the 100 measurement samples of the simulation. This will be denoted by the subscript *rms*.

In order to more closely simulate actual velocity measurements which will contain a random error inherent in the measurement technique, noise was added to the simulated data field. The method used is similar to that in Luff, *et al.* (1999). A random number generator is used to add a random percentage of noise, with a maximum value of $\pm n\%$ to each component of the velocity field. With this formulation, the velocity at each point in the simulation had a value of:

$$u = u_{act}(1 + n_{random})$$
$$v = v_{act}(1 + n_{random})$$

where n_{random} is a random number with a value $-n < n_{random} < +n$. of the actual velocity value to each component of the velocity.

A.3 Interpolation Results

Figure A.4 shows a profile of the velocity bias error for the 2nd, 3rd, and 4th order fits The error is normalized by the peak velocity found in the flow. A radial cross-section of the vortex core ranging from the center of vorticity to a radius where $r/r_{core} = 3$ is examined for all plots presented in this work. Grid densities ranging from $L/\delta = 2.5$ to $L/\delta = 10.5$ is examined in this work. In all cases, the maximum error occurs at approximately $r/r_{core} = 0.5$, which is in a region of large velocity gradient. Increasing the grid density greatly decreases the error for all fit orders. In the 2nd order fit case, increasing the grid density from *2.5* to *3.5* decreases the maximum error from *5%* of the maximum velocity to less than *2%* of the

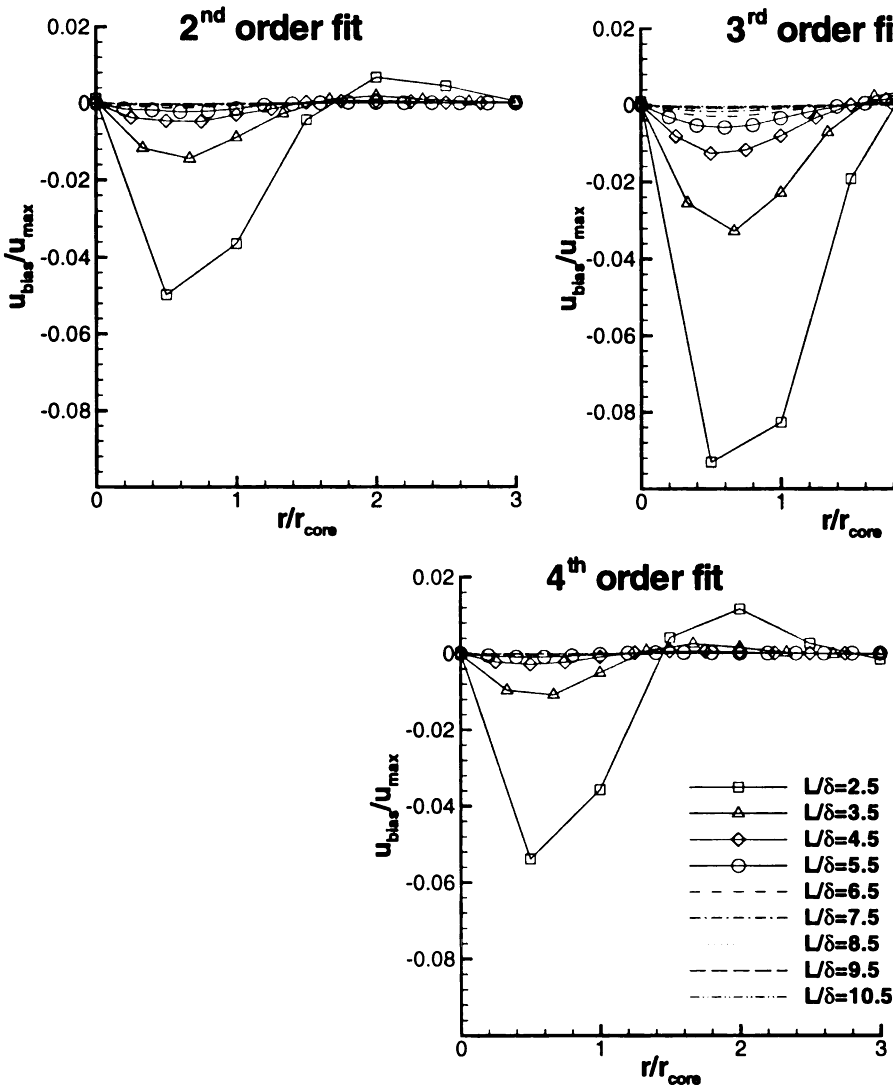

Figure A.4: Profiles of the mean velocity bias error for 2[nd], 3[rd], and 4[th] order polynomial fits for grid densities ranging from *L/δ = 2.5* to *L/δ = 10.5*.

maximum velocity. For L/δ larger than 4.5, the interpolation error is less than 0.5% for all locations. In addition to the large underestimation of the velocity error which is a maximum at $r/r_{core} = 0.5$, the interpolation overestimates the velocity field in the region $r/r_{core} > 1.5$. It should be noted that the presence of this overshoot in this region can lead to misleading results if the mean error is integrated over the entire region to determine one value. Several previous studies have attempted to quote a single number for the overall accuracy of the interpolation procedure. Since the area over of the region of the overshoot is about three times larger than that of the undershoot region, the mean velocity error averages to nearly zero. This is not indicative of the error found in this flow. If an RMS is taken, the undershoot near $r/r_{core} = 0.5$ will dominate the error value and the fact that interpolater produces values with little error at many points in the flowfield will be lost.

It is also apparent that the mean velocity error for the 2nd and 4th order polynomial fits is significantly smaller than that found using the 3rd order polynomial interpolater. This is seen more clearly in Figure A.5. A.5a shows the mean error for $L/\delta = 3.5$ for the three fit orders. Results with a maximum added of 0% and $\pm 6\%$ of the velocity added to the original irregularly spaced field are presented. The effect of adding additional noise is very similar to the $\pm 6\%$ value. No discernable impact can be seen in the mean results as a result of the added noise. The 2nd and 4th order polynomial fits do a nearly equivalent job interpolating the irregularly spaced data onto a regular grid. The magnitude of the u_{bias} associated with the 4th order fit is less than 0.5% of the peak velocity less than that of the 2nd order fit. It should be noted, however, that different R values used for the different order polynomial fits. Decreasing the radius will result in more accurate results for all fit orders.

Figure A.5b show the profile of the root mean square of the error between the actual

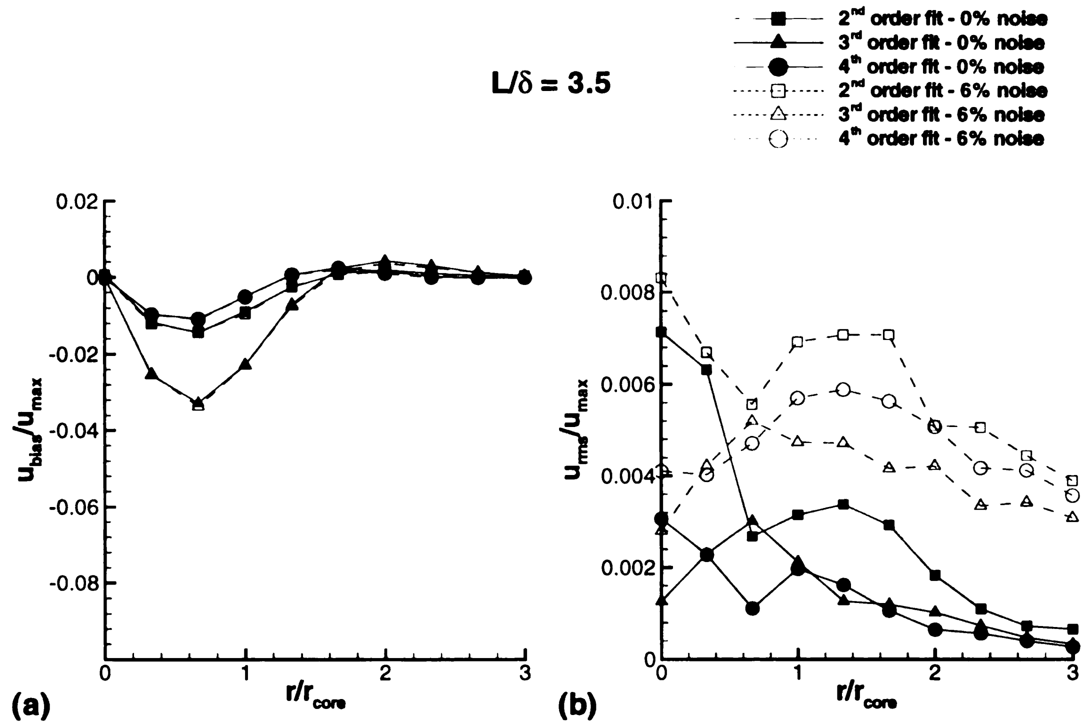

Figure A.5: Comparison of the error in the velocity field resulting from the 2nd, 3rd, and 4th order polynomial fits for the *0%* and *6%* noise added cases for a normalized grid density of *3.5*. (a) u_{bias}. (b) u_{rms}.

velocity and the interpolated velocity for the *100* samples. The addition of noise into the original measurements results in a small increase in the u_{rms} for all of the fit orders. However, the least squares fitting process tended to minimize the effect of this randomly distributed nose error. Note that even the noise-free data contains a random error. This is due to the remapping process itself. The u_{rms} of the error for the 2nd order polynomial fit results is slightly larger than the error for the other two cases, but this difference is fairly small. The difference is likely caused by more points being used in the fit for the higher order polynomial fits. For all cases, the u_{rms} error is less than approximately *0.8%* of the maximum velocity.

Figure A.6a and A.6c shows the effect of reducing the maximum radius from which

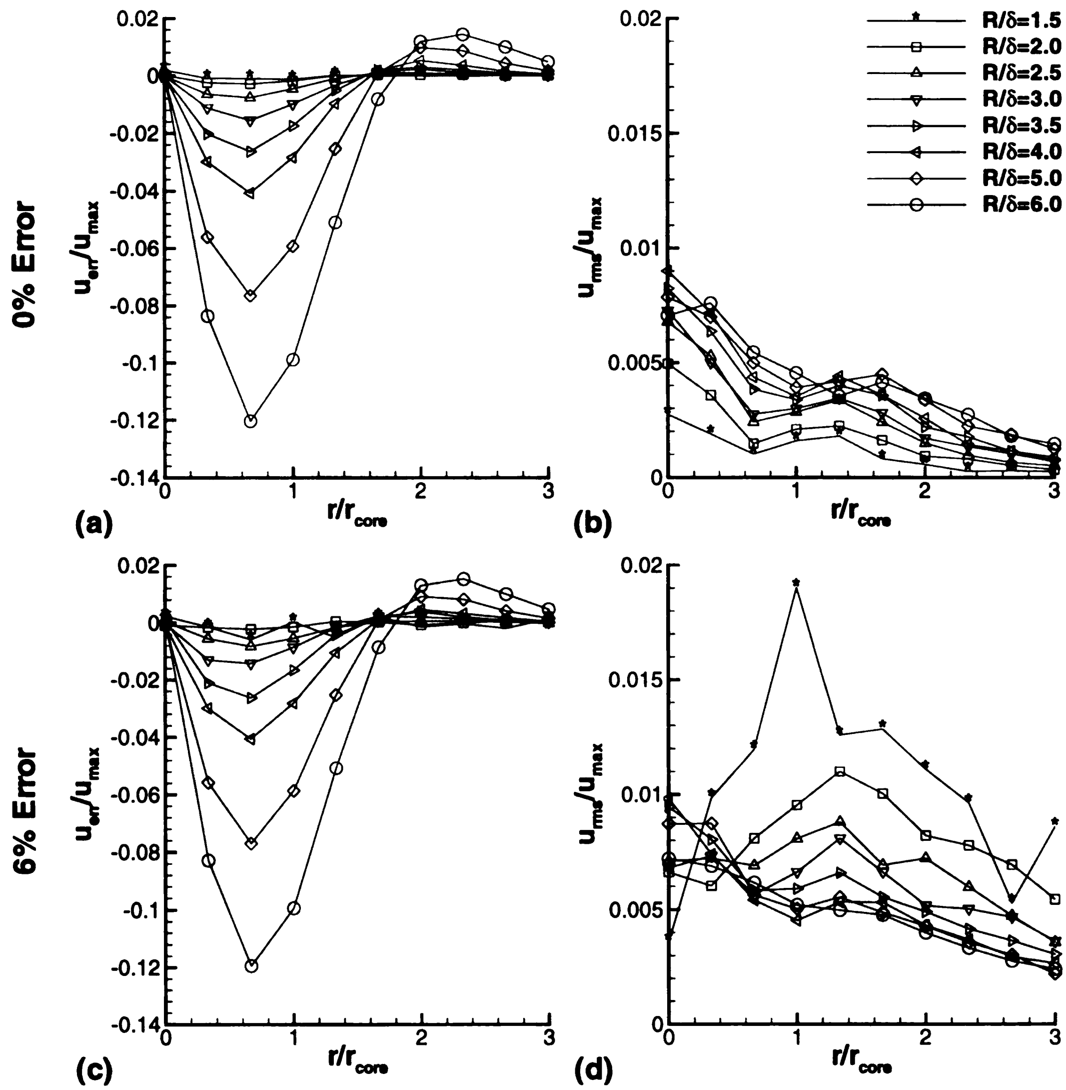

Figure A.6: Effect of decreasing the radius from which irregular points are drawn in the interpolation process on the velocity mean bias and random error. (a) u_{bias} for *0%* noise added case. (b) u_{rms} *0%* noise added case. (c) u_{bias} for *6%* noise added. (d) u_{rms} for *6%* noise added.

the irregularly spaced points are drawn for use in the fit. As all of the cases show similar effects, only the $L/\delta = 3.5$ results are examined. The mean velocity error results for both no noise added and the 6% noise added are very similar. Small values of R/δ generates the smallest mean error. The addition of noise has the most significant effect on the error for $R/\delta = 1.5$ causing a slight increase in the maximum mean error from 0.2% of the maximum velocity to 0.6% of the maximum velocity when noise is added. When noise is added, the maximum mean velocity error is smaller in the $R/\delta = 2.0$ case. For R/δ values greater than 3.0, u_{bias} continues to increase and at $R/\delta = 6.0$, the maximum value of $u_{bias} = 12\%$ of the peak velocity.

The random component of the error is shown in Figure A.6b and A.6d. For the 0% noise added results, u_{rms} is minimized at small values of R/δ. However, increases in R/δ cause only a small change in u_{rms}, and the maximum value of u_{rms} for the 0% noise added results is less than 0.8% of the maximum velocity. Figure A.5d shows the effect of the addition of the random 6% noise to the original measurement data on u_{rms}. When noise is added, increasing R/δ results in the minimum values of u_{rms}. However, the decrease in u_{rms} with increasing R/δ is small in comparison to the increases seen in u_{bias} for increasing R/δ.

A.4 Vorticity Calculation Results

In this section, the error generated by the four methods for calculating the out-of-plane vorticity field will be examined. First, the results of differentiating the various polynomial fit orders to determine the vorticity value will be discussed. Then, the results from this method will compared with those from the finite difference and circulation methods.

Figure A.7 compares the mean accuracy of the vorticity calculation using the fit differentiation method for four values of L/δ. In all cases, the result of differentiating the third order polynomial results in a smaller error than the result of differentiating the 2nd or 4th order polynomials. For all cases, the maximum ω_{bias} is located at the center of the vortex core. For $L/\delta = 2.5$, the third order fit results in the vorticity being underestimated by nearly *25%* while the differentiation of the 2nd and 4th order fit results in an error of *45%* and *35%* of the maximum vorticity respectively. As the grid density is increased, ω_{bias} decreases to nearly zero for all cases.

The random error associated with the vorticity field calculations is shown in Figure A.8. The same four grid densities shown in Figure A.7 are examined in this plot. For the *0%* noise added case, as the grid density is increased, the random error decreases. The fact that fluctuations are found when no noise is present in the data is the result of the random placement of the velocity information. Note that decrease in ω_{rms} with increasing grid density is not contradictory to the findings of Fouras and Soria (1998) that increasing the separation between velocity measurements results in a decrease in the random error. As the grid density is increased, additional information is being added to the velocity field. If the mean spacing in the initial, irregularly spaced grid, δ, is kept constant and the spacing in the regular grid is decreased, the random noise error will increase as found by Fouras and Soria (1998). When noise is added, the random error increases as the grid density increases. However, the maximum random error is less than *3%* of the maximum vorticity. This is small compared to the *25%* bias error.

Since the results of differentiating the 3rd order polynomial fit clearly outperform the

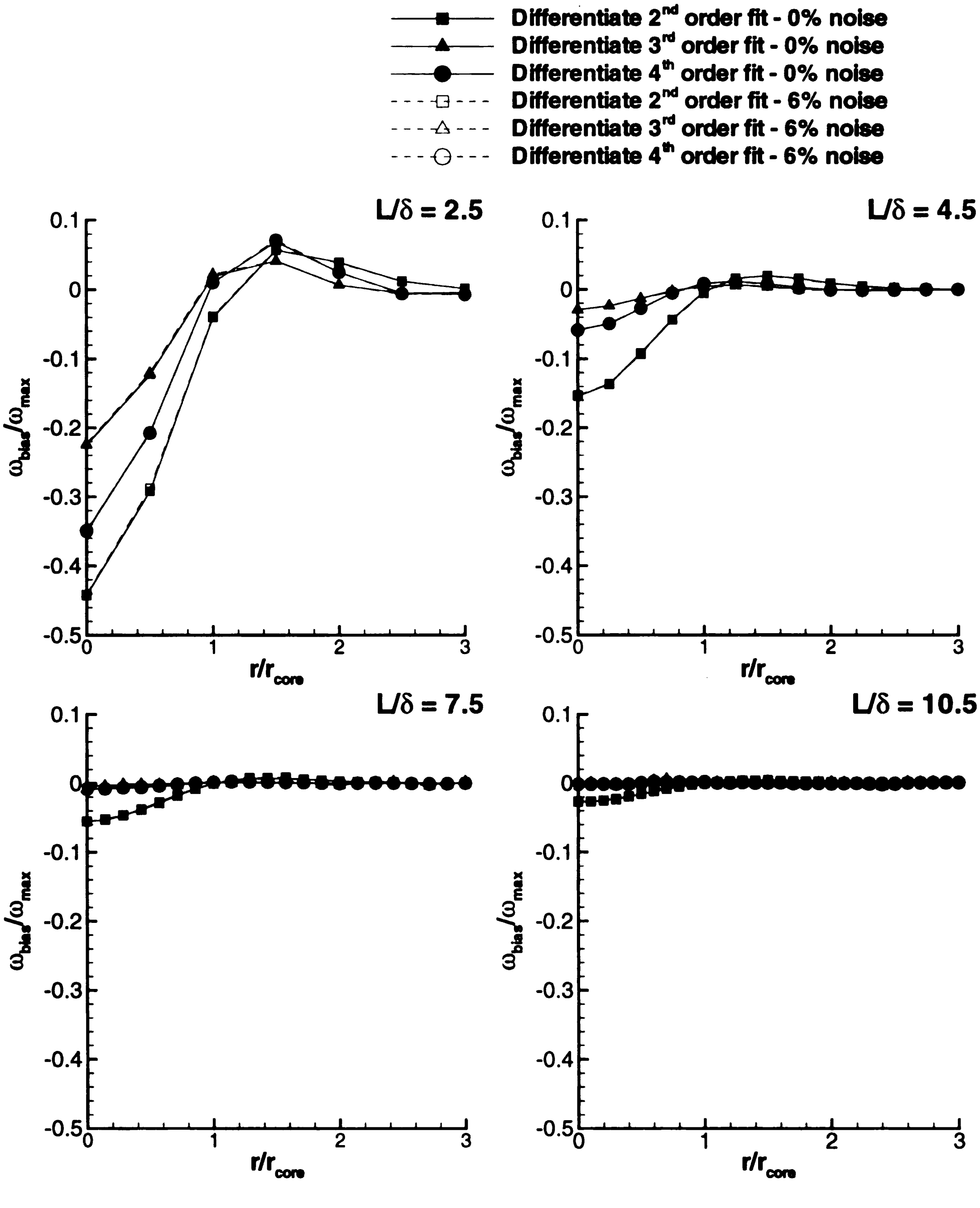

Figure A.7: Comparison of the vorticity mean bias error profile resulting from the use of differentiating the 2nd, 3rd, and 4th order polynomial fit for the calculation of the out-of-plane vorticity for four different grid densities. Results from simulations with *0%* added and a maximum of *6%* uniform noise are shown.

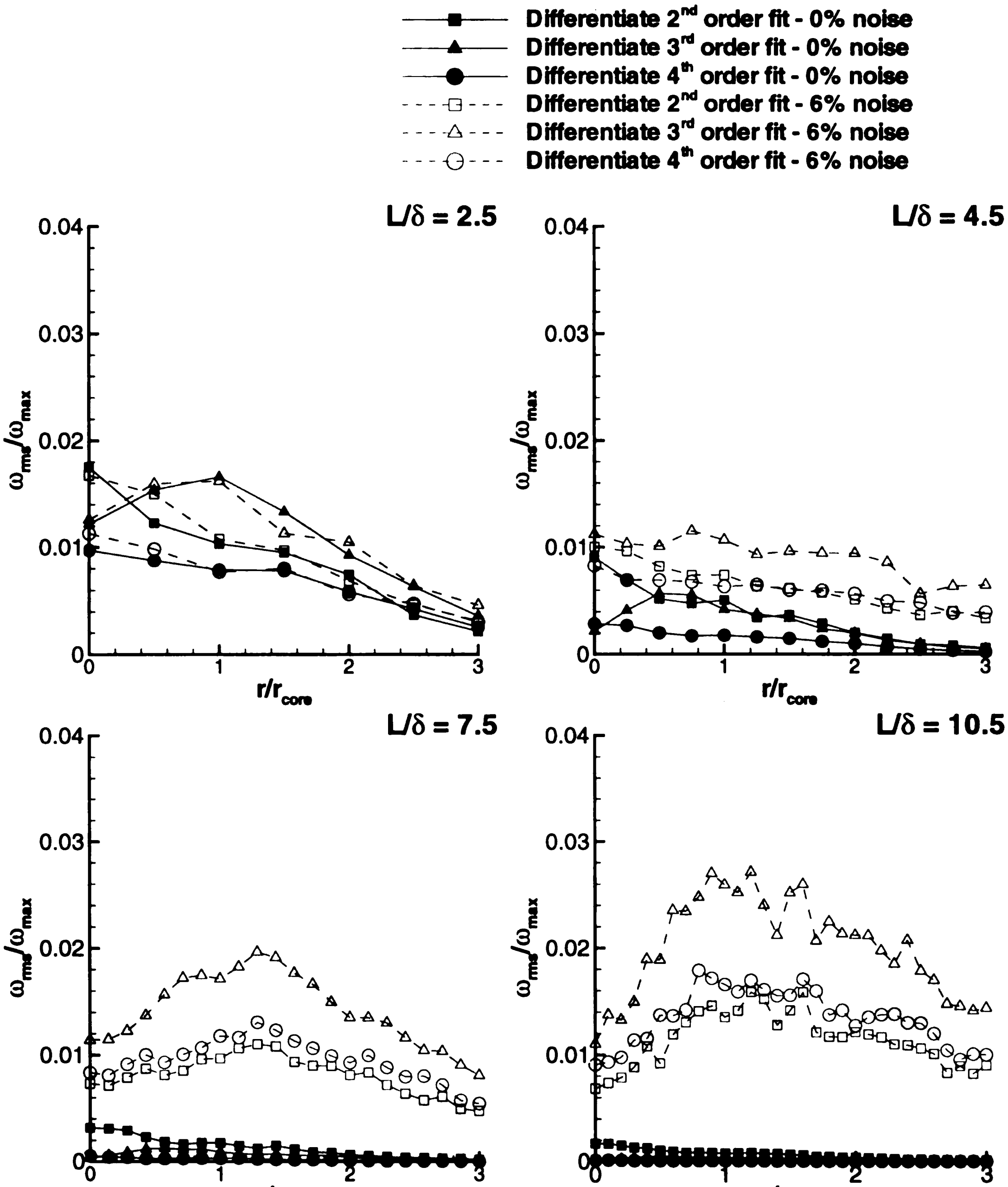

Figure A.8: Comparison of the random vorticity error profile resulting from the use of differentiating the 2nd, 3rd, and 4th order polynomial fit for the calculation of the out-of-plane vorticity for four different grid densities. Results from simulations with *0%* added and a maximum of *6%* noise are shown.

results from the other two fit orders, only the 3rd order fit results will be compared with the ω_z values calculated using the finite difference and circulation methods. For the two finite difference methods and the circulation methods, only the results from the 2nd order polynomial least squares fit shown in the previous section will be utilized. In the previous section, it was shown that the vorticity estimates calculated through the use of these methods rely solely on the velocity information on the regularly spaced grid. The interpolation results for the 2nd and 4th order polynomial fits were very similar. As expected, this results in very similar results for the vorticity calculation. Since the 2nd order fit is less computationally intensive and allows for a smaller number of surrounding points to be used in the interpolation process it was used instead of the 4th order fit. Both of these interpolation techniques produced results significantly better than the 3rd order least squares fit. As expected, the decreased accuracy in the remapped 3rd order fit velocity information results in decreased accuracy in the vorticity calculation.

Figure A.9 compares ω_{bias} found by differentiating the 3rd order polynomial least squares fit with the finite difference and circulation methods. Once again, the effect of adding noise to the initial velocity field is negligible. The qualitative features of the four methods are very similar. The maximum ω_{bias} is at $r/r_{core} = 0$ which is the location of the peak vorticity. At $r/r_{core} = 1.5$, there is a small overshoot where the vorticity value is overestimated. Note that although the numerical amount of the overshoot is small relative to the undershoot, the area occupied by the region of overshoot is roughly three times larger than the region of undershoot. Thus, the overall averaged random error will be significantly smaller than the peak. The estimate of the overall circulation of the vortex computed by integrating the vorticity field will yield a result accurate to better than *0.1%* even for $L/\delta =$

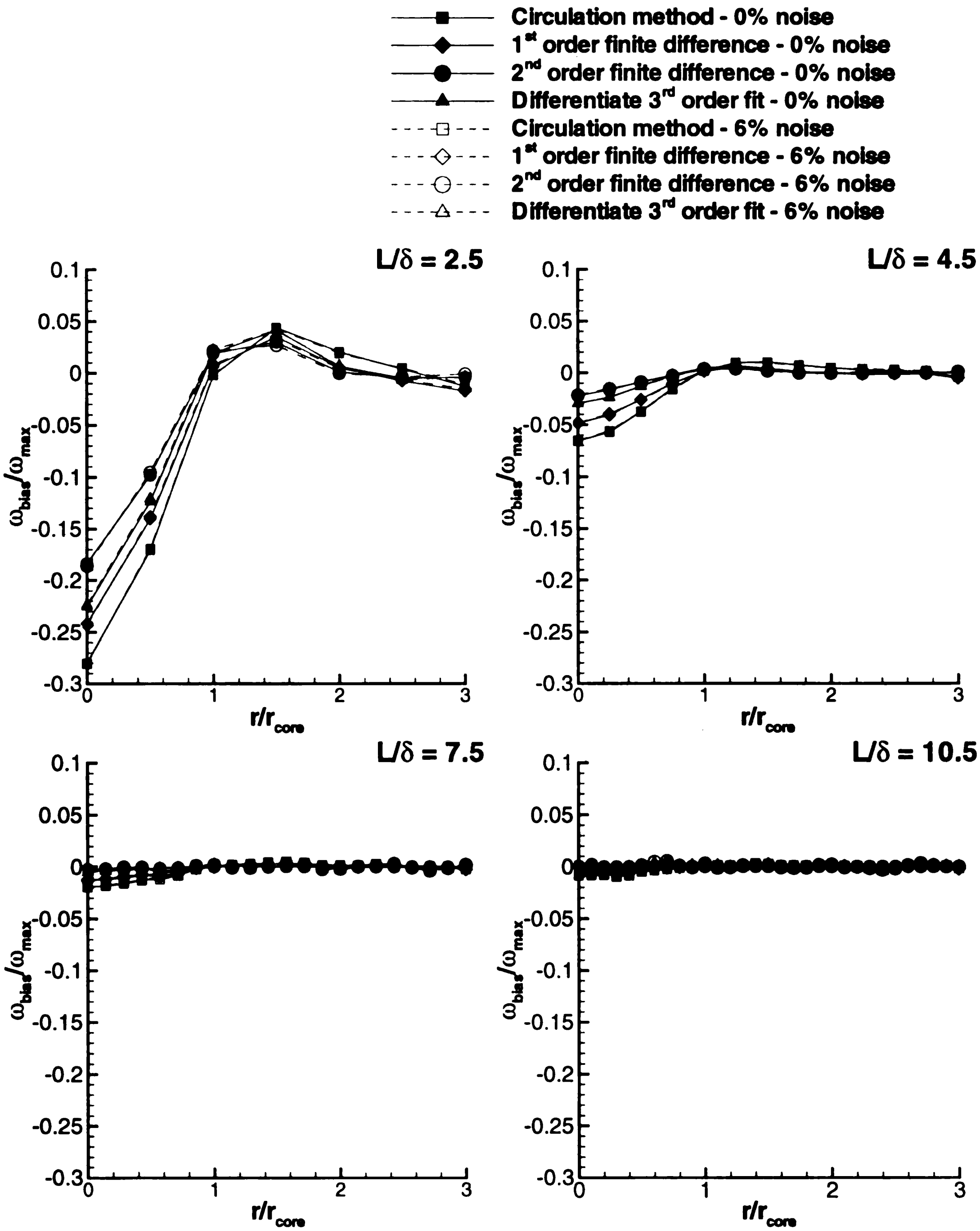

Figure A.9: Comparison of the mean vorticity bias error profile resulting from the use of the circulation method, 1st and 2nd order finite difference methods, and differentiating the 3rd order polynomial fit for the calculation of the out-of-plane vorticity for four different grid densities. Results from simulations with *0%* and *6%* noise added are shown.

2.5 which underestimated the peak vorticity by nearly *20%*.

Quantitatively, ω_{bias} decreases as the grid density increases. The use of the 2nd order finite difference method outperforms all other methods for low grid densities. As grid density increases, the difference between the methods becomes smaller and smaller as the all methods do a very good job. For the $L/\delta = 2.5$ case, the maximum error for the 2nd order finite difference method is *18%*. In comparison, differentiating the 3rd order polynomial results in a maximum bias error of *22%*, the 1st order finite difference method results in a maximum bias error of *24%*, and the circulation method results in a maximum error of *28%*. For the $L/\delta = 10.5$ case the maximum bias error is less than *1%* of the maximum vorticity for all calculation methods.

The random error in the vorticity computation is plotted in Figure A.10. As with the results found in comparing the results from differentiating different order polynomials, ω_{rms} decreases with increasing grid density in the no noise added results, and increases with increasing grid density for cases where noise is present in the initial data. The maximum random error, however, is small compared to the maximum bias errors. It should be noted that the circulation method is the least sensitive to the addition of noise.

The effect of varying the maximum radius from which irregular grid points are drawn from in the least squares fit on the vorticity calculation is shown in Figure A.11. Only the results from the two methods showing the smallest ω_{bias}, differentiating the 3rd order fit and the 2nd order finite difference method, are shown. Note that in Figure A.6 which examined the variation of u_{bias} and u_{rms} with R/δ, the smallest value examined was $R/\delta = 1.5$. This value of R/δ is not present in Figure A.11 as both ω_{bias} and ω_{rms} found using this radius are very large. As with the results for velocity, decreasing the R decreases the mean bias error.

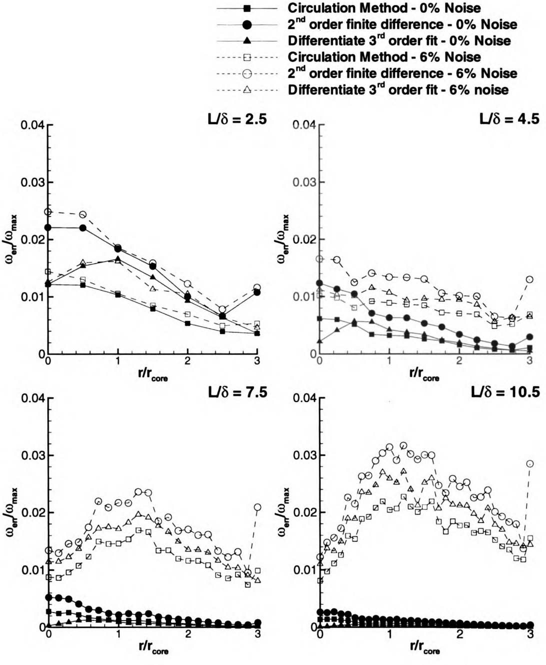

Figure A.10: Comparison of the vorticity random error profile resulting from the use of the circulation method, 1st and 2nd order finite difference methods, and differentiating the 3rd order polynomial fit for the calculation of the out-of-plane vorticity for four different grid densities. Results from simulations with *0%* and *6%* noise added are shown.

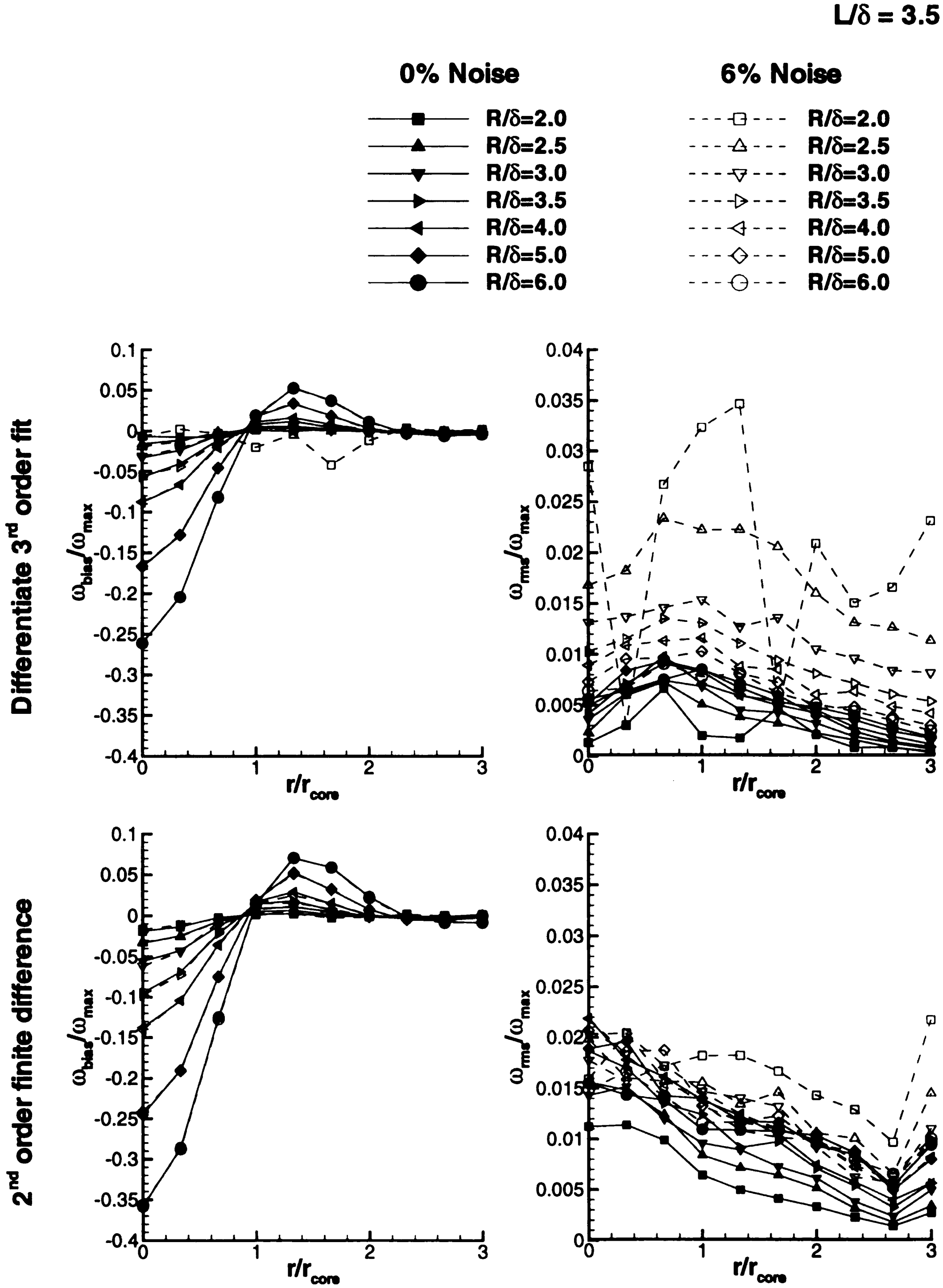

Figure A.11: Effect of varying the radius from which points are selected in the interpolation process on the mean bias and random error for the vorticity computed by means of differentiating the 3rd order polynomial and the use of the 2nd order finite difference method.

The effect of adding noise to the mean error is negligible except for the smallest radius for the differentiation method results. For small values of R/δ, the differentiation method results in a mean bias error of less than 0.5%. For the same R/δ, the 2nd order finite difference method results in a ω_{bias} of 2% of the maximum vorticity. Both methods are very sensitive to increases in R/δ. For $R/\delta = 6$, the ω_{bias} for the 2nd order finite difference method has increased to *35%* compared to *25%* for differentiating the 3rd order polynomial.

As in the study of the effect of R/δ on the remapped velocity field, when no noise is added to the measurements, increasing R results in an increase in ω_{rms}. However, when noise is added to the velocity field, increasing R results in a decrease in ω_{rms}. In the 0% noise measurements, ω_{rms} for the differentiating the 3rd order fit is less than that for the 2nd order finite difference technique. However, the differentiation method is more sensitive to the addition of noise in the velocity measurements. Again, these errors are generally small in comparison to the ω_{bias} errors present. For the differentiation results, the maximum ω_{rms} is *1%* and *3.5%* of the peak vorticity value for the *0%* and *6%* noise added results respectively. For the 2nd order finite difference technique, the maximum ω_{rms} for both the *0%* and *6%* noise results is 2% of the peak vorticity value.

A.5 Conclusions

The effect of remapping an irregularly spaced velocity measurements onto a uniformly spaced grid and the accuracy of the out-of-plane vorticity computed from this information has been studied through the use of a Gaussian core vortex simulation. Remapping onto a regular grid was performed by the use of a 2nd, 3rd, and 4th order least squares fit. The vorticity is computed by means of calculating the derivatives necessary for the computation of vorticity by means of directly differentiating the least squares fit, performing a 1st or 2nd order finite difference calculation on the regularly spaced data, and by computing the local circulation of the region around a point and dividing by the area. The effect of varying the normalized grid density (ratio of the flow characteristic length to the mean spacing in the initial velocity measurement) and the maximum radius from which points are used in the remapping process was examined. For all of the studies conducted, the density of the remapped, uniformly spaced grid remained the same as the initial irregularly spaced measurement grid.

Two types of error are present when remapping data from an irregularly spaced grid to a regularly spaced grid and in the computation of the out-of-plane vorticity: a mean bias error due to spatial filtering and a random error due to the remapping process itself and the propagation of the error in the original data. The mean bias error is not effected by noise in the original measurements and can be decreased by increasing the grid density. The random error can be affected by the presence of noise in the original measurements, which causes an increase in the random error. However, the filtering inherent in the fitting process tends to decrease the magnitude of the random error in the regular grid as compared to that which would be expected. Generally, the errors resulting from u_{bias} are significantly larger than those in u_{bias}.

When remapping data from an irregular grid onto a regularly spaced grid, a least squares fit to an even order polynomial does a better job then an odd order least square fit. It is also apparent that it is necessary to have a sufficient grid density in order to accurately reproduce the flow features. If the ratio of the flow characteristic length to the mean spacing between measurement points, L/δ, is greater than 3.5, the maximum u_{bias} is less than 1.5% of the maximum velocity. Even in the presence of noise, the random error is less than 1%. If $L/\delta = 2.5$, the u_{bias} is less than 5% of the maximum velocity. It was also found that decreasing the radius from which irregular points used in the fit are drawn from can significantly decrease the values of u_{bias}.

Using the 2nd order finite difference technique and differentiating the 3rd order polynomial fit provide the most accurate estimates of the out-of-plane vorticity. It is interesting that the differentiating the 3rd order fit yields more accurate vorticity calculations than differentiating the 2nd or 4th order fits since the even order fits provide a better estimate of the velocity field. Using the 2nd order finite difference technique to estimate the vorticity provided the best representation of the actual vorticity field with a maximum bias error of 2% of the peak vorticity can be achieved for $L/\delta = 4.5$, and for $L/\delta = 2.5$, the maximum error is less than 20% of the peak vorticity. Differentiating the 3rd order fit produced bias errors that were only slightly larger than the 2nd order finite difference method. However, it was found that decreasing R significantly improved the results of the 3rd order fit. For both methods, u_{rms} is relatively constant across the vortex core and is less than 2.5% of the peak vorticity. It should be noted that although a mean bias exists in the lower density results, a vortex core will still be found in the interpolated results and the peak vorticity will be at the same location as is found in the higher density results.

Appendix B

The Computation of Mean Quantities of Phase-Locked Signals Using Sparsely Sampled Data

When a phase locked signal is sparsely sampled in time, it is possible that simply summing the signal and dividing by the number of samples may not yield the best estimate of the true mean value of the signal. This scenario occurs in many experiments utilizing whole field velocity measurement techniques based on the recording of images from video cameras. For example, in the Molecular Tagging Velocimetry Experiments conducted in this thesis, the characteristic frequency of the flow is 6 Hz, while the measurement sampling rate is approximately 30 Hz. Thus, only five measurements are made per forcing cycle.

In cases where the signal being measured is periodic, it is possible to use the frequency information to construct a more accurate time average with a shorter record length. To show this, a sinusoidal signal of the form:

$$y = \sin(2\pi f t + \phi),$$

where f is the signal frequency and ϕ is an arbitrarily selected starting phase was examined. In the results presented here, the frequency of the input signal, $f = 6.01\ Hz$ and the sampling rate is $30\ Hz$. Given this choice of parameters, approximately 5 measurements of the sinusoid per cycle were used in the construction of the average. These numbers were selected to best match the data to be collected in the forced wake MTV experiments. In this

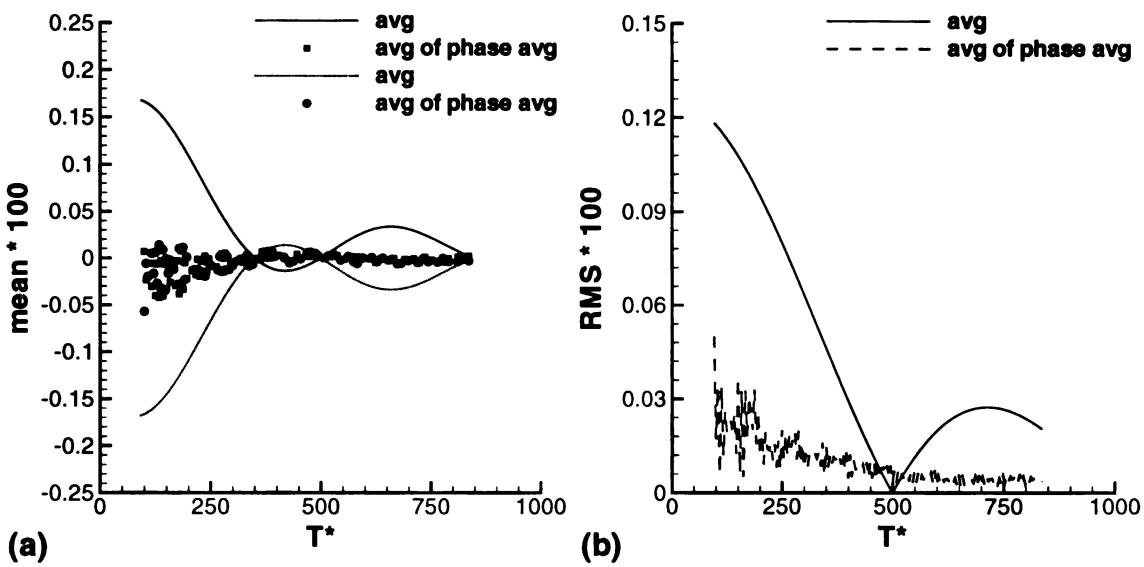

Figure B.1: Comparison of the estimation of the mean using direct computation versus calculating the phase average and the computing the mean. (a) Average value of sinusoidal signals with two different starting phases. (b) Root mean square of 16 starting phases.

study the non-dimensional record length, T^* defined as the total time of the data record divided by the period of the signal, is varied. It should be noted that for the technique described to be successful, the sampling rate must not be an exact measurement multiple of the frequency of the signal to be measured.

Using the known signal frequency, the sparsely sampled data can be first phase-averaged. The mean value of the signal is then computed by the average of the phase-averaged signal. Results have shown that for a wide range of T^*, this method can result in a more accurate estimation of the mean quantity. Figure B.1a highlights this finding for two different values of the starting phase, ϕ. The dashed lines indicate the mean computed by averaging the phase-averaged data. This estimate of the true mean consistently provides an estimate very close to the exact value of zero for T^* values larger than *100*. In contrast, the mean computed by the classic procedure of summing all of the values and dividing by the number of samples yields a result significantly poorer estimate of the actual mean. As T^* increases, the mean computed in this manner generally improves in accuracy as expected from the increased number of samples in the record. However, the error does not decay uniformly and oscillations are noted in the estimated value of the mean. Zero error occurs when the total number of samples occupy an exact number of cycles.

Since varying ϕ can result in differences in the estimated value of the average obtained using either method, it was deemed necessary to find a quantity which assesses the sensitivity to this effect. The mean value was computed for *16* different values of the starting phase and the RMS of these *16* samples gives an indication of the variation expected in the estimation of the mean caused by changes in ϕ. Figure B.1b shows similar trends as the previous figure. For the majority of the range examined, computing the average of the phase-averaged data yields more accurate results than computing the average via standard methods. It is noted that for a record length of exactly *500* periods yields zero error for the standard method. This location of $T^* = 500$ is an artifact of the particular signal and sampling frequencies chosen. Different combinations of these two parameters will yield a different T* value where zero error is found..

The computation of the mean using the direct method yields less accurate results than averaging the phase averaged data because the record length may contain a non-integral number of cycles. The effect is similar to sampling the signal with a sufficient sampling frequency, however, not sampling the entire waveform. When sampling a waveform with only a few measurements per cycle, the signal will not be sampled uniformly over its period. Thus, certain phases of the signal will be disproportionately represented in the mean. This effect gets reduced as the record length increases. Phase-averaging the signal first eliminates this bias. The zero value at $T^* = 500$ is a good example of this effect. At this non-dimensional sampling time, the sampling frequency and function frequency are such that all phases of the signal are equally represented. Thus, the standard procedure for the computation of the mean generates a very good estimate of the average for all starting phases. The exact number of samples necessary for this nodal point to occur will vary with the exact selection of sampling and signal frequency.

When the frequency of a sparsely sampled signal is known, that information can be used to improve the estimate of the calculation of the mean. The additional information provided by the signal frequency allows for this increase in accuracy. It should be noted however that in absolute terms, the difference in accuracy between the two methods is small. The error resulting from the direct computation of the mean at $T^*=100$ is only 0.2% of the signal amplitude.

Appendix C

Velocity Forcing Amplitude Calibration Curves for the Two-stream Mixing Layer Facility

In the experiments conducted in this dissertation, the velocity perturbations were input into the through an oscillating bellows mechanism. This bellows is driven by an electromagnetic shaker which derives its command forcing signal from a function generator. Typically, the perturbation is input by setting the peak to forcing frequency and peak-to-peak amplitude of the command signal. The bellows is driven in open-loop mode, so the amplitude of the bellows motion is dependent upon the frequency. The amplitude or the bellows motion is measured by means of linear position transducer. The velocity perturbation in this, as well as previous experiments, is reported as the RMS streamwise velocity fluctuations, u_{rms} normalized by the free-stream velocity, u_0. As the fluctuation levels decrease with downstream location, this measurement is made as far upstream as possible.

Figure C.1 shows the calibration of the free-stream velocity disturbance in the mixing layer facility with the displacement of the bellows/shaker mechanism and with the input peak-to-peak levels of the command signal. All of the data was collected at x = 3.75 cm and for a wake case with u_0 = 9.4 cm/s. The vast majority of the data is for the 6 Hz forcing frequency, however, a smaller amount of data for the 4 Hz and 8 Hz forcing frequencies are also shown. As described in the main portion of the thesis, the u velocity perturbations do

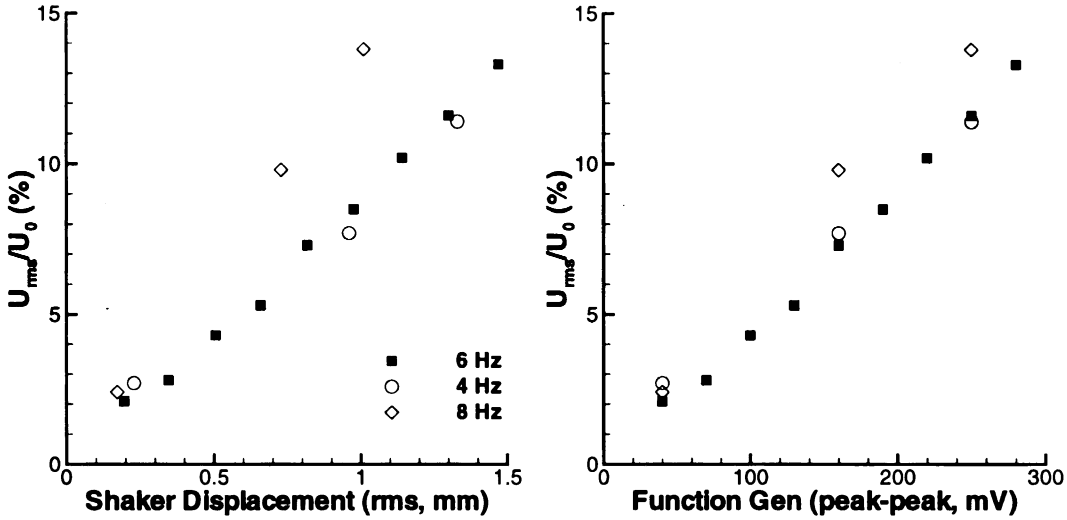

Figure C.1: Velocity perturbation calibration curves for the forced wake.

not reach a steady level for the 4 Hz forcing cases. Thus, the perturbation level is dependent both upon the spanwise and streamwise position of the measurement. For all three forcing frequencies, the relationship between the input forcing and the velocity disturbance is linear. However, the slope is not constant between the different forcing frequencies. This indicates, as expected, that the flow responds differently to the different input forcing frequencies.

BIBLIOGRAPHY

BIBLIOGRAPHY

Abrahamson, S. and Lonnes, S. [1995] "Uncertainty in Calculating Vorticity from 2D Velocity Fields using Circulation and Least Square Approaches." *Experiments in Fluids*, **20**, pp. 10-20.

Agui, J. and Jimenez, J. [1987] "On the Performance of Particle Tracking." *Journal of Fluid Mechanics*, **186**, pp. 447-468.

Breidenthal, R. [1980] "Response of Plane Shear Layers and Wakes to Strong Three-Dimensional Disturbances." *Physics of Fluids*, **23**(10), pp. 1929-1933.

Cohn, R.K., Gendrich, C.P., MacKinnon, C.G., and Koochesfahani, M.M. [1995] "Crossflow Velocimetry Measurements in a Wake Flow." *Bulletin of the American Physical Society*, **40**(12), p. 1962.

Cohn, R.K. and Koochesfahani, M.M. [1993] "Effect of Boundary Conditions on Axial Flow in a Concentrated Vortex Core." *Physics of Fluids A*, **5**(1), pp. 280-282.

Cohn, R.K. and Koochesfahani, M.M. [1997] "Structure of the Velocity and Vorticity Field in a Confined Wake." *Bulletin of the American Physical Society*, **42**(11), p. 2197.

Fouras, A. and Soria, J. [1998] "Accuracy of Out-of-Plane Vorticity Measurements from In-Plane Velocity Field data." *Experiments in Fluids,* **25**(5/6), pp. 409-430.

Gendrich, C.P, Bohl, D.G., and Koochesfahani, M.M. [1997] "Whole-Filed Measurements of Unsteady Separation in a Vortex Ring/Wall Interaction. AIAA Paper #97-1780.

Gendrich, C.P. and Koochesfahani, M.M. [1996] "A Spatial Correlation Technique for Estimating Velocity Fields Using Molecular Tagging Velocimetry." *Experiments in Fluids*, **22**, pp. 67-77.

Gendrich, C.P., Koochesfahani, M.M., and Nocera, D.G. [1997] "Molecular Tagging Velocimetry and Other Novel Applications of a New Phosphorescent Supramolecule." *Experiments in Fluids*, **23**, pp. 361-372.

Hartmann, W.K., Gray, M.H.B., Ponce, A., Docera, D.G., and Wong, P.A. [1996] "Substrate Induced Phosphorescence from Cyclodextrin-Lumophore Host-Guest Complexes." *Inorganica Chimica Acta*, **243**, pp. 239-248.

Hagen, J.P. and Kurosaka, M. [1993] "Corewise Cross-Flow Transport in Hairpin Vortices--the 'Tornado Effect'." *Physics of Fluids A*, **5**(12), pp. 3167-3174.

Hilbert, H.S. and Falco, P.E. [1991] “Measurements of Flows during Scavenging in a Two-Stroke Engine.” SAE 910671.

Hill, R.B. and Klewicki, J.C. [1991] “Data Reduction Methods for Flow Tagging Velocity Measurements.” *Experiments in Fluids*, **20**(3), pp. 142-152.

M. M. Koochesfahani, R. K. Cohn, C. P. Gendrich, and D. G. Nocera [1996] “Molecular Tagging Diagnostics for the Study of Kinematics and Mixing in Liquid-Phase Flows.” Plenary presentation at the Eighth International Symposium on Applications of Laser Techniques to Fluid Mechanics, Lisbon, Portugal, July 8-11, 1996: pp. 1.2.1 - 1.2.12.

Koochesfahani, M.M. [1989] “Vortical Patterns in the Wake of an Oscillating Airfoil.” *AIAA Journal*, **27**, pp. 1200-1208.

Koochesfahani, M.M. and Nelson, K.E. [1997] “Molecular Mixing Enhancement in the Confined Wake of a Splitter Plate.” AIAA paper #97-2007.

Kurosaka, M., Christiansen, W.H., Goodman, J.R., Tirres, L., and Wohlman, R.A. [1988] “Crossflow Transport Induced by Vortices.” *AIAA Journal*, **26**(11), pp. 1403-1405.

Lasheras, J.C. and Meiburg, E. [1990] "Three-Dimensional Vorticity Modes in the Wake of a Flat Plate." *Physics of Fluids A*, **2**(3), pp. 371-380.

LeBoeuf, R.L. and Mehta, R.D. [1996] "Topology of the Near-Field Vortical Structures in a Three-Dimensional Wake." *Experimental Thermal and Fluid Science*, **13**, pp. 223-238.

Luff, J.D., Drouillard, T., Rompage, A.M., Linne, M.A., and Hertberg, J.R. [1999] “Experimental Uncertainties Associated with Particle Image Velocimetry (PIV) Based Vorticity Algorithms.” *Experiments in Fluids*, **26**, pp. 36-54.

MacKinnon, C.G. and Koochesfahani, M.M. [1997] “Flow Structure and Mixing in a Low Reynolds Number Forced Wake inside a Confined Channel.” *Physics of Fluids*, **9**(10), pp. 3099-3101.

Mattingly, G.E. and Criminale, W.O. [1972] “The Stability of an Incompressible Two-Dimensional Wake.” *Journal of Fluid Mechanics*, **51**(2) pp. 233-272.

Nelson, K.E. [1996] *Structure and Mixing in a Low Reynolds Number Forced Wake in a Confining Channel.* M.S. Thesis, Michigan State University.

Meiburg, E. and Lasheras, J.C. [1988] "Experimental and Numerical Investigation of the Three-Dimensional Transition in Plane Wakes." *Journal of Fluid Mechanics*, **190**, pp. 1-37.

Ponce, A., Wong, P.A., Way, J.J., and Nocera, D.G. [1993] "Intense Phosphorescence Triggered by Alcohols upon Formation of a Cyclodextrin Ternary Complex." *Journal of Physical Chemistry*, **97**, pp. 1137-1142.

Visbal, M.R., Gaitonde, D.V., and Gogineni, S.P. [1998] "Direct Numerical Simulation of a Forced Transitional Plane Wall Jet." AIAA paper #98-2643.

Roberts, F.A. [1985] *Effects of a Periodic Disturbance on Mixing in Turbulent Shear Layers and Wakes*. Ph.D. thesis, Caltech.

Sato, H. [1970] "An Experimental Study of the Non-Linear Interaction of Velocity Fluctuations in the Transition Region of a Two-Dimensional Wake." *Journal of Fluid Mechanics*, **44**(4), pp. 741-765.

Sato, H. and Kuriki, K. [1961] "The Mechanism of Transition in the Wake of a Thin Flat Plate Placed Parallel to a Uniform Flow." *Journal of Fluid Mechanics*, **11**, pp. 321-352.

Spedding, G.R. and Rignot, E.J.M. [1993] "Performance Analysis and Application of Grid Interpolation Techniques for Fluid Flows." *Experiments in Fluids*, **15**, pp. 417-430.

Stier, B. [1994] *An Investigation of Fluid Flow during Induction Stroke of a Water Analog Model of an IC Engine Using an Innovative Optical Velocimetry Concept -LIPA*. PhD. Thesis, Michigan State University.

Weygandt, J.H. and Mehta, R.D. [1995] "Three-Dimensional Structure of Straight and Curved Plane Wakes." *Journal of Fluid Mechanics*, **282**, pp. 279-311.

Wygnanski, I., Champagne, F., and Marasli, B. [1986] "On the Large-Scale Structures in Two-Dimensional, Small-Deficit, Turbulent Wakes." *Journal of Fluid Mechanics*, **168**, pp. 31-71.